Search for neutrino-induced particle showers with IceCube-40

D i s s e r t a t i o n

zur Erlangung des akademischen Grades

d o c t o r r e r u m n a t u r a l i u m

(Dr. rer. nat.)

im Fach Physik

eingereicht an der
Mathematisch-Naturwissenschaftlichen Fakultät
der Humboldt-Universität zu Berlin

von
Dipl. Phys. Eike Middell

Präsident der Humboldt-Universität zu Berlin:
Prof. Dr. Jan-Hendrik Olbertz

Dekan der Mathematisch-Naturwissenschaftlichen Fakultät:
Prof. Dr. Elmar Kulke

Gutachter/innen:
1. Prof. Dr. Marek Kowalski
2. Dr. Elisa Bernardini
3. Dr. Alexander Kappes

Tag der mündlichen Prüfung: 23.02.2015

To Nadin

Abstract

Located at the geographic South Pole, the IceCube Neutrino Observatory is presently the world's largest detector to search for neutrinos in the TeV to PeV range. A cubic-kilometer volume deep in the glacial ice has been instrumented with digital optical sensors in order to record Cherenkov light emitted by charged secondary particles that are generated in neutrino interactions. The experiment aims at the detection of an astrophysical high-energy neutrino flux from which answers are expected regarding the long standing question of the origin of cosmic rays. The construction of IceCube was completed in 2010. In data taken in the following two years evidence for an astrophysical diffuse neutrino flux was found.

This dissertation presents a search for neutrino-induced particle showers, also called cascades, in data taken between April 2008 and May 2009 during IceCube's construction phase, when about 50% of the final configuration was deployed and operational. The goal of this analysis is the detection of the astrophysical diffuse neutrino flux while maintaining sensitivity to neutrinos originating from the Earth's atmosphere. Both neutrino fluxes must be separated from a much more abundant background of muons created in cosmic-ray-induced air showers. Good energy reconstruction and a signature in the detector that is qualitatively different from the muon background make cascade searches very well-suited for this task.

A robust estimate of this background has been obtained from air-shower simulations and techniques were developed to isolate the neutrino flux from the atmospheric muon background. Two event selections were prepared. Firstly, a low-energy sample with an energy threshold of about 2 TeV aimed at the detection of atmospheric neutrinos. A 1.1σ excess over the expectation from atmospheric muons was found. The excess can be explained well by atmospheric neutrinos but is not significant enough to rule out a muon-background-only hypothesis. Secondly, a high-energy sample with an energy threshold of about 100 TeV targeted the astrophysical neutrino flux. In this sample a 2.7σ excess over the expectation from atmospheric muons and neutrinos was found. While not significant enough to claim a detection, the flux normalization of astrophysical neutrinos following an E^{-2} energy spectrum is constrained. For equal flavor contributions a 90% credible interval covers the range $(2 - 14) \times 10^{-8}\,\mathrm{GeV sr^{-1} s^{-1} cm^{-2}}$ and is compatible with the more stringent flux estimates obtained by measurements with the completed IceCube detector.

Zusammenfassung

Das am geographischen Südpol gelegene IceCube Neutrino Observatorium ist der derzeit größte Detektor für die Suche nach extraterrestrischen Neutrinos mit TeV-PeV Energien. Ein kubikkilometergroßes Volumen tief im Antarktischen Eisschild wurde mit optischen Sensoren instrumentiert, um die in Neutrinowechselwirkungen entstandene Cherenkov-Strahlung nachzuweisen. Das Experiment zielt auf die Entdeckung astrophysikalischer, hochenergetischer Neutrinos ab, von denen man sich Antworten auf die seit mehr als 100 Jahren offene Frage nach dem Ursprung der kosmischen Strahlung erhofft. Der IceCube-Detektor wurde 2010 fertiggestellt. Mit Daten, die in den folgenden zwei Jahren aufgezeichnet wurden, konnte der Nachweis eines diffusen, astrophysikalischen Neutrinoflusses erbracht werden.

Die vorliegende Dissertation beschreibt eine Suche nach neutrinoinduzierten Teilchenschauern in Daten, die von April 2008 bis Mai 2009 während der Konstruktionsphase von IceCube aufgezeichnet wurden. In der Zeit war etwa die Hälfte der endgültigen Detektoranordnung installiert und betriebsbereit. Das Ziel der Arbeit war die Entdeckung astrophysikalischer Neutrinos mit der Maßgabe, gleichzeitig eine Sensitivität für Neutrinos terrestrischen Ursprungs aufrecht zu erhalten. Beide Sorten von Neutrinos müssen von einem um ein Vielfaches größeren Untergrund von atmosphärischen Myonen isoliert werden. Die Suche nach Teilchenschauern im Detektor bietet sich hierfür an, da für diese Ereignisklasse eine gute Energierekonstruktion möglich ist. Außerdem unterscheidet sich eine solche Signatur der Neutrinowechselwirkung qualitativ von der Signatur des Myonuntergrunds.

Eine robuste Abschätzung des Myonuntergrunds konnte mittels Luftschauersimulationen gewonnen werden und Methoden wurden entwickelt um Neutrinos und Myonen voneinander zu unterscheiden. Darauf aufbauend wurden zwei verschiedene Selektionen von Ereignissen erstellt. Ein Niedrigenergiedatensatz mit einer Energieschwelle von 2 TeV zielte auf die Messung atmosphärischer Neutrinos ab. In diesem Datensatz wurden mehr Ereignisse gefunden als man von atmosphärischen Myonen allein erwartet hätte. Der Überschuss entspricht 1.1σ und kann quantitativ gut mit atmosphärischen Neutrinos erklärt werden. Er ist jedoch nicht signifikant genug um einen rein myonischen Ursprung auszuschließen. Der zweite Hochenergiedatensatz zielte auf die Entdeckung astrophysikalischer Neutrinos ab, mit einer Energieschwelle von 100 TeV. Ein 2.7σ Überschuss in Bezug auf atmosphärische Myonen und Neutrinos wurde gefunden. Zwar ist auch dieser Überschuss nicht signifikant genug um einen rein terrestrischen Ursprung auszuschließen, aber er schränkt den möglichen astrophysikalischen Neutrinofluss ein. Für ein E^{-2} Energiespektrum und gleiche Anteile an Elektron-, Myon- und Tauonneutrinos erstreckt sich ein Bayesianisches 90%-Konfidenzintervall über den Bereich $(2 - 14) \times 10^{-8}\,\mathrm{GeVsr^{-1}s^{-1}cm^{-2}}$. Das Resultat ist kompatibel zu der stringenteren Flussmessung, die mit dem fertiggestellten IceCube Detektor gelang.

Contents

1 Introduction

High-energy neutrino astronomy gradually becomes a reality. The evidence for astrophysical neutrinos recently found by the IceCube detector [1] is a promising achievement which offers new prospects to the field of astrophysics. The possibility to detect astrophysical neutrinos above 1 TeV opens a new window to the understanding of the non-thermal universe. The topic of this dissertation is the implementation and refinement of one particular approach to neutrino detection.

Certain populations of particle in the universe reach energies which are typically only found in macroscopic objects. Namely, cosmic rays constantly hit the Earth's upper atmosphere with energies reaching up to 10^{20} eV or 16 J. These high energies of single subatomic particles cannot be explained with thermal processes. Instead the particles are thought to attain their energy through acceleration processes in energetic astrophysical objects. Even now, more than 100 years after the discovery of cosmic rays by Victor Hess [2], the sources of the highest energetic cosmic rays are still unknown. Consequently, also the specifics of how they attain such high energies remain unclear.

Neutrino-astronomy could help to answer these questions. In the prevailing picture particles are accelerated in energetic astrophysical objects, like supernovae or gamma-ray bursts. When they escape the objects as cosmic rays, they are likely to interact with surrounding matter and radiation fields. In these interactions neutrinos would be produced. Hence, cosmic-ray sources would also be sources of high-energy neutrinos. This connection makes neutrinos versatile probes which tell us much about cosmic-ray sources.

By detecting high-energy neutrinos from an astrophysical object it can be identified as a cosmic-ray source. Furthermore, the physics of acceleration mechanisms can be probed. Astrophysical neutrinos are also expected to contribute answers to fundamental questions concerning neutrino oscillations, the nature of dark matter and quantum gravity [3]. Last but not least there is always the hope that a new observation channel to the universe leads to new and unexpected discoveries.

Experimentally, the main problem is that neutrinos are hard to detect due to their low interaction cross sections. Huge volumes need to be made sensitive to neutrino interactions in order to detect the astrophysical neutrino flux. They can be observed via the Cherenkov light

emitted by charged secondary particles created in the interaction. The instrumentation of large natural bodies of water or ice with light sensors has proved to be a viable approach to create sensitive detectors. Such water Cherenkov detectors were built and operated in the Siberian Lake Baikal [4], the Mediterranean Sea [5] and the Antarctic ice sheet. Over decades the available neutrino detectors grew in size and increased their sensitivity [6]. This effort culminated in the construction of the IceCube Neutrino Observatory, a cubic kilometer array of light sensors buried deep in the glacial ice at the geographic South Pole [7].

Neutrino interactions in water Cherenkov detectors can be attributed to two main classes: track-like events containing a muon track and cascade-like events containing one or more particle showers. Since the former provides good angular resolution of the incident neutrino, it is the preferred channel for the search for neutrino point sources. Compared to the muon channel the advantages of the cascade channel are a better resolution of the neutrino energy and a sensitivity to not only one, but all neutrino flavors. In some aspects cascades allow for an easier separation from the muon and neutrino background created in the Earth's atmosphere [8].

Even if the sensitivity of a neutrino detector is too low to identify neutrino point sources, the detector may still be sensitive to the combined diffuse astrophysical neutrino flux. This flux is formed by the collective contributions of all unresolved neutrino sources and is expected to have an energy spectrum following a power law with index -2. Searches for the diffuse neutrino flux have to separate astrophysical neutrinos from a muon and neutrino background of terrestrial origin. Because the spectrum of astrophysical neutrinos is harder than the spectra of the atmospheric background, a search for the diffuse neutrino flux through a calorimetric measurement of the neutrino spectrum is possible [9]. Cascade searches are particularly suited for this kind of measurement.

The recently found evidence for this diffuse astrophysical neutrino flux has an all-flavor intensity estimated to be $\mathrm{E}_\nu^2\Phi = (3.6 \pm 1.2) \times 10^{-8}\,\mathrm{GeV sr^{-1} s^{-1} cm^{-2}}$ with indications for a cutoff at $\sim 2\,\mathrm{PeV}$. It is consistent with an isotropic flux and a flavor ratio of $\nu_e : \nu_\mu : \nu_\tau = 1 : 1 : 1$ [1]. A large fraction of the events contributing to this result were cascades, including two particle showers with PeV energies [10].

This thesis presents a search for neutrino-induced cascades in one year of data, taken during the construction phase of IceCube, when about half of the detector was operational (IceCube-40). The objective of this search was to identify an astrophysical flux of high-energy neutrinos, while maintaining a sensitivity to atmospheric neutrinos in the few TeV energy range. This analysis succeeds searches done on the previous IceCube-22 detector configuration [11] and searches done with IceCube's predecessor AMANDA [12, 13]. It was conducted parallel to two other cascade searches on the IceCube-40 dataset, hence it shares some of their methodology [14, 15]. It complements a search for the diffuse neutrino flux done with muon neutrinos on the IceCube-59

dataset [16]. While small excesses were found in [15] and [16], they were not significant enough to claim a detection. Hence, all these searches produced upper limits on the diffuse neutrino flux.

Methods used in previous analyses were recombined and further developed to create an event selection suitable for the objectives of this analysis. A particular challenge of the previous cascade analyses was to obtain a robust background estimate for atmospheric muons in the few TeV energy range. This background is estimated from Monte Carlo simulations and obtaining sufficiently sized Monte Carlo datasets has been a computationally intractable problem. Therefore, developing an approach to achieve a reliable background estimate was crucial for this analysis.

The thesis is structured as follows: firstly, as a basis the theoretical background for this analysis is outlined with a special focus on cosmic rays and the search for their sources. The connection between cosmic rays and high-energy neutrinos is explained. Afterwards, the experimental aspects of neutrino detection are described by discussing detector physics in general and IceCube with its different detection channels in particular. Hereafter, Monte Carlo techniques employed in this analysis are shown and the method used to obtain a sufficiently sized Monte Carlo dataset of atmospheric muons is presented. Subsequently, the analysis is described in detail and sources of systematic uncertainties are discussed. Finally, the results of this analysis are presented, followed by a summary and outlook.

2 Atmospheric and Astrophysical Neutrinos

As a basis for the following analysis this chapter will provide the astrophysical and particle physics theory background. The energy spectrum of cosmic rays is discussed as well as the acceleration mechanisms through which they are thought to attain their energy. After explaining the connection between cosmic rays and high-energy neutrinos, source candidates for both will be discussed. By shifting the focus from the sources to Earth, the oscillation effects during neutrino propagation as well as neutrino production in the atmosphere will be covered.

2.1 Cosmic Rays

The Earth's upper atmosphere is constantly bombarded with highly-energetic charged particles which were discovered in balloon flights by Victor Hess in 1912 [2]. Since then, cosmic rays have been the subject of large experimental effort. By reaching energies, which largely exceed the capabilities of current particle accelerators at Earth, cosmic rays prompt the question, where these particles originate from and how they acquire their energy. As charged particles are deflected in the magnetic fields of the interstellar medium the arrival direction of cosmic rays provides only little information to answer these questions. However, from studies of the energy spectrum and elemental composition of cosmic rays much has already been learned.

The available measurements of the cosmic-ray energy spectrum cover many orders of magnitude both in energy and intensity. A compilation of measurements is shown in Figure 2.1. Individual particles with energies exceeding $10^{20}\,\mathrm{eV}$ have been detected although these particles are extremely rare. The spectrum follows a broken power law with the intensity of the cosmic-ray flux dropping from one particle per square meter and second at $10^{11}\,\mathrm{eV}$ down to one particle per square kilometer and century at $10^{20}\,\mathrm{eV}$.

At lower energies direct measurements of the cosmic-ray flux are possible. Balloon- and satellite-borne particle detectors allow for energy measurements and particle identification [25]. The intrinsic size limitations of airborne experiments ($\mathcal{O}(\mathrm{m}^2)$) restrict these experiments to energies below 100 TeV. Up to this energy about 79% of the cosmic rays are protons. Of the rest again 70% are nucleons bound in helium nuclei and the remainder are nuclei of heavier elements [25]. Electrons provide only a minor contribution to the total cosmic-ray particle

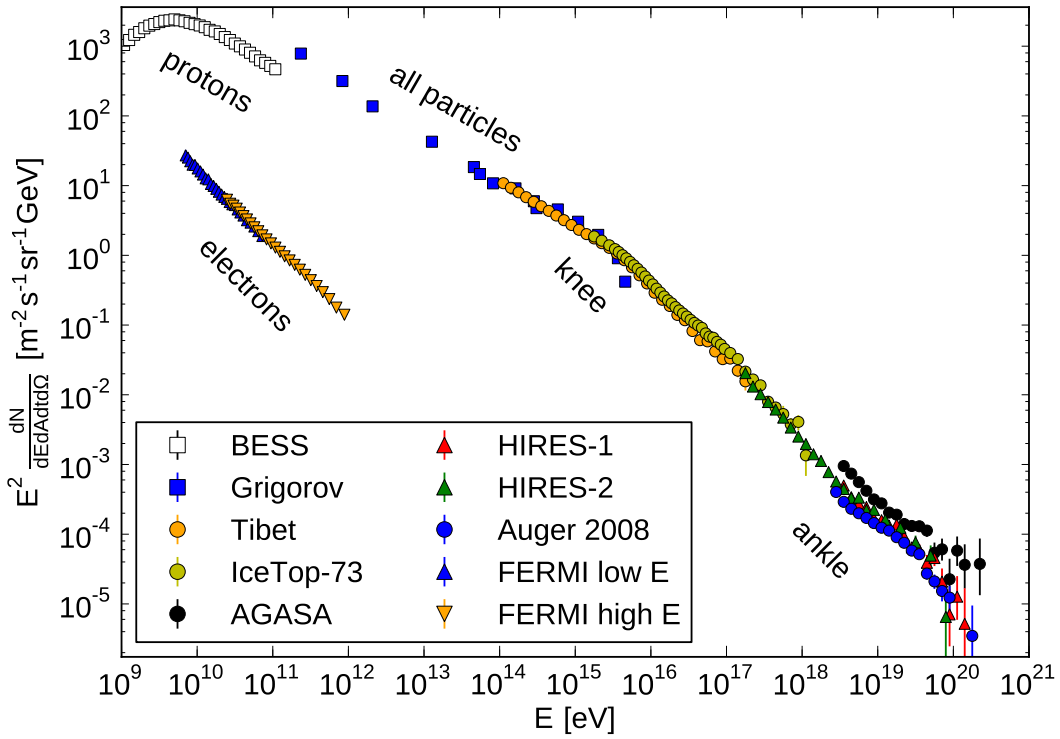

Figure 2.1: Cosmic Ray Spectrum. The plotted data was obtained from references [17–24].

flux [24]. The spectrum follows approximately a power law:

$$\frac{dN}{dE} \approx 1.8 \times 10^4 (E/\,\mathrm{GeV})^{\alpha}\ \frac{\text{nucleons}}{\mathrm{m^2\,s\,sr\,GeV}}, \tag{2.1}$$

where E denotes the energy per nucleon and the slope of the spectrum is given by the index $\alpha = -2.7$ [25].

Above 100 TeV one has to revert to indirect measurements of cosmic rays. When high-energy cosmic rays hit the atmosphere they induce air showers in which secondary particles are created. Extended ground arrays with sizes up to $\mathcal{O}(10^3 \mathrm{km}^2)$ have been built to study the nature of these air showers. The applied techniques encompass the detection of the secondary particles when they reach the ground as well as the detection of fluorescent light and Cherenkov light that is also created in the shower. For any detected air shower the information on the primary nucleus has to be inferred from properties of the air shower. Fluctuations in the shower development and uncertainties in the physics of hadronic interactions within the air shower make the determination of the cosmic ray composition difficult [26]. Consequently, Figure 2.1 shows

the all-particle spectrum above 100 TeV.

The power law in Eq. 2.1 continues to higher energies but exhibits two distinct changes in slope. Around 3×10^{15} eV, the so-called knee, the spectrum steepens from $\alpha = -2.7$ to $\alpha = -3.1$. The spectrum hardens again at the ankle around $10^{17} - 10^{18}$ eV. In addition, there are indications for a cutoff in the spectrum at about 10^{20} eV [22]. An upper limit on the cosmic ray energy has been predicted by Greisen, Zatsepin and Kuzmin since at these high energies cosmic rays are able to interact with the cosmic microwave background photons via the Δ^+-resonance and transform to lower-energetic pions [27].

Regarding the composition of cosmic rays there is evidence that around the knee the chemical composition changes with heavier elements becoming more dominant [28]. The composition at the ankle is not clear yet since experimental data disagrees whether at the highest energies the composition is lighter or heavier [26].

These transitions in slope and composition provide hints for the origins of cosmic rays. Cosmic rays above the ankle are most likely extra-galactic. This argument is based on the gyro-radius r_g, which for a particle with momentum p and charge ze in a magnetic field B calculates to:

$$r_g = \frac{p}{zeB} = \frac{R}{B} = 1.08 \frac{(p/\,\mathrm{PeVc^{-1}})}{z(B/\,\mu\mathrm{G})}\,\mathrm{pc}. \tag{2.2}$$

The quantity $R = p/ze$ is called the rigidity and denotes the particles resistance to deflection in the magnetic field. Protons with energies above 10^{18} eV traversing the galactic magnetic field of a few μG would have gyro-radii of above 300 pc. As this exceeds the thickness of the galactic disc they would rather escape the galaxy than reaching Earth. In contrast, below the ankle cosmic-rays would be magnetically confined so the majority of cosmic rays is thought to originate from within our galaxy.

A feature like the knee, i.e. a steepening in the spectrum, is expected around the highest energy attainable by cosmic rays from a major source class. Namely, young supernova remnants are thought to run out of steam at PeV energies [29]. Also the observed change in composition towards heavier elements is expected in this scenario. For a cosmic ray particle of charge Ze the maximum attainable energy $E_{\max}$ scales with charge: $E_{\max}(Z) = ZE_{\max}(Z = 1)$ (see Section 2.2.1). With increasing energy the steepening of the spectrum will occur first for protons, resulting in a higher fraction of heavier elements at the energies above [30].

2.1.1 Fermi Acceleration of Charged Particles

Diffuse shock acceleration, also called Fermi acceleration [31], is the prevalently assumed mechanism how particles are accelerated to the observed energies. In this process particles gain

energy by being repeatedly scattered off moving clouds of plasma or shock fronts as they are for example formed by the blast waves of supernovae. Other astrophysical objects in which Fermi acceleration is believed to take place are discussed in Section 2.1.2.

One of the advantages of Fermi acceleration is that under fairly general assumptions the process leads to an energy spectrum at the source following a power law with index ≈ -2. Together with assumptions about the energy-dependent diffusion process how cosmic rays meander from the source to Earth, an E^{-2} source spectrum can explain the $E^{-2.7}$ cosmic-ray spectrum observed at Earth [32]. Consequently, in theoretical models E^{-2} energy spectra are a common assumption. The analysis presented in Chapter 5 searches for neutrinos of astrophysical origin which are produced alongside with cosmic rays and are therefore thought to follow a power law with an index close to -2 as well. Identifying these neutrinos crucially depends on the condition that the astrophysical neutrino spectrum is with E^{-2} harder than the spectrum of neutrinos of terrestrial origin.

Because of this fundamental fact it seems appropriate here to give a derivation of the acceleration mechanism and the resulting energy spectrum. Below, the line of arguments in Refs. [33] and [34] is followed.

Let's consider an acceleration process, which a particle of initial energy E_0 can repeat several times, each time gaining an amount of energy ΔE proportional to its current energy: $\Delta E = \xi E$. At each iteration it has a probability P_{esc} to escape the process. This results in an energy spectrum that follows a power law. After n iteration the particle would have reached the energy:

$$E_n = E_0(1+\xi)^n. \tag{2.3}$$

The number iterations n required to reach energy E is given by:

$$n = \frac{\log\left(E/E_0\right)}{\log\left(1+\xi\right)}, \tag{2.4}$$

and the probability to not having escaped the acceleration process is:

$$P_n = (1-P_{\text{esc}})^n. \tag{2.5}$$

Hence, the number of particles finishing n or more iterations and therefore exceeding energy E calculates to:

$$N(\geq E) \propto \sum_{m=n}^{\infty}(1-P_{\text{esc}})^m = \frac{(1-P_{\text{esc}})^n}{P_{\text{esc}}}. \tag{2.6}$$

By eliminating n from Eq. 2.6 through substitution of Eq. 2.4 one obtains:

$$N(\geq E) \propto \frac{1}{P_{\text{esc}}} \left(\frac{E}{E_0}\right)^{-\gamma} \quad \text{with} \quad \gamma = \frac{\log\left(\frac{1}{1-P_{\text{esc}}}\right)}{\log\left(1+\xi\right)} \approx \frac{P_{\text{esc}}}{\xi}. \tag{2.7}$$

So the differential energy spectrum follows a power law with index $-\gamma - 1$:

$$\frac{dN}{dE} \propto \left(\frac{E}{E_0}\right)^{-\gamma-1}. \tag{2.8}$$

In the case of Fermi acceleration charged particles are accelerated at the intersection of two regions of ionized gas, i.e. either gas clouds or shock fronts. These regions move with different velocities. For example supernova explosions can eject material with velocities of about $10^4\,\text{kms}^{-1}$ into the surrounding interstellar medium. With about $10\,\text{kms}^{-1}$ the speed of sound is much smaller there [34]. A shock front forms which then propagates with supersonic velocities through the ambient medium.

The gas is ionized and carries turbulent magnetic fields from which charged particles are elastically scattered. These deflections at magnetic fields cannot directly transfer energy to the particles. But they cause a randomization of the particle directions. After entering the gas cloud or crossing the plane shock front, the particles are scattered several times after which their directions are isotropic in the rest frame of the moving gas. However, when observed from the rest frame of the outer region, to which the particle eventually returns, the particle on average prefers the direction of the moving gas.

Let's now consider a relativistic particle of energy E_1 much larger than its rest mass and moving at a velocity close to the speed of light. It enters a region of gas moving at velocity $\vec{V}$ at a relative angle θ_1. This can either be a plasma cloud with velocity $\vec{V}$ or it can be the gas behind a shock front. In the rest frame of the shock the gas upstream flows into the shock with velocity $\vec{u}_1$ and downstream it departs with velocity $\vec{u}_2$. Hence, in a laboratory frame the shock front moves with velocity $-\vec{u}_1$ and the gas behind the front moves with velocity $\vec{V} = -\vec{u}_1 + \vec{u}_2$. Figure 2.2 illustrates the geometric setup.

By applying a Lorentz transformation the particle's energy in the rest frame of the gas (denoted by primed symbols in the following formulas) is as follows:

$$E_1' = \gamma E_1 \left(1 - \beta \cos\theta_1\right), \tag{2.9}$$

where $\beta = V/c$, $V = \left|\vec{V}\right|$ and $\gamma = (1-\beta^2)^{-1/2}$. Inside the gas the energy of the particle E_1' is not changed. After being elastically scattered several times the particle leaves with angle θ_2'. In

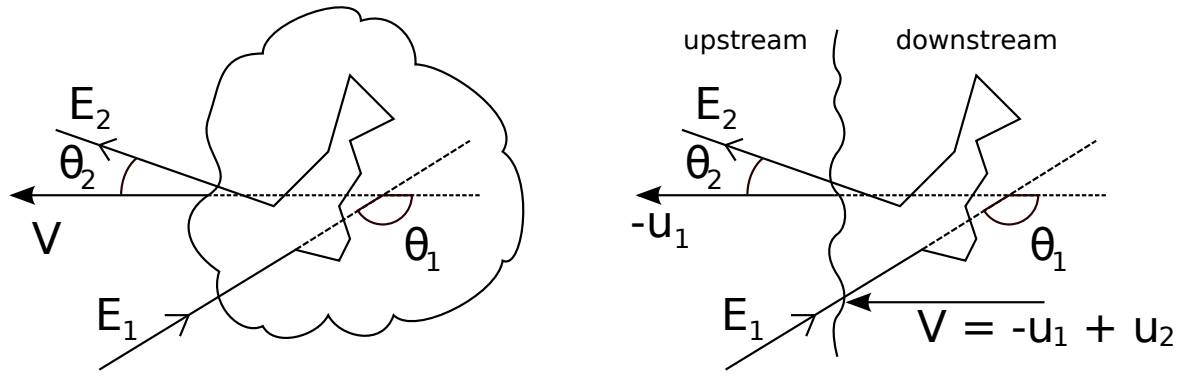

Figure 2.2: Scattering of a particle on a moving cloud of plasma (left) and at a plane shock front (right).

the original frame of reference the energy of the particle is then:

$$E_2 = \gamma E_1' \left(1 - \beta \cos\theta_2'\right). \tag{2.10}$$

By substituting Eq. 2.9 in Eq. 2.10 the energy gain (or loss) calculates to:

$$\frac{\Delta E_1}{E_1} = \xi = \frac{1 - \beta\cos\theta_1 + \beta\cos\theta_2' - \beta^2\cos\theta_1\cos\theta_2'}{1-\beta^2} - 1, \tag{2.11}$$

which only depends on the entrance and exit angles and the velocity of the moving gas.

The crucial difference between scattering on (a) gas clouds or (b) plane shock fronts is the distribution of the entrance and exit angles. For the gas cloud the distribution of $\cos\theta_1$ is proportional to the relative velocity between cloud and particle. Inside the cloud the particle direction is isotropized, making all exit directions equally probable:

$$\frac{dp}{d\cos\theta_1} = \frac{c - V\cos\theta_1}{2c}, \qquad -1 \le \cos\theta_1 \le 1, \qquad \langle\cos\theta_1\rangle_a = -\frac{V}{3} \tag{2.12}$$

$$\frac{dp}{d\cos\theta_2'} = const., \qquad -1 \le \cos\theta_2' \le 1, \qquad \langle\cos\theta_2'\rangle_a = 0. \tag{2.13}$$

In the case of the plane shock fronts the distributions of θ_1 and θ_2' are obtained by selecting those particles from an isotropic flux which cross the plane from upstream to downstream and

vice versa. To select these particles, the flux is projected onto the plane:

$$\frac{dp}{d\cos\theta_1} = 2\cos\theta_1, \qquad -1 \leq \cos\theta_1 \leq 0, \qquad \langle\cos\theta_1\rangle_b = -\frac{2}{3} \tag{2.14}$$

$$\frac{dp}{d\cos\theta_2'} = 2\cos\theta_2', \qquad 0 \leq \cos\theta_2' \leq 1, \qquad \langle\cos\theta_2'\rangle_b = +\frac{2}{3}. \tag{2.15}$$

By substituting the average entrance and exit angles from Eq. 2.12 to Eq. 2.15 into Eq. 2.11 the average energy change from a single interaction with a gas cloud or a single shock front traversal is obtained:

$$\langle\xi\rangle_a = \frac{1+\frac{1}{3}\beta^2}{1-\beta^2} - 1 \approx \frac{4}{3}\beta^2 \tag{2.16}$$

$$\langle\xi\rangle_b = \frac{1+\frac{4}{3}\beta+\frac{4}{9}\beta^2}{1-\beta^2} - 1 \approx \frac{4}{3}\beta. \tag{2.17}$$

The last approximation assumes gas clouds and shocks to move at non-relativistic speeds ($\beta \ll 1$). In the case of scattering on plane shock fronts the energy gain is positive and linear in β. In contrast, the energy gain from scattering on gas clouds scales with β^2. For this reason the two processes are also named first and second order Fermi acceleration, respectively. Since $\beta < 1$ it is obvious from Eq. 2.16 and Eq. 2.17 that first order Fermi acceleration is the more efficient mechanism. Therefore, in the following only first order Fermi acceleration is considered.

The last step is to calculate the spectral index γ via Eq. 2.7, for which the escape probability has to be assessed. Particles escape the acceleration region by traversing the shock to the downstream region and then being carried away through convection. When the number density of particles is ρ_{CR}, the rate of particles crossing the plane shock is again obtained through projecting the isotropic flux onto the plane:

$$\int_0^1 \mathrm{d}\cos\theta \int_0^{2\pi} \mathrm{d}\phi \frac{c\rho_{\mathrm{CR}}}{4\pi}\cos\theta = \frac{c\rho_{\mathrm{CR}}}{4}. \tag{2.18}$$

In the rest frame of the shock the gas flows downstream with velocity u_2. Therefore, a fraction of the particles is carried away from the shock through convection at a rate $\rho_{\mathrm{CR}}u_2$ and the escape probability calculates to:

$$P_{\mathrm{esc}} = \frac{\rho_{\mathrm{CR}}u_2}{c\rho_{\mathrm{CR}}/4} = \frac{4u_2}{c}, \tag{2.19}$$

and the spectral index is:

$$\gamma = \frac{P_{\mathrm{esc}}}{\xi} = \frac{3}{u_1/u_2 - 1}. \tag{2.20}$$

Since the flow of particles across the shock must obey mass conversation ($\rho_1 u_1 = \rho_2 u_2$), the

velocities $u_{1,2}$ are linked to the gas densities $\rho_{1,2}$ before and after the shock [34]:

$$\frac{u_1}{u_2} = \frac{\rho_2}{\rho_1} = \frac{(c_p/c_v + 1)}{(c_p/c_v - 1) + 2/M^2}, \tag{2.21}$$

where c_p/c_v is the specific heat ratio and $M = u_1/c_1$ is the Mach number in a medium with the speed of sound c_1. For an ideal, monoatomic gas the specific heat ratio is related to the degrees of freedom f by $c_p/c_v = 1 + 2/f = 5/3$. Assuming a very strong shock ($M \gg 1$) the density ratio in Eq. 2.21 becomes $\rho_2/\rho_1 = 4$ resulting in an index of the energy spectrum of $\gamma \approx 1$. Finally, the differential energy spectrum calculates to:

$$\frac{dN}{dE} \propto \left(\frac{E}{E_0}\right)^{-2}. \tag{2.22}$$

To conclude, the diffuse shock acceleration as outlined above results in an energy spectrum following a power law. For strong shocks an index of about -2 is expected. This is the general picture of the acceleration process. Particular aspects of this process are more involved, like for example the way how particles are injected into the acceleration process, how they stay confined and how the accelerated particles influence or even enhance the environment in which acceleration takes place [35].

2.1.2 The connection between cosmic rays and high-energy neutrinos

The last section described the diffuse shock acceleration as the likely process through which cosmic rays attain their energy. Consequently, the focus now shifts to the astrophysical objects which are thought to be cosmic ray sources. However, before discussing source classes an important connection needs to be highlighted.

If an astrophysical object would be a hadronic accelerator it would also be a source of high-energy neutrinos. The accelerated particles would interact with the ambient matter and radiation fields surrounding the source [36]. Through proton-photon ($p\gamma$) and proton-proton (pp) interactions pions would inevitably be created:

$$p\gamma \;\rightarrow\; \Delta^+ \rightarrow \begin{cases} \pi^0 + p \\ \pi^+ + n \end{cases} \tag{2.23}$$

$$pp \;\rightarrow\; \begin{cases} \pi^0 + X \\ \pi^\pm + X \end{cases}. \tag{2.24}$$

Neutral pions decay immediately into gamma rays:

$$\pi^0 \to \gamma\gamma, \tag{2.25}$$

whereas in the decays of charged pions neutrinos are produced:

$$\pi^+ \to \mu^+\nu_\mu \to e^+\nu_e\bar{\nu}_\mu\nu_\mu, \tag{2.26}$$

$$\pi^- \to \mu^-\bar{\nu}_\mu \to e^-\bar{\nu}_e\nu_\mu\bar{\nu}_\mu. \tag{2.27}$$

From these decay chains neutrinos emerge at a ratio of $\nu_e : \nu_\mu : \nu_\tau = \bar{\nu}_e : \bar{\nu}_\mu : \bar{\nu}_\tau = 1 : 2 : 0$. In the interactions of Eq. 2.23 also heavier mesons can be created. The decay chain of Eq. 2.26 exists also for charged kaons, so these would also produce ν_e and ν_μ. Charmed mesons could also decay to ν_τ. However, because of the higher energy threshold and lower cross-section of charmed meson production the ν_τ flux at the source is considered negligible compared to the ν_e and ν_μ produced from pion decays.

Cosmic rays are deflected by magnetic fields on their path from the source to Earth. Therefore, hints for the cosmic ray sources are obtained from the arrival directions at Earth only for the highest-energetic and therefore most rigid cosmic rays. In contrast, neutrinos are electrically neutral and hence not affected by magnetic fields. Due to their low interaction probabilities they escape even dense environments unhindered and are also not absorbed on their way from the source to Earth. The neutrino production in cosmic ray sources as well as their beneficial properties as messenger particles are the reasons why neutrino astronomy holds out the prospect to answer the question about the cosmic ray sources.

2.2 Sources of High Energy Neutrinos

In the following classes of astrophysical objects which are considered source candidates of both cosmic rays as well as high-energy neutrinos are discussed.

2.2.1 Hillas Criterion

What kind of astrophysical objects are thought capable of accelerating particles to the highest observed energies? Hillas [37] pointed out that in order to magnetically confine the particle during its acceleration the acceleration region must be larger than the particle's gyroradius r_g (see Eq. 2.2). From this the maximum energy attainable in an accelerator of size L is:

$$E_{\max} = ze\beta BL. \tag{2.28}$$

This criterion does not only hold for Fermi acceleration but also for one-shot acceleration scenarios in which the particles attain energy in the electric field E induced in a conductor moving through a magnetic field at velocity $U = \beta c$. Pulsars, i.e. fast spinning, magnetized neutron stars fall into this category. Rewriting the induction law of the Maxwell equations to orders of magnitude the electric field E is about [34]:

$$\nabla \times \boldsymbol{E} = -\frac{\partial \boldsymbol{B}}{\partial t} \rightarrow \frac{E}{L} \sim \frac{B}{L/U} \rightarrow E \sim BU. \tag{2.29}$$

The energy attained by a particle of charge ze in this field calculates to:

$$E_{\max} = \int zeEdx = ze\beta BL. \tag{2.30}$$

Hence, to accelerate particles beyond a particular energy for both acceleration scenarios a lower bound on the product BL exists. Because $E_{\max}$ is proportional to the charge z the bound is lowered for heavier elements. The Hillas criterion is illustrated in Figure 2.3 in which for several candidate sources typical values of B and L are plotted. In order to accelerate protons or iron atoms to the highest observed energies of 100 EeV a source must be located to the upper right of the solid or dashed line, respectively. Extragalactic sources like Active Galactic Nuclei (AGNs) and Gamma Ray Bursts (GRBs) as well as strongly magnetized pulsars are considered to be able to reach these energies. While galactic sources like supernova remnants (SNRs) are not expected to reach the highest energies, their contribution to the cosmic ray flux at lower energies is thought to be significant.

2.2.2 Galactic Sources

Young supernova remnants (SNRs) are thought to be the major source of galactic cosmic rays [38]. One reason is that supernovae provide enough power to explain the energy observed in cosmic rays. The energy density in cosmic rays observed close to Earth is $\rho_E = 1\,\mathrm{eV/cm^3}$ [33]. Assuming that the energy density is homogeneous throughout the galactic disc this amounts to

$$E = d\pi R^2 \rho_E = \pi(200\,\mathrm{pc})(15\,\mathrm{kpc})^2(1\,\mathrm{eV/cm^3}) \approx 7 \cdot 10^{54}\,\mathrm{erg}. \tag{2.31}$$

Cosmic rays diffuse through the galaxy for about $\tau = 6 \cdot 10^6\,\mathrm{yr}$ before they leak to the intergalactic space. Hence, the power necessary to maintain the energy density is:

$$L_{CR} = \frac{E}{\tau} \approx 5 \cdot 10^{40}\,\mathrm{erg/s}. \tag{2.32}$$

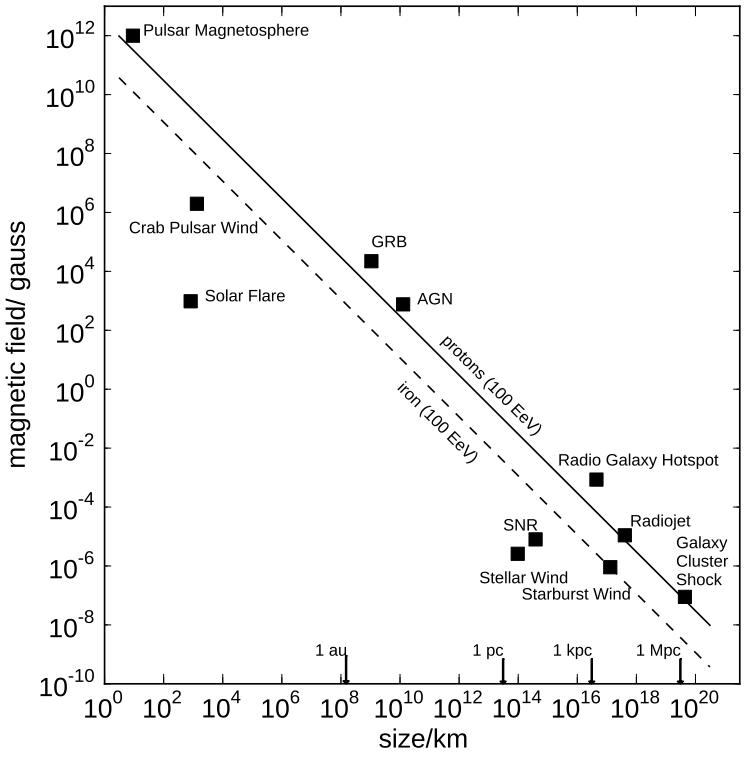

Figure 2.3: Hillas plot after [37] with data taken from [34].

The kinetic energy in $10M_\odot$ of material ejected at a velocity of 5000 km/s amounts to $E_{SN} = 2.5 \cdot 10^{51}$ erg. With about three galactic supernovae per century this contributes a power of:

$$L_{SN} \approx 3 \cdot 10^{42} \text{erg/s}. \tag{2.33}$$

So only a small fraction of the released energy would be sufficient to fulfill the power requirements of cosmic rays.

Observations with air Cherenkov telescopes identified SNRs as sources of TeV gamma rays which substantiated the idea of particles being accelerated to energies beyond 100 TeV in the blast waves [39]. However, the energy spectra obtained from such measurements did not allow to conclusively identify SNRs as hadronic accelerators, i.e. as sources of cosmic rays. In case of hadronic acceleration the gamma rays are explained through proton-proton interactions with the matter surrounding the progenitor star. In this reaction neutral pions are created which

instantly decay into gamma rays (see Eq. 2.25). However, purely leptonic accelerators remained a viable explanation. Relativistic leptons also produce gamma rays through bremsstrahlung and inverse Compton scattering. At lower energies a distinction between these two scenarios became possible for the two objects IC 443 and W44 through data taken with the Fermi Large Area Telescope. The gamma-ray energy spectrum resulting from pion decays provides a characteristic signature in form of a symmetric bump around half the pion rest mass $\frac{1}{2}m_{\pi^0} = 67.5\,\mathrm{MeV}$ which is difficult to fit with leptonic models. By observing this feature Fermi provided direct evidence that cosmic-rays were accelerated to GeV energies in SNRs [40].

Another class of galactic cosmic ray sources are pulsars. They are formed during the death of spinning magnetized stars. When the fusion processes in these stars come to an end the radiation pressure vanishes and the star contracts. The conserved angular momentum and magnetic field of the progenitor star result in a rapidly spinning neutron star with radii of about 10 km, rotation periods of the order of milliseconds and strong magnetic fields of about $10^{12}\,\mathrm{G}$ [38]. In the pole region of pulsars electrostatic particle acceleration could accelerate cosmic rays to energies beyond the knee.

Binary systems with strong x-ray emission are also believed to contribute to the cosmic-ray flux above the knee. They comprise a neutron star or a black hole which accretes matter from an accompanying star. At the compact object relativistic jets are formed through which the gravitational energy from the infalling matter is released. This setup resembles active galactic nuclei which are discussed in the next section.

2.2.3 Extragalactic sources

Gamma-ray bursts (GRBs) are outbreaks of intense gamma radiation over short time spans of only a few seconds. They are thought to originate from blast waves emerging from the collapse of massive stars or the merger of compact objects like neutron stars or black holes [41]. The bursts are distributed isotropically over the sky and from observations in other wavelengths it is known that the radiation origins from objects at cosmological distances. GRBs are the most energetic electromagnetic explosions in the universe, given that despite the large distances GRBs outshine any other source of gamma-rays in the sky. If the energy released would be emitted isotropically one of the brightest GRBs observed to date would have released $E_{\mathrm{iso}} \approx 8.8 \cdot 10^{54}\,\mathrm{erg}$, or 4.9 times the Solar rest energy [42]. This energy requirement would be mitigated if the blast wave powering the gamma-ray emissions would be collimated into a narrow jet. In these jets Fermi accelerated electrons could create the gamma-rays through synchrotron radiation or inverse Compton scattering. If additionally protons and heavier nuclei would be accelerated in these jets, neutrinos would also be produced. The neutrinos would again stem from the

decays of charged mesons (see Eq. 2.23). These could either be produced in $p\gamma$-interactions with synchrotron photons or, in the scenario of a collapsing star, through pp-interactions between those protons accelerated in the jet and those in the collapsing hull.

Given the immense energy release GRBs are considered likely sources of the highest energetic cosmic rays. As a consequence they are also considered to be strong neutrino sources [43]. By now the neutrino detection capabilities at Earth evolved so far that these predictions are in range. The non-observation of neutrinos in association with GRBs so far disproved the earliest predictions [44].

Active galactic nuclei (AGNs) are the cores of active galaxies exhibiting strong non-thermal electromagnetic radiation. In the prevailing picture their emission is thought to be powered by the gravitational energy of a supermassive black hole at the center of these galaxies [45]. Matter falling into the core forms an accretion disc around the black hole. Through dissipative processes the accretion disc heats up and glows brightly at ultraviolet wavelength. Near the black hole inverse Compton scattering on relativistic electrons results in hard X-ray emission. Observations of the optical and ultraviolet radiation can be obscured by a torus of gas and dust in the same plane as the accretion disc. Along the rotation axis of the accretion disc a collimated outflow of matter forms jets which can exhibit very strong radio emission. Gas moves in these jets at relativistic velocities leading to the emission of electromagnetic radiation up to gamma rays which in addition is strongly beamed forward. Depending on the orientation of this axis to the line of sight of the observer the appearance of AGNs can be significantly different. So-called blazars are particular luminous AGNs for which the jet points in the direction of the observer. The emission of blazars varies over times. They exhibit flaring periods [46] and variability of the order of minutes has been observed in gamma-rays [47]. The extreme luminosities and short time-scale variability can be explained with compact blobs of gas propagating at relativistic velocities through the jet towards the observer [34].

If hadrons would also be efficiently accelerated in the jets then AGNs would also qualify as likely sources of the highest energetic cosmic rays and consequently as candidate neutrino sources [48, 49].

2.2.4 Diffuse Astrophysical Neutrino Flux

So far no point-source of high-energy neutrinos has been identified [50]. While individual neutrino sources might be too weak to be detectable with current instruments, they would still contribute to a collective astrophysical neutrino flux.

The highest-energetic cosmic rays are thought to be of extra-galactic origin because of their large gyro-radii. They provide a possibility to estimate an upper bound on the extragalactic

component of the diffuse neutrino flux. This argument was originally presented by Waxman and Bahcall [51, 52]. From cosmic-ray measurements the energy production rate of protons $\dot{\epsilon}_{\mathrm{CR}}^{[10^{19},10^{21}]}$ in the energy range $10^{19}\,\mathrm{eV}$ to $10^{21}\,\mathrm{eV}$ is known. Assuming an injection spectrum $dN_{\mathrm{CR}}/dE_{\mathrm{CR}} \propto E_{\mathrm{CR}}^{-2}$ from diffuse shock acceleration (see Section 2.1.1) the energy-dependent generation rate of cosmic rays in the source calculates to:

$$E_{\mathrm{CR}}^2 \frac{d\dot{N}_{\mathrm{CR}}}{dE_{\mathrm{CR}}}\bigg|_{10^{19}\,\mathrm{eV}} = \frac{\dot{\epsilon}_{\mathrm{CR}}^{[10^{19},10^{21}]}}{\ln\left(10^{21}/10^{19}\right)} \approx 0.5 \cdot 10^{44}\,\mathrm{erg Mpc^{-3} yr^{-1}}. \tag{2.34}$$

From this the flux of muon neutrinos calculates to:

$$E_\nu^2 \frac{dN_\nu}{dE_\nu dA d\Omega dt} \approx \frac{1}{4}\epsilon t_H \frac{c}{4\pi} \xi_Z E_{\mathrm{CR}}^2 \frac{d\dot{N}_{\mathrm{CR}}}{dE_{\mathrm{CR}}} \approx 10^{-8} \xi_{\mathrm{Z}}\,\mathrm{GeV sr^{-1} s^{-1} cm^{-2}}, \tag{2.35}$$

where the Hubble time $t_H \approx 10^{10}\,\mathrm{yr}$, c is the speed of light and the factor $\epsilon \leq 1$ denotes the fraction of energy cosmic rays lose before escaping the source. About half of the pions created in pp interactions in the source create neutral pions which do not produce neutrinos. For the charged pions about half of their energy is transfered to muon neutrinos. Both effects are accounted for by the factor 1/4. The factor ξ_Z accounts for the effect that the generation of cosmic-rays evolved during the cosmic evolution. An increase of the neutrino flux up to a factor of $\xi_Z = 3$ is estimated from this effect [51].

Finally, to obtain the Waxman-Bahcall upper bound $\epsilon = 1$ is assumed and a factor 1/2 is applied to account for neutrino oscillations from the source to Earth (see Section 2.3). Another factor of 3 is applied to transform the ν_μ flux from Eq. 2.35 to an all-flavor flux:

$$E_\nu^2 \Phi_{\mathrm{WB}} \leq \frac{3}{2} E_\nu^2 \frac{dN_\nu}{dE_\nu dA d\Omega dt} \approx 3 \cdot 10^{-8}\,\mathrm{GeV sr^{-1} s^{-1} cm^{-2}}. \tag{2.36}$$

2.2.5 Cosmogenic Neutrinos

The Greisen-Zatsepin-Kuzmin cutoff mentioned in the beginning of this chapter gives also rise to a flux of neutrinos. Through interactions with photons of the cosmic microwave background cosmic rays produce pions via the Δ^+-resonance (see Eq. 2.23). In the decays of the pions neutrinos are produced. A particular advantage of these so-called cosmogenic or GZK neutrinos is that they form a guaranteed flux of neutrinos. Model predictions range in energy from $10^7\,\mathrm{GeV}$ up to $10^{12}\,\mathrm{GeV}$ [53], which is above the energy range on which this thesis focusses.

2.3 Neutrino Oscillations

When neutrinos are created and detected in weak interactions their flavor is defined through the corresponding lepton in the interaction. Unlike other leptons neutrinos exhibit the ability to change the flavor between creation and detection. These so-called neutrino oscillations were observed with neutrinos originating in the sun [54–56], the atmosphere [57] and man-made neutrino sources at Earth like nuclear reactors [58, 59] and particle accelerators [60].

Neutrino oscillations are connected to neutrino mass. When neutrinos are created in a weak interaction they are created as eigenstates $|\nu_\alpha\rangle$, $\alpha = e, \mu, \tau$, of an operator measuring flavor. However, the time development of a quantum mechanical state is governed by the mass eigenstates $|\nu_j\rangle$, $j = 1, 2, 3$. The flavor eigenstates are representable as a superposition of mass eigenstates:

$$|\nu_\alpha\rangle = U_{\alpha j} \, |\nu_j\rangle \, . \tag{2.37}$$

The coefficients of the matrix $U_{\alpha j}$ describe the neutrino mixing and the time evolution of the flavor eigenstates can be written as [36]:

$$|\nu_\alpha(t)\rangle = \sum_{j=1,2,3} U_{\alpha j} \exp\left(-iE_j t\right) |\nu_j\rangle \, . \tag{2.38}$$

The E_j denote the energies of the mass eigenstates. Because the matrix is unitary $U_{\alpha j}$ can be parametrized by three angles θ_{12}, θ_{23} and θ_{13} and a CP-violating phase δ:

$$U = \begin{pmatrix} c_{12}c_{13} & s_{12}c_{13} & s_{13}e^{-i\delta} \\ -s_{12}c_{23} - c_{12}s_{23}s_{13}e^{i\delta} & c_{12}c_{23} - s_{12}s_{23}s_{13}e^{i\delta} & s_{23}c_{13} \\ s_{12}s_{23} - c_{12}c_{23}s_{13}e^{i\delta} & -c_{12}s_{23} - s_{12}c_{23}s_{13}e^{i\delta} & c_{23}c_{13} \end{pmatrix}, \tag{2.39}$$

where $s_{ij} = \sin(\theta_{ij})$, $c_{ij} = \cos(\theta_{ij})$. The probability to have a neutrino of flavor α and created at time $t = 0$ to be observed at a later time t as a neutrino of flavor β is then:

$$\begin{aligned} P_{\nu_\alpha \to \nu_\beta} &= |\langle \nu_\beta(t) | \nu_\alpha(t=0) \rangle|^2 \\ &= \delta_{\alpha\beta} - 4 \sum_{\substack{i,j \\ j>i}} Re(U^*_{\alpha i} U_{\beta i} U_{\alpha j} U^*_{\beta j}) sin^2 \left(\frac{\Delta m^2_{ij} L}{4E_\nu} \right) \\ &\quad + 2 \sum_{\substack{i,j \\ j>i}} Im(U^*_{\alpha i} U_{\beta i} U_{\alpha j} U^*_{\beta j}) sin^2 \left(\frac{\Delta m^2_{ij} L}{4E_\nu} \right) \end{aligned} \tag{2.40}$$

For neutrinos origination from beyond the solar system L/E is large and the sin^2 terms in

Eq. 2.40 average to 1/2 [36, 61]. As argued in Section 2.1.2 the astrophysical neutrinos are thought to originate mostly from pion decays. At the source these decays result in a flavor ratio of $\nu_e : \nu_\mu : \nu_\tau = 1 : 2 : 0$ with twice as many muon neutrinos as electron neutrinos, no tau neutrinos and equal amounts of neutrinos and anti-neutrinos. From the NuFIT 1.3 global fit to neutrino oscillation experimental data the following 3σ intervals are estimated for the mixing parameters: $31.3° \leq \theta_{12} \leq 35.9°$, $38.4° \leq \theta_{23} \leq 53.3°$, $7.87° \leq \theta_{13} \leq 9.11°$ and $0° \leq \delta \leq 360°$ [62]. The interval of δ spans the whole domain, so $\delta_{CP} = 0$ is assumed here. With Eq. 2.40 the expected flavor ratio at Earth calculates then to:

$$\begin{pmatrix} \nu_e \\ \nu_\mu \\ \nu_\tau \end{pmatrix}_{\text{Earth}} = P_{\alpha\beta} \cdot \begin{pmatrix} \nu_e \\ \nu_\mu \\ \nu_\tau \end{pmatrix}_{\text{Source}} = \begin{pmatrix} 0.55 & 0.22 & 0.23 \\ 0.22 & 0.41 & 0.37 \\ 0.23 & 0.37 & 0.41 \end{pmatrix} \cdot \begin{pmatrix} 1 \\ 2 \\ 0 \end{pmatrix} = \begin{pmatrix} 0.99 \\ 1.05 \\ 0.96 \end{pmatrix} \tag{2.41}$$

Due to neutrino oscillations the flavor ratio transforms to a balanced ratio of about 1 : 1 : 1. One consequence is that despite the vanishing low production of tau neutrinos at the source they nevertheless make up one third of the astrophysical neutrino flux at Earth. Neutrino detectors like IceCube are able to discriminate flavors to some extent (see Section 3.5). The equalised flavor ratio is a direct consequence of the assumed neutrino production in pion decays. Therefore, measurements of the flavor ratio at Earth are expected to yield insights into neutrino production mechanisms if a different or energy-dependent constitution of the astrophysical neutrino flux should be found [63].

2.4 Atmospheric neutrinos

Depending on the parent mesons two classes of atmospheric neutrinos have to be distinguished. Those originating from decays of pions and kaons are called conventional atmospheric neutrinos. Their parent mesons' lifetimes are long enough for some of them to re-interact with another air nuclei instead of decaying. The spectrum of conventional atmospheric neutrinos results from this competition between either decaying or re-interacting. The second class consists of neutrinos produced in the decay of charmed mesons. These mesons are short-lived and decay practically immediately, which has led to the name prompt atmospheric neutrinos.

The general properties of the atmospheric neutrino spectrum can be illustrated with an analytic approximation. The atmospheric muon neutrino spectrum at the Earth's surface dN_ν/dE

as a function of neutrino energy E_ν and zenith angle θ is given by [33]:

$$\frac{dN_\nu}{dE}(E_\nu) = \frac{dN_N}{dE}(E_\nu) \times \left\{ \frac{A_{\pi\nu}}{1 + B_{\pi\nu} cos(\theta) E_\nu/\epsilon_\pi} + \frac{A_{K\nu}}{1 + B_{K\nu} cos(\theta) E_\nu/\epsilon_K} + \frac{A_{\mathrm{D}\nu}}{1 + B_{\mathrm{D}\nu} cos(\theta) E_\nu/\epsilon_\mathrm{D}} \right\}. \tag{2.42}$$

The three summands describe the contribution of pions, kaons and charmed mesons, respectively. Each is proportional to the cosmic ray spectrum $dN_N/dE \propto E^{-\alpha}$, $\alpha \approx 2.7$. The factors $A_{i\nu}$ and $B_{i\nu}$, $i = \pi^\pm, K^\pm, D^\pm$ contain the physics of meson production and decay. They do not depend on the energy. The energy behaviour of the three fractions is controlled by the critical energies ϵ_i:

$$\epsilon_\pi = 115\,\mathrm{GeV} \quad \epsilon_K = 850\,\mathrm{GeV} \quad \epsilon_D \approx 4.3 \cdot 10^7\,\mathrm{GeV} \tag{2.43}$$

At energies exceeding $\epsilon_i/\cos(\theta)$, time dilatation sufficiently increased the mean distance particles travel before decaying so that they are more likely to interact instead. Therefore, while at lower energies the neutrino spectrum follows the cosmic-ray spectrum, at higher energies the spectrum becomes steeper by another factor E^{-1}.

At the energies relevant in the following ($>$ TeV) the majority of the muon neutrinos originate from kaon decays and have a steepened spectrum with index of about -3.7. In contrast the spectrum of prompt neutrinos follows the harder cosmic ray spectrum. Eventually, the prompt neutrinos exceed the conventional atmospheric neutrinos. A hardening of the atmospheric neutrino spectrum is expected at the energy where this transition takes place.

The flux of conventional electron neutrinos is lower than the flux of muon neutrinos. They originate from the decay $K_0^L \to \pi e \nu_e$ as well as from the second step in in the pion and kaon decay chains shown in Eq. 2.26, yielding a ratio of electron to muon neutrinos of $\lessapprox 5\%$ [64]. In contrast, the fluxes of prompt electron and muon neutrinos are identical because charmed mesons are equally likely to decay into electrons or muons. Prompt ν_τ would originate from D_S decays but their flux is expected to be more than an order of magnitude smaller than the other prompt neutrinos [65]. One implication of these flavor ratios is that the transition, in which the contribution of prompt neutrinos exceeds the conventional ones, occurs at lower energies for electron neutrinos than for muon neutrinos.

The fluxes of conventional and prompt neutrinos also depend differently on the zenith angle. The distance between the cosmic-ray interaction height and a detector at ground increases with zenith angle. Particles created in horizontal air showers have a longer distance available to decay. Therefore, the flux of conventional neutrinos arriving horizontally is enhanced. A similar enhancement of the horizontal flux does not occur for prompt neutrinos as their parent mesons

decay immediately [65].

The analytical approximation in Eq. 2.42 is useful to describe the general features of the atmospheric neutrino spectrum. However, in the following for the conventional neutrinos the predictions of the HKKMS07 calculation [66] is used. Starting from the primary cosmic ray spectrum these calculations incorporate simulations of the hadronic interactions and trace the propagation of the air shower through the atmosphere. A three-dimensional atmosphere is modeled in order to account for the effect of the geomagnetic field on lower energetic charged particles. The calculations reach up to 10 TeV and have to be extrapolated to higher energies. The atmospheric neutrino flux predicted by these extrapolations has been experimentally verified by IceCube both for muon [16, 67] and electron neutrinos [68]. The original HKKMS06 model does not account for the knee in the cosmic ray spectrum. In order to include the knee a modification of the atmospheric neutrino predictions is used [16, 69].

Predictions for the prompt atmospheric neutrino flux are much less certain. Their intensity has not been measured yet and uncertainties in the relevant production cross-sections lead to large uncertainties in the predicted flux. In the following the ERS calculation [65] will be used as the benchmark. Here, a pertubative quantum chromodynamics approach is used to estimate the charm production from partonic processes like $gg \to c\bar{c}$. Key ingredients in these calculations are the parton distribution functions (PDFs). In the quark parton model the partons are thought to carry a fraction x of the proton's total momentum and the PDFs give the probability that two partons encounter each other with particular momentum fractions. The PDFs are not directly measurable and especially the distributions for small values of x are insufficiently constrained through collider experiments [70]. Since especially the PDFs at small values of x provide dominant contributions to the charm production cross-section the uncertainties of small x physics transform into uncertainties of the prompt atmospheric neutrino flux. An upper limit on the prompt neutrino flux has been derived in [16]. The flux is constrained to be lower than 3.8 times the prediction of the ERS calculation.

2.5 Evidence of the diffuse astrophysical neutrino flux

During the preparation of this thesis analyses performed with data taken over two years with the completed cubic kilometer IceCube detector have established evidence for the diffuse astrophysical neutrino flux [1, 10]. Its spectrum is compatible with the expected E^{-2} power law with an estimated all-flavor intensity of:

$$E_\nu^2 \frac{dN}{dEdtdAd\Omega} = (3.6 \pm 1.4) \cdot 10^{-8}\,\mathrm{GeVsr^{-1}s^{-1}cm^{-2}}. \tag{2.44}$$

The sample included two events at PeV energies. Neutrinos of these energies had never been observed before. If the diffuse neutrino flux would follow an unbroken power law, additional $3-6$ events in the 2 to 10 PeV range would have been expected. Since these were not found, the diffuse spectrum could either exhibit a cutoff at PeV energies or the spectrum could generally be softer. The best fit to the spectrum is $\Phi_\nu \propto E^{-2.2\pm0.4}$.

No significant clustering of the observed events or correlation with source candidates was found so the diffuse flux is still consistent with an isotropic flux. The observed flavor ratio is compatible with $1:1:1$ which matches the expectations from neutrino production in pion decays and neutrino oscillations between the source and Earth (see Section 2.1.2 and Section 2.3). A follow-up analysis added another year of IceCube data and consolidated this picture [71].

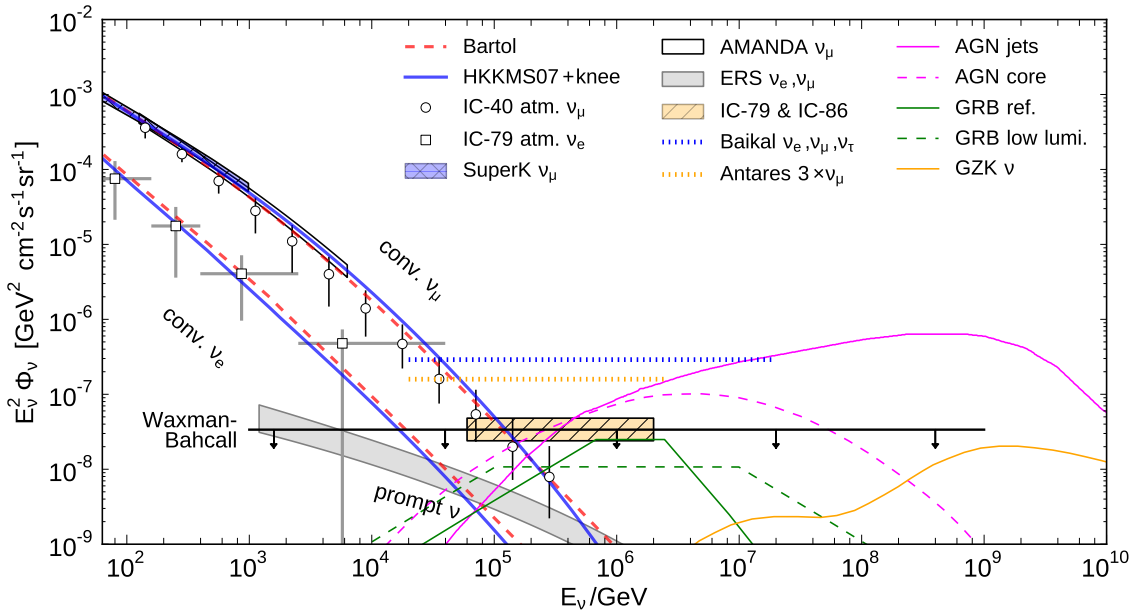

Figure 2.4: Measured and predicted high-energy neutrino fluxes. The measurements of the atmospheric neutrino flux are: IC-40 atm. ν_μ [67], IC-79 atm. ν_e [68], Amanda ν_μ [72] and SuperK ν_μ [73]. The corresponding model predictions are Bartol [74], HKKMS07 + knee [16,66,75] and ERS ν_e, ν_μ [65]. Constraints on the astrophysical diffuse neutrino flux are obtained from Baikal [76] and Antares [77]. The flux has been measured by IC-79 & IC-86 [1]. The shown theoretical neutrino flux predictions for GRBs and AGNs are obtained from Ref. [78]. The Waxman-Bahcall bound [51, 52] is shown as well as a prediction for GZK neutrinos [53].

3 Neutrino Detection and the IceCube Experiment

Neutrinos are very elusive particles as they are only subject to the weak interaction and gravitation. In the context of neutrino detectors the effect of gravitation is too small to be relevant. Hence, in order to directly detect neutrinos they have to weakly interact with matter. In collider experiments neutrinos can also be detected indirectly. Since in these experiments the kinematics are well under control, produced neutrinos that escape the instrument undetected reveal themselves as missing energy. But neutrino telescopes aim at measuring a neutrino flux of uncertain intensity and energy spectrum. So a direct detection method is needed.

In the following the principles of high-energy neutrino detection and their application in the IceCube instrument will be discussed. At first neutrino interactions in matter are discussed. Afterwards the relevant physics processes of secondary particles passing through matter are described. Then the IceCube experiment is introduced and its different detection channels are presented.

3.1 Neutrino Cross-Sections

In the Standard Model of particle physics weak interactions are mediated through the exchange of $W^{\pm}$ and Z^0 gauge bosons. Accordingly, two interaction scenarios are possible. The charged-current (CC) exchange, mediated through $W^{\pm}$ bosons, and the neutral-current (NC) exchange mediated through Z^0 boson. Neutrinos can thus be scattered from other leptons and nuclei. In the case of scattering on nuclei it depends on the neutrino energy at which length scales the scattering target is probed. With rising energy a transition takes place from neutrino interactions with the whole nucleus to scattering on constituents within [79].

Above TeV energies the dominant reaction is deep-inelastic neutrino-nucleon scattering, where the neutrinos scatter on quarks inside nucleons:

$$\nu_l + N \rightarrow \quad l + X \qquad (CC) \tag{3.1}$$

$$\nu_l + N \rightarrow \quad \nu_l + X \qquad (NC). \tag{3.2}$$

Figure 3.1 shows the Feynman diagrams for both interaction scenarios. In the CC reaction the $W^{\pm}$ exchange transforms the incident neutrino ν_l into its corresponding partner lepton l. As a consequence the final state of the reaction contains an electron, muon or tau-lepton as well as a hadronic system X that instantly develops into a hadronic particle shower as quarks recombine. In the case of a NC reaction the incident neutrino does not transform and the final state contains the neutrino and a hadronic shower. In CC reactions all of the neutrino energy is distributed over the lepton and the hadronic shower. Therefore, the energy is in principle measurable. In NC reactions only a part of the energy is deposited in the hadronic shower, whereas the remainder is carried away by the neutrino.

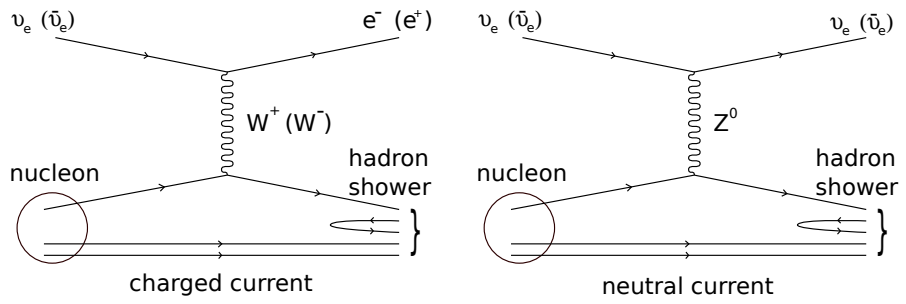

Figure 3.1: Feynman diagrams of deep inelastic neutrino-nucleon scattering.

The cross-section for a neutrino with energy E_ν to interact with an isoscalar nucleon, i.e. a nucleon with equal number of protons and neutrons, has been calculated in [81]:

$$\frac{d^2\sigma}{dxdy} = \frac{G_F^2 M E_\nu}{\pi} \begin{cases} 2\left(\frac{M_W^2}{Q^2+M_W^2}\right)^2 \left[xq(x,Q^2) + x\overline{q}(x,Q^2)(1-y)^2\right] & (CC) \\ \frac{1}{2}\left(\frac{M_Z^2}{Q^2+M_Z^2}\right)^2 \left[xq^0(x,Q^2) + x\overline{q^0}(x,Q^2)(1-y)^2\right] & (NC) \end{cases} \tag{3.3}$$

where M, M_W and M_Z are the masses of the nucleon and the mediating bosons and G_F is the Fermi constant. The kinematics of the process are described by the invariant momentum transfer $-Q^2$, the Bjorken variable $x = Q^2/(2M(E_\nu - E_l))$ and the inelasticity $y = (E_\nu - E_l)/E_\nu$,

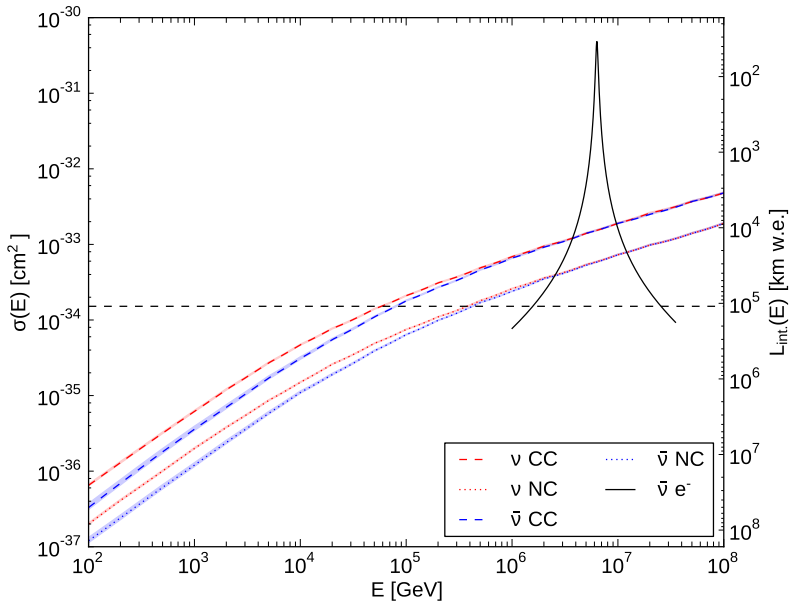

Figure 3.2: Cross-sections for deep inelastic neutrino-nucleon scattering. The plot illustrates calculations based on current collider data [80]. The widths of the plotted bands indicate the estimated uncertainties of the calculation. In addition to the cross-sections of neutrino-nucleon scattering the Glashow resonance at 6.3 PeV is shown. The second axis translates the cross-sections into interaction lengths in units of km water equivalent. A column through the center of the Earth is shown as reference (black dashed line).

where E_l denotes the energy of the emerging lepton.

The parton distribution functions (PDFs) q, q^0 $(\overline{q}, \overline{q}^0)$ describe the probability for the neutrino to probe a quark (anti-quark) with the nucleon momentum fraction x in a collision with moment transfer Q^2. These PDFs, describing the structure of the nucleon, are obtained from collider experiments. With increasing energy the PDFs get sampled at smaller values of x which makes measurements of the PDFs at low x especially important for neutrino telescopes. The analysis presented in this thesis uses a cross-section calculation based on the CTEQ5 PDFs [82] which incorporate measurements down to $x = 10^{-4}$. PDFs derived from the combined results of the HERA experiments (reaching down to $x = 6 \times 10^{-6}$) were used in more recent calculations of the neutrino cross-sections [80]. The cross-sections of this recent calculation as well as their uncertainties are shown as a function of neutrino energy in Figure 3.2. In the TeV- PeV range, which is important for this thesis, the CTEQ5-based cross-sections and those plotted in Figure 3.2

agree within the shown uncertainty band.

At lower energies the cross-section scales linearly with the neutrino energy E_ν. Above $\approx 10\,\mathrm{TeV}$ the propagator term $\propto (Q^2/M_{W,Z}^2 + 1)^{-2}$ restricts Q^2 close to M_W^2. This dampens the contribution of a large area of the kinematically allowed phase space and flattens the rise of the cross-section with energy. Up to PeV energies the cross-section for anti-neutrinos is generally lower than for neutrinos, because the parton distribution functions are dominated by the valence quarks and the contribution of anti-quarks is dampened by the $(1-y)^2$ factor in Eq. 3.3. With higher energies the neutrino is more likely to probe also sea quarks and the cross-sections for νN and $\overline{\nu} N$ scattering become equal.

Similar to νN scattering, the cross-section for νe scattering is proportional to the target mass. With the electron mass M_e being much smaller than the nucleon mass M, νe scattering can be ignored for most of the energy range. There is one exception in form of the so-called Glashow resonance [83]:

$$\overline{\nu}_e + e^- \rightarrow W^- \rightarrow \text{anything} \tag{3.4}$$

at $E_\nu = \frac{M}{2M_e} = 6.3\,\mathrm{PeV}$. At this resonance the cross-section is two orders of magnitude larger than for neutrino nucleon scattering.

In order to put the size of the cross-sections into perspective it is helpful to translate them into interaction lengths in a material:

$$L_{\text{int.}} = \frac{A}{\sigma N_A \rho}, \tag{3.5}$$

where $N_A = 6.022 \times 10^{23}\,\mathrm{mol}^{-1}$ is the Avogadro constant and the material is characterized by the atomic mass A and mass density ρ. The second axis in Figure 3.2 shows the interaction length for $A = 1\,\mathrm{gmol}^{-1}$ and the density of water $\rho = 1\,\mathrm{gcm}^{-3}$. According to the Preliminary Reference Earth Model a neutrino travelling through the center of the Earth traverses a column depth of $11\,\mathrm{ktcm}^{-2}$ [84]. That corresponds to $1.1 \times 10^5\,\mathrm{km}$ water equivalent (shown by the black dashed line in Figure 3.2). Above $40\,\mathrm{TeV}$ the interaction length of νN approaches the Earth diameter. With increasing energy neutrinos approaching through the Earth have higher probabilities to interact before reaching the detector and the Earth gets opaque for electron and muon neutrinos. For τ-neutrinos this is mitigated through a process called τ-regeneration. The τ-lepton created in a CC ν_τ interaction decays again into a ν_τ. While the regenerated neutrino carries less energy than the primary neutrino, it still has a chance to reach the detector.

3.2 Interactions of Charged Particles Traversing Matter

After being created in the neutrino interaction the charged particles traverse matter. By interacting with the surrounding material they become measurable and from there inferences on the incident neutrino can be made.

The central process here is the Cherenkov effect by which charged relativistic particles emit light. This makes them detectable in a transparent material instrumented with optical sensors. However, it is not the process trough which the particles dissipate most of their energy. For different particles different energy-loss processes dominate. As a consequence, the secondaries emerging from charged-current neutrino interactions of different flavors exhibit rather different event signatures inside the detector.

3.2.1 Cherenkov Radiation

When charged particles traverse a medium at a velocity $v = \beta c$ larger than the light's phase velocity in this material, they will emit Cherenkov radiation [85]. The phase velocity is $v_p = c/n$, where n is the refractive index of the medium and c the speed of light in vacuum. By traversing the medium, the particle polarizes the electron hulls of atoms in the vicinity of the track [86]. In the following reconciliation they emit electromagnetic radiation. Because of the common source, this radiation is coherent and can constructively interfere. In the Huygens construction shown in Figure 3.3 the particle is a moving emitter of spherical waves which constructively sum up to a notable wavefront. Since the Huygens construction is axially symmetric the light is emitted along the surface of a cone with half-opening angle θ_C (see Figure 3.3).

For θ_C the following relation holds:

$$\cos\theta_C = \frac{v_p}{v} = \frac{1}{\beta n} \leq 1. \tag{3.6}$$

The angle θ_C depends on the particle's velocity and the refractive index of the medium. For example relativistic particles ($\beta \approx 1$) traversing ice ($n \approx 1.31$ at 475 nm) emit Cherenkov radiation at an angle $\theta_C = 40.24°$.

If the particle carries the electric charge ze, the number of photons N_γ emitted with energies in $[E, E + dE]$ per track length dx is given by [87]:

$$\frac{d^2 N_\gamma}{dx dE} = \frac{\alpha z^2}{\hbar c}\left(1 - \frac{1}{\beta^2 n^2}\right), \tag{3.7}$$

where α is the fine structure constant and $\hbar$ is the reduced Planck constant. Two aspects are noteworthy. First, N_γ is proportional to $dE \propto d\nu \propto d\lambda/\lambda^2$, so ultraviolet and blue wavelengths

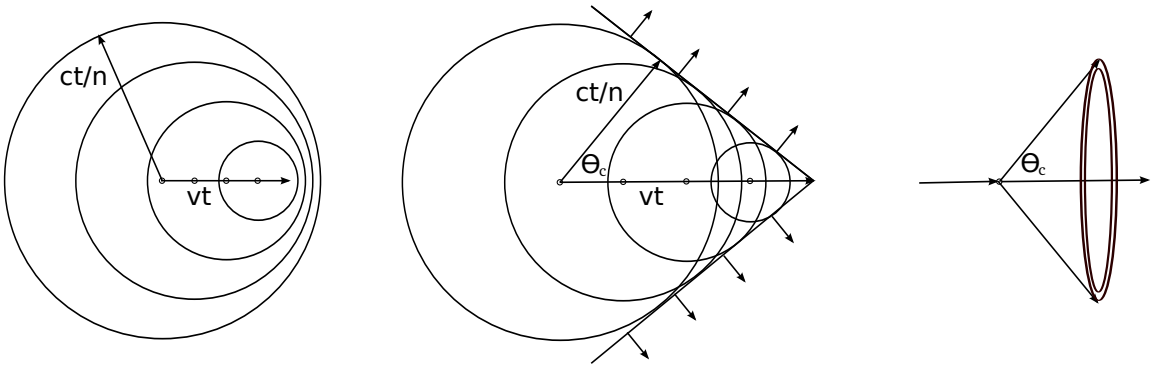

Figure 3.3: Huygens construction of a particle traversing a medium and emitting Cherenkov light. In the left sketch the particle moves slower than the speed of light in the medium, whereas in the center sketch it moves faster. The emitted spherical waves constructively add up to a wavefront emitted in the direction θ_C. The right sketch illustrates that due to axial symmetry the Cherenkov light is emitted along the surface of a cone.

will dominate in a medium transparent for optical and nearby wavelengths. Secondly, if one integrates 3.7 in a given wavelength interval and assumes that $n(\lambda)$ does not vary too much within this interval, one obtains:

$$\frac{dN_\gamma}{dx} = 2\pi\alpha z^2 \int_{\lambda_1}^{\lambda_2} \left(1 - \frac{1}{\beta^2 n^2}\right) \frac{d\lambda}{\lambda^2} \approx 2\pi\alpha z^2 \left(1 - \frac{1}{\beta^2 n^2}\right) \frac{\lambda_1 - \lambda_2}{\lambda_1 \lambda_2} = const., \tag{3.8}$$

i.e the light yield is proportional to the track length. Considering the wavelength interval of $350\,\mathrm{nm} < \lambda < 650\,\mathrm{nm}$ and the refractive index of ice $n \approx 1.31$ the particle emits about 250 photons per cm. In terms of energy loss this amounts to $675\,\mathrm{eVcm}^{-1}$. In comparison to the energy loss of a minimum ionizing particle of $\approx 2\,\mathrm{MeVcm}^{-1}$ this is negligible.

3.2.2 Electromagnetic particle showers

The interplay of two processes, the emission of bremsstrahlung photons by high-energy electrons and the e^+e^- pair production by high-energy photons, leads to electrons and photons creating particle showers [25]. In the presence of the coulomb field of a nearby nucleus a high-energy electron can emit a bremsstrahlung photon. If the photon's energy is larger than twice the electrons rest mass the photon can in turn pair produce an electron and a positron. Since these two energetic particles will emit bremsstrahlung again an avalanche of electrons, positrons and

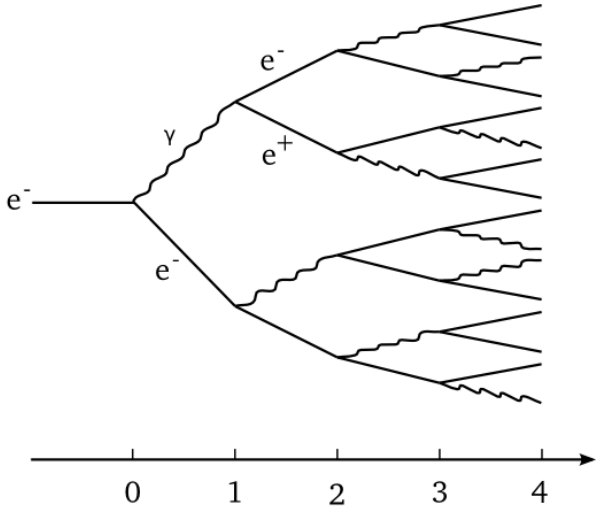

Figure 3.4: Illustration of a simple model to mimic an electromagnetic cascade. After each multiple of the radiation length each electron or positron (straight lines) will emit a bremsstrahlung photon (curly lines) that again creates an e^+e^--pair.

photons is created. This electromagnetic cascade grows as long as the created particles have enough energy to continue the process. At lower energies electrons dissipate their remaining energy mainly through ionization losses and photons through Compton scattering and the photoelectric effect. The threshold energy at which ionization losses become dominant over the bremsstrahlung losses is denoted the critical energy E_c. An approximation formula for E_c in a solid medium with atomic number Z is given in [25]:

$$E_c = \frac{610 \text{ MeV}}{Z + 1.24}. \tag{3.9}$$

The mean free path for high-energy electrons, i.e. the distance after which the energy of electrons is reduced by a factor e, is given by the radiation length X_0. The mean free path for high-energy photons is similar with about $9/7X_0$ [87]. For water the radiation length is $\mathrm{X_0} = 36.08\,\mathrm{gcm}^{-2}$, where the length is quoted in gcm^{-2} of matter traversed.

Because of the similarities in pair production and bremsstrahlung one can describe electromagnetic cascades with a simple model that nevertheless is able to explain characteristics of real electromagnetic cascades [87]. Let the incident electron's energy be E_0. After one radiation length it will emit a photon, which then creates an e^+e^- pair after covering the same distance (see figure 3.4). In each of these processes the energy of the primary particle will be split equally between the two secondaries. Thus, the shower will longitudinally develop in generations with

length t measured in multiples of X_0. In each such generation the number of particles N is doubled:

$$t = \frac{x}{X_0}, \qquad N = 2^t, \qquad E(t) = \frac{E_0}{2^t}. \tag{3.10}$$

In the limit there will be equal numbers of electrons, positrons and photons. This process will continue until the energy $E(t)$ drops below the critical energy E_c. So in the last generation t_{max} the number particles N_{max} is given by:

$$t_{max} = \frac{\ln(E_0/E_c)}{\ln 2}, \qquad N_{max} = \exp(t_{max} \ln 2) = \frac{E_0}{E_c}. \tag{3.11}$$

Thus, the length of the shower scales logarithmically with its energy. Two other important properties can be derived. The total number of particles with energies exceeding E is proportional to the shower energy:

$$N(>E) = \int_0^{t(E)} N dt = \int_0^{t(E)} \exp(t \ln 2) dt = \frac{\exp(t(E) \ln 2) - 1}{\ln 2} \approx \frac{E_0/E}{\ln 2}. \tag{3.12}$$

About 2/3 of the particles are charged so they can emit Cherenkov light. As shown in Eq. 3.8, the number of Cherenkov photons emitted from a charged particle is proportional to its total track length. By integrating the track lengths of all charged particles above the critical energy one obtains the total track length:

$$L = \frac{2}{3} \int_0^{l_{max}} N dt = \frac{2}{3 \ln 2} \frac{E_0}{E_c} \propto \frac{E_0}{E_c}. \tag{3.13}$$

The total track length of all charged particles in the shower is proportional to the energy of the incident electron. Therefore, the Cherenkov light yield of the cascade is proportional to the electrons energy as well. This allows the reconstruction of the deposited energy by counting the number of emitted Cherenkov photons.

Simulations of electromagnetic showers in water were done in [88]. The longitudinal energy deposition could be parametrized with a gamma distribution:

$$\frac{dE}{dt} = E_0 b \frac{(tb)^{a-1} \exp(-tb)}{\Gamma(a)}, \qquad a = 2.03 + 0.604 \ln(E_0/GeV), \qquad b = 0.633. \tag{3.14}$$

Here, Γ is the gamma function, E_0 is the cascade energy and t is the length in units of the radiation length. The gamma distribution has its maximum at $t_{max} = (a-1)/b$. With the radiation length and the density of ice ($\rho_{\text{ice}} = 0.92\,\text{gcm}^{-3}$) a 100 TeV cascade will have its maximum at about 5 m.

For very high-energetic cascades the Landau-Pomeranchuck-Midgal (LPM) effect has to be

taken into account. Above PeV energies the cross-sections for pair production and bremsstrahlung are suppressed because of interference between amplitudes from different scattering centers. The cross-section suppression effectively elongates electromagnetic showers which can exceed lengths of 100 m above 10^{20} eV [89].

The transverse spread of the shower is given in units of the Molière radius

$$R_M \approx 21 \text{ MeV} \cdot X_0/E_c. \tag{3.15}$$

About 99% of the cascade energy is deposited in a cylinder with a radius of about $3.5R_M$ [25]. For ice this means a spread of about 35 cm.

In the cascade the Cherenkov light is emitted by the ensemble of electrons and positrons with decreasing energies and different directions. Hence, the angular emission profile of the whole cascade is different from a single relativistic particle, where the Cherenkov photons are emitted into a very narrow cone with angle θ_C (see Eq. 3.6). From simulations of electromagnetic cascades the angular emission profile has been derived [88, 90]. There is still a strong emission with angles close to θ_C but it shows emission into other directions, too.

To summarize, the electromagnetic cascades generated by electrons and photons in the energy interval of interest here (TeV to PeV energies) emit Cherenkov light in a volume of few meters length. This light has an angular distribution that peaks at the Cherenkov angle θ_C relative to the incident particle. The number of emitted photons scales nearly linearly with the energy of the primary particle.

3.2.3 Hadronic Particle Showers

Cascades emerging from hadronic interactions are different from electromagnetic showers. The hadrons in these particle showers either decay or interact again with nucleons. Like for electromagnetic showers the longitudinal development stills scales logarithmically with energy. But the characteristic nuclear interaction length $\lambda_\text{I} = 83.3\,\text{gcm}^{-2}$ is larger than the corresponding radiation length X_0 of electromagnetic showers [25]. Moreover, the development of hadronic cascades is not as regular as for electromagnetic showers. One reason is the electromagnetic component that every hadronic shower has: every generated neutral pion decays practically instantly into two photons which then induce an electromagnetic cascade. The particles in this component do not further contribute to the development of the hadronic shower. The other reason are muons created in decays of hadrons which may propagate much further than other particles in the shower. Hence, the development of hadronic showers fluctuates depending on the stage of shower development at which neutral pions and muons are created [88].

The Cherenkov light yield of hadronic showers is also lower than for electromagnetic cascades

for several reasons. Neutral particles created in the shower (e.g. neutrons) do not emit Cherenkov photons. Also the energy that goes into the binding energy of created hadrons is not available for the further creation of charged particles that would emit Cherenkov light. And because Cherenkov radiation is emitted only above a threshold velocity (see Eq. 3.6) the energy threshold of the heavier hadrons is higher than for electrons and positrons. The relative Cherenkov light yield of electromagnetic and hadronic cascades has been studied in simulations. Parametrizations for the mean light yield and its fluctuation due to the irregular nature of hadronic cascades have been derived in [91].

3.2.4 Muons

Muons are created abundantly in air showers but occur also in charged-current muon neutrino interactions and hadronic cascades. At relativistic speeds they emit Cherenkov light. The main processes through which muons lose energy are ionization, radiative processes like bremsstrahlung radiation, photonuclear interactions and electron-positron pair productions. At TeV energies muons can travel several kilometers in ice before they are stopped or decay. In simulations about 99.9% of the muons with an energy of 2 TeV (1 PeV) were able to traverse 5 km (30 km) of ice [92].

While the energy loss trough ionization is a continuous process, the radiative losses which are dominant above TeV energies are of stochastic nature [25]. With comparatively low cross-sections these losses occur only sporadically along the muon track. The energies transferred to secondaries fluctuate strongly and range up to substantial parts of the muon's total energy. In this case they are referred to as catastrophic energy losses. The high-energy secondaries induce electromagnetic and, in the case of photonuclear interactions, hadronic particle showers.

In transparent media the continuous emission of Cherenkov light along the muon track with its characteristic emission profile provides a clear signature. But the overlaid Cherenkov emission of the particle showers induced by catastrophic energy losses can alter this signature considerably. Studies of the total Cherenkov light output of muons where done in [88].

3.3 IceCube Detector

The Cherenkov radiation of charged secondary particles emerging from a neutrino interaction provides a viable detection principle to search for astrophysical neutrinos. But the small anticipated astrophysical neutrino flux and the extremely low interaction probability demand for detectors which instrument very large volumes of an optically transparent material with optical sensors. First size estimates for such a detector started at a few kilotons in 1960 and increased

over the years to gigatons and more [6]. Man-made caverns of this size are not economically feasible. Hence, the idea of Markov [93], to use natural volumes of water or ice, is the basis of currently operated detectors in lake Baikal [4], the Mediterranean sea [5] and the Antarctic ice sheet.

The IceCube Neutrino Observatory [7] is located at the South Pole and is the first kilometer-scale Cherenkov neutrino telescope. An optical sensor array is deployed deep into the Antarctic ice sheet. The IceCube array is accompanied by the IceTop surface air shower experiment.

The optical sensors, called Digital Optical Modules (DOMs) [94], are sensitive to Cherenkov photons between 350 nm and 650 nm. The DOMs are deployed between depths of 1450 m and 2450 m and are attached to strings that are formed by the readout cables. Each string has 60 DOMs attached.

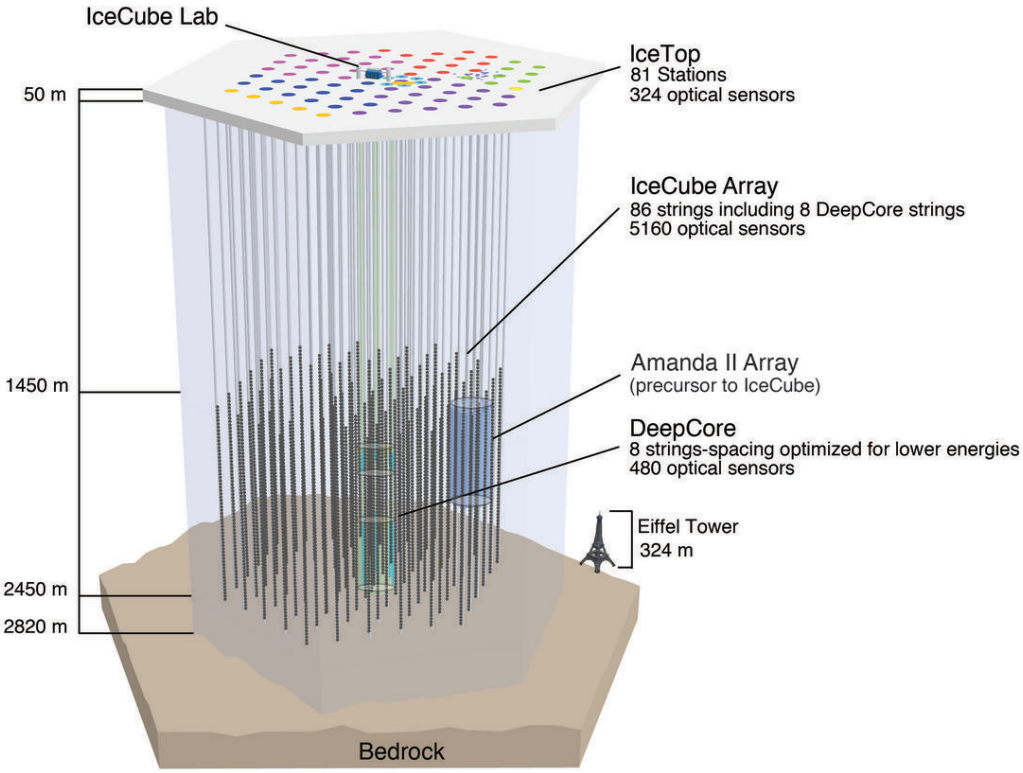

Figure 3.5: The IceCube Neutrino Observatory.

The IceCube strings were deployed during the seven Antarctic summer seasons from 2004/05 to 2010/11. The completed array comprises 86 strings. Their configuration are shown in Fig-

ure 3.5. Of the 86 strings 78 are arranged on a hexagonal grid with a horizontal spacing of approximately 125 m and a vertical spacing of the DOMs of approximately 17 m. The other 8 strings form a denser sub-array called DeepCore in the center of IceCube. The IceCube array also encloses its precursor AMANDA [95].

For this thesis IceCube data was used that was collected between April 2008 and May 2009 with a total of 367.1 days livetime. In this period 40 strings were deployed and operational. Before IceCube's completion in 2010, the IceCube-59, and IceCube-79 configurations took data with 59 and 79 deployed strings, respectively. The remainder of this section will describe the detector and readout electronics as it was operational for IceCube-40.

Each DOM consists of a 25 cm diameter photomultiplier tube (PMT) [96], made by Hamamatsu Photonics, a data acquisition system and a set of calibration LED light sources (flashers), all housed within a pressure sphere made of 13 mm thick borosilicate glass. The PMT's dynamic range is 200 photoelectrons per 15 ns and it is designed to accurately record the amplitudes and widths of the pulses with a timing resolution better than 5 ns. The PMTs peak quantum efficiency is approximately 25% and they are operated at a gain of 10^7 to resolve single photoelectrons.

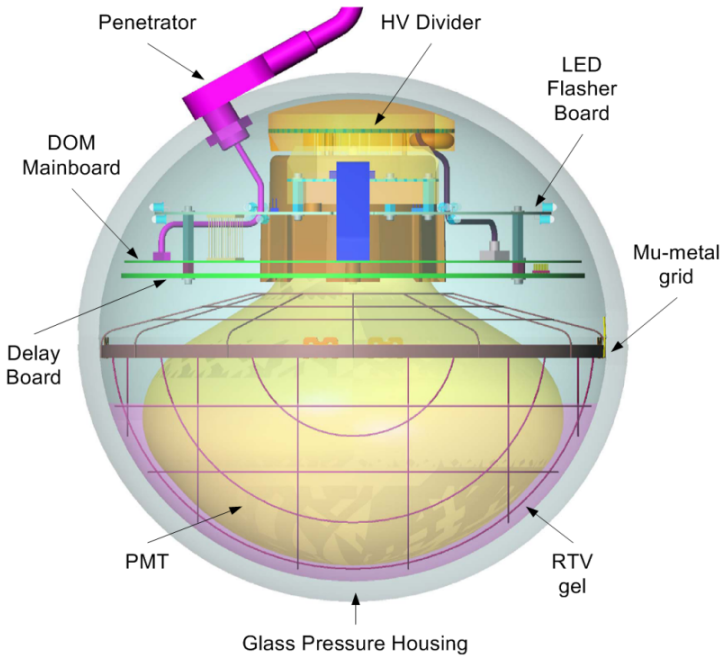

Figure 3.6: The IceCube Digital Optical Module (DOM).

The time-resolved PMT signal (waveform) is digitized in the DOM. For this purpose two

digitization devices are available on the DOM mainboard: two Analog Transient Waveform Digitizers (ATWD) and a fast Analog-to-Digital Converter (fADC). The ATWDs have three channels operated parallelly at different gains to provide a large dynamic range (a fourth channel is used only for calibration purposes). Due to scattering in the ice (see Section 3.4) the arrival times of photons emitted at the same point and time can vary by microseconds. The ATWDs provide a sampling rate of 300 Megasamples/s over a time window of 425 ns allowing them to record the earliest photons (i.e. those least affected by scattering in the ice) with high precision. The second digitizer, the fADC, has a coarser sampling of 40 Megasamples/s recording data over a longer time period for photons with larger delays of up to 6.4 µs.

In order to reduce data readout volume due to noise, a local coincidence criterion is required in IceCube-40. Only if a neighbouring DOM on the same string also detects light within the local coincidence time window of ±1000 ns, the PMT response is digitized, time-stamped, and transmitted to the surface for analysis. The surface data acquisition system combines the individual PMT responses and forms events when one of the several possible triggering criteria are fulfilled.

The main trigger requirement for IceCube-40 was the Simple Multiplicity Trigger, which required that eight DOMs were hit within a 5000 ns time window. The data rate for IceCube-40 from this trigger was approximately 1 kHz.

3.4 Light propagation in the glacial ice at the South Pole

Between its emission and its detection light travels up to several hundred meters trough the ice and is affected by scattering and absorption. The knowledge how the photon intensity and timing is altered by these effects is crucial in order to simulate the detector and interpret recorded data.

Photons are scattered on microscopic regions which have a different refractive index than the surrounding medium [97]. The experiment faces an abundance of such scattering centra with varying sizes in form of air bubbles and dust grains. The scattering can be parametrized by two parameters. First, the geometric mean free path λ_s, which gives the average distance between two scatters. Secondly, the distribution of the angle Θ between the photon direction before and after the deflection must be known. Using Mie theory this distribution has been derived in [98]. Light scattering in the Antarctic ice is strongly peaked forward with $\langle \cos\Theta \rangle = 0.94$ or $\langle \Theta \rangle = 20°$, respectively.

The parameters λ_s and $\langle \cos\Theta \rangle$ cannot be measured separately. With the dimensions of the IceCube detector photons get scattered several times before they are recorded in an optical module. As a consequence only the effective scattering length λ_e is measurable. It denotes

the length after which successive anisotropic scatters yield the same randomization as isotropic scattering:

$$\lambda_e = \lambda_s \sum_{i=0}^{n} \langle \cos\Theta \rangle^i \xrightarrow[n\to\infty]{} \frac{\lambda_s}{1 - \langle \cos\Theta \rangle}. \tag{3.16}$$

Absorption of visible and near ultraviolet photons happens due to electronic and molecular excitation processes [99]. These effects can be parametrized by a characteristic absorption length λ_a, after which the photon's survival probability drops to $1/e$.

Instead of the scattering and absorption lengths their reciprocal values, the effective scattering coefficient $b_e = \lambda_e^{-1}$ and absorption coefficient $a = \lambda_a^{-1}$ are often used.

Glacial ice is an optically inhomogeneous medium. Several of its properties which have an impact on the transmission of light, like temperature, pressure and concentrations of air bubbles or dust, change with depth. The ice sheet exhibits a layered structure which originates from climatological changes during the formation of the ice. The optical properties of the ice sheet are described in so-called ice models. These models stem from in-situ measurements of the detector response to pulsed artificial light sources, like deployed lasers or LED flashers inside the optical modules. Measurements were made with IceCube's predecessor AMANDA and were further refined by measurements performed with IceCube strings. The general procedure is to emit photons at one point in the detector and have them recorded by optical modules at different positions in the ice. Software for ray-tracing photons through a material as specified by the ice model is then used to simulate the light propagation. The parameters of the ice models are then adjusted until simulated and experimental data match.

Figure 3.7 summarizes the millennium ice model [98]. It shows the effective scattering coefficient and the absorption coefficient (absorptivity) as functions of the wavelength and the depth. The wavelength interval that needs to be considered here is limited in the ultraviolet by the transmission properties of the glass pressure housing. For higher wavelength it is limited by the dropping quantum efficiency of the PMT. The coefficients vary strongly with depth. Down to 1.3 km the ice is rich on air bubbles, which lead to strong scattering. By going deeper the pressure rises and the former gaseous molecules are trapped in the molecular lattice of the ice [100]. Such a solid air hydrate has a refractive index close to the surrounding ice, which reduces scattering. Between 1.4 km and 2.2 km pronounced peaks in both plots indicate the existence of dust layers that pervade the otherwise clear ice.

The millennium model was obtained by taking the data of emitter-receiver pairs and fitting them individually. The model was later improved to the AHA model. It corrects an intrinsic convolution effect in the analysis method used to derive the previous model. It also adds further information gathered from ice cores, which suggests that the ice below the big dust layer and between the other dust layers is much cleaner than expected. On the other hand scattering and

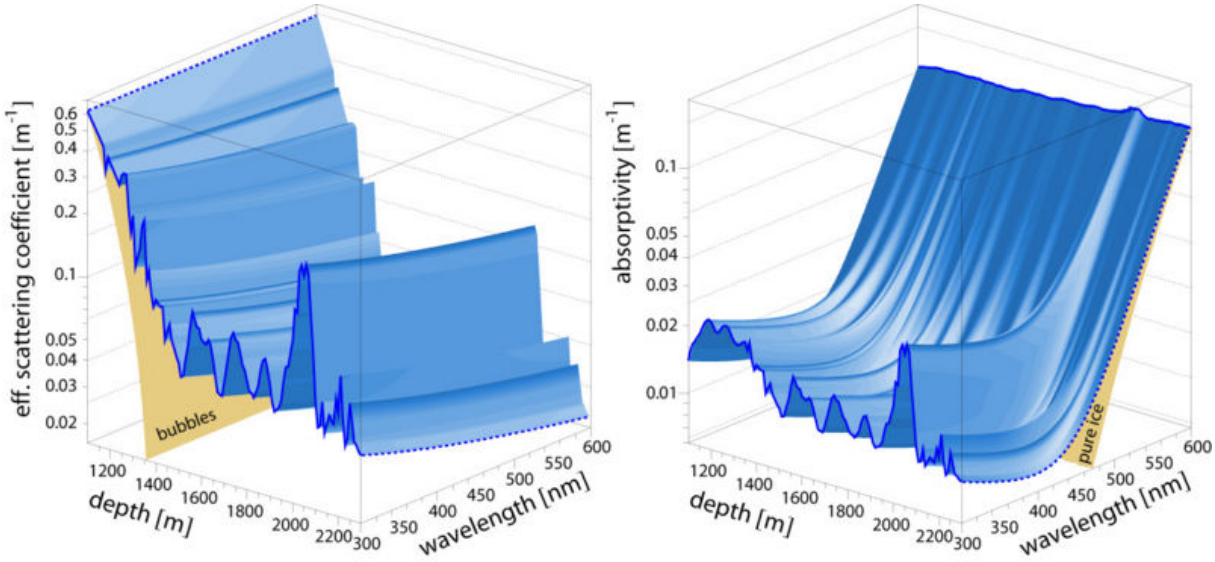

Figure 3.7: Absorption and scattering coefficients of the antarctic ice. Picture taken from [98].

absorption in the dust layers are assumed to be stronger. For most of this thesis the AHA model is used.

The AHA model was superseded by the South Pole Ice (SPICE) models [101]. These models stem from a global likelihood fit to describe simultaneously the data of all emitter-receiver pairs in a large dataset of flasher data taken with IceCube in 2008. An early result of this procedure, called SPICE1, is used in this thesis for the study of systematic uncertainties. A comparison of the absorption and scattering coefficients of the AHA and SPICE1 models is given in Fig.3.8. In the further evolution of the SPICE models adjustments of the distribution of scattering angles Θ were found necessary. Furthermore, indications for tilts in the ice layers and a azimuthal asymmetry of scattering directions were found. A full description of the current best understanding of the ice as well as a comparison to the AHA model can be found in [101].

3.5 Event Signatures

The detector response to a neutrino interaction results from an interplay of the physics described in the previous sections. Based on the signature of the neutrino interaction, which depends on the flavor of the incident neutrino and the type of the interaction (see Section 3.1), two main detection channels exist.

Searches in the muon channel look for charged-current muon neutrino interactions. These have

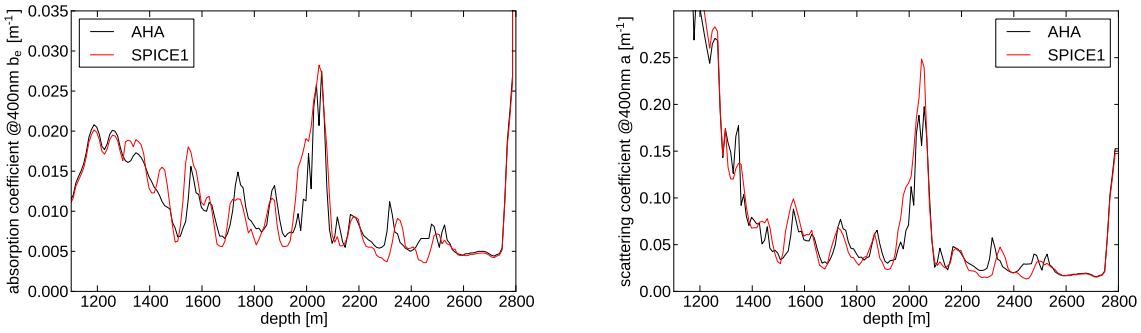

Figure 3.8: Comparison of the absorption and scattering coefficients of the *AHA* and *SPICE1* ice models.

a muon in the final state. The strongly peaked Cherenkov emission profile of the muon combined with light emission all along the muon track make the muon direction reconstructible with a resolution of about 1 degree [102]. This resolution is practically also achieved for the neutrino direction since the strong relativistic boost in the interactions yields a mean angle between the muon and the neutrino of about $0.7°/(E_\nu/\,\mathrm{TeV})^{0.7}$ [38]. Consequently the muon channel is particularly suited for neutrino astronomy, i.e. the search for the sources of astrophysical neutrinos.

The large muon range above TeV energies also allows to detect neutrino interactions outside the instrumented volume when the created muon afterwards passes through the detector. While this increases the effective volume in which neutrinos can be detected, it complicates the reconstruction of the neutrino energy. For tracks not starting inside the detector the energy transferred to the hadronic cascade at the interaction vertex as well as the energy lost by the muon on its way from the vertex to the detector is not accessible to measurements. Consequently only a lower limit on the neutrino energy can be obtained. Through-going muons do not deposit all of their energy inside the detector. Instead their energy has to be estimated from the energy losses along their track. While a nearly linear relationship exists between a muon's energy and its mean energy loss the stochastic nature of muon energy losses above $\sim 1\,\mathrm{TeV}$ yields large fluctuations in the particular amount of deposited energy (see Section 3.2.4). This inherently limits the achievable energy resolution for track-like events [103].

In the scope of this thesis the cascade channel comprises all other interaction scenarios. In the case of neutral-current interactions there is only the hadronic particle shower at the interaction vertex. In charged-current electron neutrino interactions the additional electromagnetic cascade emerges from the same vertex. To IceCube the two cascades are indistinguishable and appear

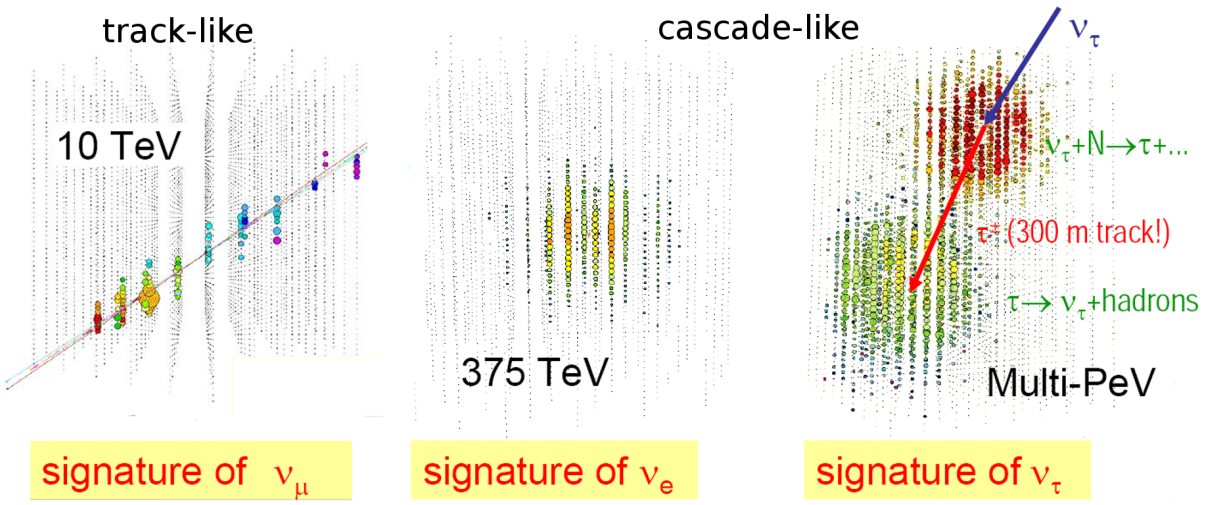

Figure 3.9: Event Signatures of ν_e, ν_μ and ν_τ interactions.

as a single point-like light source. Charged-current tau neutrino interactions can exhibit more complex signatures depending on the time dilated lifetime of the tau lepton and its decay products [61]. In those decay channels which result in a hadronic cascade, the resulting signature would be first a hadronic cascade at the neutrino vertex, then the track of the tau lepton followed by a second cascade, when the tau decays. Again these two cascades may not be distinguishable by IceCube if they are too close together. A sufficient separation is expected above 2 PeV where the tau lepton would travel about 100 m before decaying. This double bang signature is a unique feature of tau neutrinos. However, below PeV energies tau neutrinos are not distinguishable from other events in the cascade channel.

IceCube can detect neutrino-induced particle showers only when the neutrino interacts inside the detector or in its close proximity, so that the Cherenkov light can still reach the DOMs. This restriction in volume, where neutrino interactions can be detected, is balanced by two effects. First, since neutrino interactions of all flavors contribute to the cascade-channel more cascades than tracks are expected to start inside IceCube. Secondly, in comparison to muon tracks a particular advantage of the cascade interaction scenario is that all the energy transferred from the neutrino to a particle shower is dissipated close to the detector and hence is accessible to measurements. The nearly linear relation between deposited energy and Cherenkov light yield (see sections 3.2.2 and 3.2.3) allow for a better energy reconstruction mostly limited by the inherent fluctuations in the development of hadronic cascades [103].

The Cherenkov light emitted by muon tracks and particle showers traverses the optical inhomogeneous ice before being recorded by the DOMs. The resulting hit-patterns, i.e. the in-

formation when which DOM at a given position and time recorded how much light, are formed through the convolution of the original emission profile and the effects of the ice. Especially the strong scattering in the South Pole ice transforms the anisotropic emission of particle showers into nearly spherical hit-patterns. From the original anisotropy, and hence the direction of the incident neutrino, much information is lost.

Examples of typical hit patterns of different neutrino flavors are given in Figure 3.9.

In conclusion, the cascade channel is distinguished by good energy and a poor angular resolution. This makes cascades particularly suited for searches for diffuse astrophysical neutrinos in which the neutrino energy measurement is more important than pointing capabilities [9].

4 Simulation

Monte Carlo simulations of physics processes are used on several occasions during the interpretation of IceCube data. These simulation codes encapsulate the understanding how light propagates through the optical inhomogeneous detector as well as how the detector reacts to neutrino and atmospheric muon events. Event rate predictions in the experiment are derived from these simulations. For these predictions to be reliable large amounts of simulated datasets are needed. Hence, the production of simulated datasets was an essential part of this analysis. In the following the used tools and techniques are described.

4.1 Simulation of light propagation in glacial ice

Precise knowledge about the light propagation in glacial ice is crucial for the IceCube experiment. In order to interpret IceCube data or to simulate the detector it is necessary to predict for an emitter-receiver pair how much of the emitted light arrives at a given time at the receiver.

Here, an emitter-receiver pair comprises a light source (like a particle shower or a flasher) and a DOM as the receiver. The setup is illustrated in Figure 4.1. As outlined in Section 3.4 on their path between receiver and emitter photons are subject to scattering and absorption. Hence, not all emitted photons arrive at the DOM and due to scattering photons can reach the receiver also on non-straight paths.

On the receiver side the arriving photons hit photoelectrons out of the cathode of the photomultiplier. Hence, the observables of interest here are the mean total number of recorded photoelectrons $\langle n_{\mathrm{pe}} \rangle$ (amplitude) as well as the photon arrival times. For the arrival time t_a of a photon emitted at time t_0 at position $\vec{x}_0$ and propagating to a DOM at position $\vec{x}_1$ there exists a lower bound given by the time necessary to cover the distance at the vacuum speed of light:

$$t_a = t_0 + t_{geo} + t_d \geq t_0 + \frac{|\vec{x}_1 - \vec{x}_0|}{c}, \tag{4.1}$$

where $t_{geo} = |\vec{x}_1 - \vec{x}_0| / c$ is called the geometrical time and c denotes the vacuum speed of light. Substantial delay times t_d are caused by scattering. Depending on the distance between emitter and receiver the delay time can range up to microseconds.

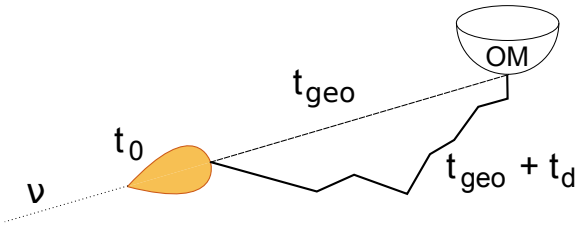

Figure 4.1: Photon propagation from the source to the DOM. Due to scattering photons can reach the DOM on non-straight paths and arrive therefore delayed with respect to the time necessary to cover the geometrical distance.

Ignoring the optical inhomogeneity of the detector for a moment, the delay time probability function dp/dt_d can be parametrized with a gamma distribution [104]. This parametrization, also called Pandel function, is useful in reconstructions where accuracy is less important than the speed of the calculation.

However, when the optical inhomogeneity of the medium is considered the actual recording of a DOM depends non-trivially on the particular geometric setup. Also, scattering and absorption are stochastic processes. Consequently, Monte Carlo methods are needed for detailed studies of the light propagation in ice. For this purpose the `Photonics` simulation program is used [105]. It can track an ensemble of photons through a horizontally layered medium, where the scattering and absorption coefficients vary with depth as described by the ice model. `Photonics` is able to simulate light sources with the angular emission profile typical for particle showers and muons. A cylindrical grid of cells is defined around the light source. Simulated photons are tracked as they pass through the cells. From these records the number of photons reaching a given cell and their arrival times are obtained. Using the quantum efficiency of the DOM the photon number is converted into the number of photoelectrons $\langle n_{\mathrm{pe}} \rangle$. This number as well as the delay time probability functions dp/dt_d are then tabulated.

Such a generated table describes light emission from a particular point in the detector. In order to cover all possible receiver-emitter geometries inside IceCube a set of these tables is needed, where the individual tables cover all possible emitter locations and orientations inside the detector. Symmetry assumptions reduce the number of tables necessary for a `Photonics` table set. Due to the azimuthal symmetry of the DOMs and the horizontally layered ice model, azimuthal and horizontal translational symmetry are assumed. Thereby, it is sufficient to define a grid of depths and zenith angles and simulate one table for each depth and orientation. Interpolation is required for receiver-emitter geometries that are not located on the grid.

The table sets generated by `Photonics` are used both in the simulation of IceCube events

and the reconstruction of events. However, the way how the tables are queried differs between simulation and reconstruction. In the simulation case the objective is to obtain for a given light source the number of photoelectrons and timing information at the position of the DOMs. For a single light source this information can be found inside a single table of the table set. In contrast during the reconstruction of an event, in which the number and arrival times of photoelectrons have been measured, the tables are queried with the objective to find the location and orientation of the light source that fits best to the measurement (see Section 5.2 for more details). To this end tables must be queried at different depths and zenith angles. As a consequence during reconstruction a table set covering all depths and zenith angles must be loaded into the computer's memory, whereas during the simulation only subsets are needed.

For the majority of the simulation used in this thesis a table set was used which incorporates the AHA ice model (see Section 3.4) with a 20 m spacing in depth and a 10° spacing in zenith angles. For the reconstruction of particle showers two different table sets are available. One is a subset of the simulation tables with a grid spacing of 40 m in depth and 20° in zenith angle. In the context of the angular reconstruction of particle showers the coarse zenith spacing and the multidimensional linear interpolation implemented in `Photonics` led to binning effects. In order to avoid these a parametrization of the `Photonics` tables through multidimensional spline fits was developed [106]. Such a parametrized table set incorporating the SPICE1 ice model has been used in this study.

4.2 Importance Sampling and Effective Livetime

The central use case of simulated IceCube events is to determine the distributions of event-characterizing variables for those events which pass a particular set of filter conditions (see Chapter 5). For example cosmic-ray induced air showers are simulated in order to estimate how many muons arrive at the detector and how the detector responds to them. Of interest are for example the distributions of reconstructed muon arrival directions or the reconstructed energy of these events. Knowing these distributions and how they change when cuts are applied is crucial when trying to distinguish the muons from the searched for neutrino flux.

To this end the sample of simulated events must be sizable to have enough events passing the filter conditions. Only then the statistical error of any quantity derived from the sample is sufficiently small. The need for a high background suppression results in tight cuts on a number of variables. In the parameter space spanned by these variables the events that are relevant at the highest cut levels populate a significantly smaller region than those events rejected by the filter.

Therefore, importance sampling is necessary to increase the efficiency of the Monte Carlo

simulation [107]. Instead of generating Monte Carlo events with frequencies according to the simulated process, more events are created in those regions of the parameter space, where events have a higher chance to survive the cuts.

So the generation distribution, from which events are sampled, differs from the target distribution which is actually meant to be simulated. In order to use such a biased sample to represent the process under study each event is provided with an event weight. Events have larger weights in sparsely sampled regions of the parameter space and smaller weights in oversampled regions.

The IceCube simulation uses a weighting scheme [108, 109] where every event carries an event weight w_i in units of Hz. The index i enumerates individual events. The rate of occurrence R of a particular ensemble of events (for example those falling into some bin of a histogram) is calculated as the sum of their weights $R = \sum w_i$. The calculation of the events weights depends on the particular simulation, but generally it includes the total number of generated events and the ratio of the target distribution to the generation distribution.

For a counting experiment with rate R that is run for the time T_{live} the relative statistical error of the event count N is:

$$\frac{\Delta N}{N} = \frac{\sqrt{RT_{\text{live}}}}{RT_{\text{live}}} = \frac{1}{\sqrt{RT_{\text{live}}}}. \tag{4.2}$$

For a weighted Monte Carlo simulation the statistical error is $\Delta N_w = \sqrt{\sum w_i^2 T^2}$ [110], where the time T is used here to transform the event rate into an event count. As a figure of merit for the statistical error of a sample of weighted events an effective livetime T_{eff} can be defined. It denotes the time necessary to run the real counting experiment to achieve the same relative error as provided by the weighted Monte Carlo sample:

$$\frac{\Delta N}{N} \stackrel{!}{=} \frac{\Delta N_w}{N_w} \;\rightarrow\; \frac{1}{\sqrt{RT_{\text{eff}}}} = \frac{\sqrt{\sum w_i^2 \cancel{T^2}}}{\sum w_i \cancel{T}} \tag{4.3}$$

$$T_{\text{eff}} = \frac{\left(\sum w_i\right)^2}{\sum w_i \sum w_i^2} = \frac{\sum w_i}{\sum w_i^2}. \tag{4.4}$$

Using T_{eff} is practical when the size of a simulated dataset is compared to the size of the experimental data recorded in one year.

In order to illustrate the effect of importance sampling on T_{eff} let's compare two simulations: one with importance sampling and one without. In both cases N events are simulated to represent a process occurring at rate R. From Eq. 4.4 one can see that when no importance sampling is used, i.e. when the weights are $w_i = R/N = const.$, the effective livetime $T_{\text{eff}} = N/R$ equals the time necessary to collect N events at rate R. This is exactly the livetime of the real

experiment T_{live}.

In the second case, when oversampling is used, the event weights are not constant. They reflect the difference between the generation distribution and the target distribution. By construction the events carrying large event weights are meant to be filtered out. After cuts, the remaining events have small weights $w_i < R/N$ and according to Eq. 4.4 the effective livetime becomes larger than T_{live}.

Calculating the effective livetime according to Eq. 4.4 is practical. It can be calculated for any ensemble of events just from the event weights. However, this approach has two problems when applied to atmospheric muon simulations. For these muons it is computationally difficult to obtain sufficiently sized event samples (see Section 4.4). As a consequence, tight cut conditions can remove all simulated events. In such a situation T_{eff} in Eq. 4.4 is simply not defined. The second problem is that the muon background comprises different components, which are induced by different primary cosmic-ray nuclei and occur with different frequencies. One has to make sure that enough events are simulated for each of these components - a requirement easy to miss by summing in the calculation of T_{eff} over all events of all components. If in such a case a tight cut condition removes all events of one component, that component's influence on the total statistical uncertainty is disguised. In such a situation it is better to compare the number of total generated events to the frequency of the process to be simulated.

4.3 Neutrino Simulation

For this analysis interactions of all flavors of neutrinos were simulated to model atmospheric and astrophysical neutrinos. The `NuGEN` software package maintained by the IceCube collaboration was used. It is based on the `ANIS` [111] neutrino generator, which produces neutrinos isotropically over the Earth's surface and propagates them to interact in or near the detector volume. Neutrino attenuation and ν_τ regeneration are accounted for using the Preliminary Reference Earth Model [84]. CTEQ5 structure functions [82] were used to model the deep-inelastic neutrino-nucleon scattering cross section.

Throughout this thesis the diffuse astrophysical neutrino flux is simulated isotropically, with a flavor ratio of $1:1:1$ and equal amounts of neutrinos and anti-neutrinos. If not stated otherwise an unbroken power-law spectrum with index of -2 and an all-flavor intensity of $3.6 \times 10^{-8}\,\text{GeVsr}^{-1}\text{s}^{-1}\text{cm}^{-2}$ is used.

Rate predictions for the atmospheric neutrinos are based on the HKKMS07 model [66] for conventional atmospheric neutrinos and the ERS model [65] for prompt atmospheric neutrinos (see Section 2.4). Extrapolations of the original calculations to higher energies provide rate predictions at the energy range relevant to this work. The steepening of the cosmic-ray spectrum

around a few PeV (the so-called "knee") causes a similar feature in the atmospheric neutrino spectrum which is not accounted for in the HKKMS07 model. A modification to the HKKMS07 model [16, 75] was applied to account for the knee. For comparisons the alternative Bartol model [74] was also used to estimate the conventional atmospheric neutrino flux. Compared to the modified HKKMS07 model it predicts a higher ν_e contribution (see Figure 2.4).

The propagation of muons and taus through the detector and their energy losses were simulated using the `MMC` program [92] and the cascade simulation inside the detector was handled by the `CMC` program [112]. Neutrino-induced cascades below a threshold of 1 TeV were simulated as point-like light sources, emitting an angular Cherenkov light profile typical of an electromagnetic shower [90]. Cascades of higher energies are split into segments along the direction of the shower development. Each cascade segment is then approximated by a point-like sub-shower with a light yield proportional to the light yield in the corresponding segment of the electromagnetic cascade. The elongation of electromagnetic cascades due to the suppression of bremsstrahlung and pair production cross sections above PeV energies (LPM effect, see Section 3.2.2) is accounted for. Hadronic cascades are simulated as electromagnetic cascades with a smaller light yield per deposited energy to account for the neutral shower components which do not generate Cherenkov light (see Section 3.2.3).

For each DOM the number of photoelectrons created by the muon tracks or cascades needs to be estimated. This is done by the `HitMaker` program which looks up each pair of light source and receiver in the `Photonics` tables. An additional contribution of noise-induced photoelectrons is simulated by the `NoiseGenerator` program.

After knowing the number of photoelectrons at the photomultiplier's cathode the `PMTSimulator` and `DOMSimulator` programs determine the response of each individual DOM and whether its readout condition is fulfilled. Afterwards it is checked if the triggered DOMs have fulfilled the trigger conditions necessary to read out the whole detector (see Section 3.3). If the simulated event fulfills the trigger condition it is kept and passed to further processing steps. The programs mentioned above are part of the IceSim simulation suite of which version V02-03-02RC has been used. A diagram illustrating the simulation chain is shown in Figure 4.2.

For the study presented here datasets for all three neutrino flavors were produced. The datasets are summarized in Table 4.1. Both E^{-1} and E^{-2} generation spectra have been used. The datasets are then reweighted to represent the target flux Φ_{target} which is either an atmospheric neutrino spectrum or the power-law spectrum of astrophysical neutrinos. To do this for each event i with energy E_i and zenith angle θ_i the weight

$$w_i = \Phi_{\text{target}}(E_i, \theta_i) \frac{w_i^{\text{one}} T_{\text{live}}}{N_{\text{evts}}} \tag{4.5}$$

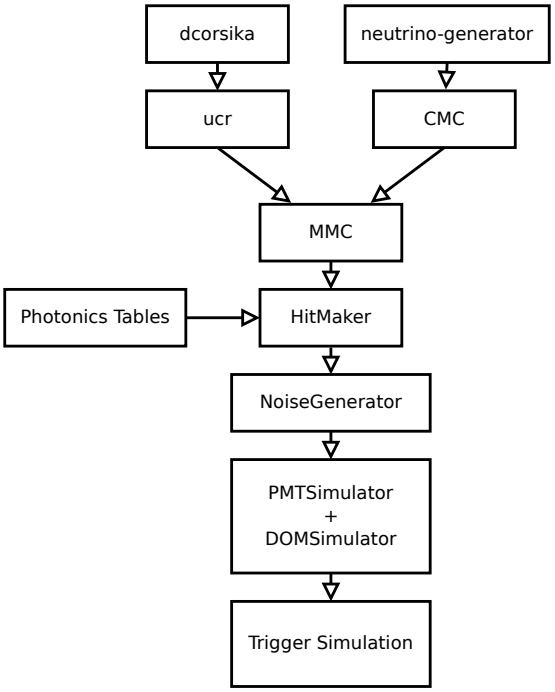

Figure 4.2: Overview of the simulation chain.

is calculated. Here N_{evts} denotes the total number of generated events and the livetime T_{live} transforms the weights from units of Hertz into an event count. The quantity w_i^{one} is the so-called OneWeight calculated by `NuGen` and accounts for two facts. Firstly, it includes the used generation spectrum. Secondly, because of the tiny neutrino cross sections `NuGen` increases the efficiency of the simulation by forcing each neutrino to interact. Afterwards it keeps track of the interaction probability through the event weight.

Datasets are produced with E^{-2} and E^{-1} generation spectra because they are typically shared between IceCube analyses. Depending on whether the analysis needs statistics at lower or at higher energies the softer or harder spectrum can be chosen. In the study presented here datasets with both spectra are combined. A threshold energy is defined. Below this energy only events from the E^{-2} datasets are used and above the threshold only events from the E^{-1} datasets are used. The threshold energy is ideally located near the point where the effective livetime of the combined sample is largest. For the datasets used in this study 100 TeV was found to

neutrino flavor	generation spectrum	energy range/ GeV	generated events
ν_e	E^{-2}	$10^1 - 10^{10}$	$600 \cdot 10^6$
	E^{-1}	$10^1 - 10^{10}$	$4 \cdot 10^6$
ν_μ	E^{-2}	$10^1 - 10^{10}$	$600 \cdot 10^6$
	E^{-1}	$10^1 - 10^{10}$	$5.9 \cdot 10^6$
ν_τ	E^{-1}	$10^1 - 10^{10}$	$15 \cdot 10^6$

Table 4.1: Simulated neutrino datasets.

be good choice. As discussed in the previous section the effective livetime has to be calculated per flavor and depends on the cut selection. For the final cut selections the combined muon neutrino dataset has the lowest effective livetime, because in a cascade search only the neutral current muon neutrino interactions are selected. Nevertheless, with an effective livetime of about 500 years the muon neutrino dataset is significantly larger than the experimental dataset. The effective livetimes of the other flavors are even higher, so the simulated neutrino datasets provide enough statistics for this study.

4.4 Simulation of atmospheric muon background

The contribution of atmospheric muon events is estimated from simulations done with a modified version [113,114] of the `CORSIKA` air shower simulation software [115]. The SIBYLL 2.1 hadronic interaction model is used [116].

As will be discussed in Chapter 5 the number of neutrinos expected to be found in this study is of the order of a few events per year. In order to measure these neutrinos, rare types of muon events occurring at the same rate need to be understood. To this end a large number of muon events have to be simulated. Providing a large background sample is computationally challenging, mostly because of the sheer number of air showers needed, but also due to the simulation of light propagation in the optically inhomogeneous ice. The lack of sufficiently sized background samples was the major obstacle in previous cascade searches done with IceCube-22 and IceCube-40 [14, 117].

Additionally, the chemical composition of the cosmic rays is important for an estimate of the muon background. Previous cascade searches have shown that protons are of prime importance [11]. Proton primaries produce lower multiplicities of muons with higher individual energies than heavier primaries. Compared to air showers induced by heavier elements, which typically lead to muon bundles reaching the detector, proton showers are more likely to generate single high-energy muons. If such a high-energy muon has a single catastrophic energy loss, the relative

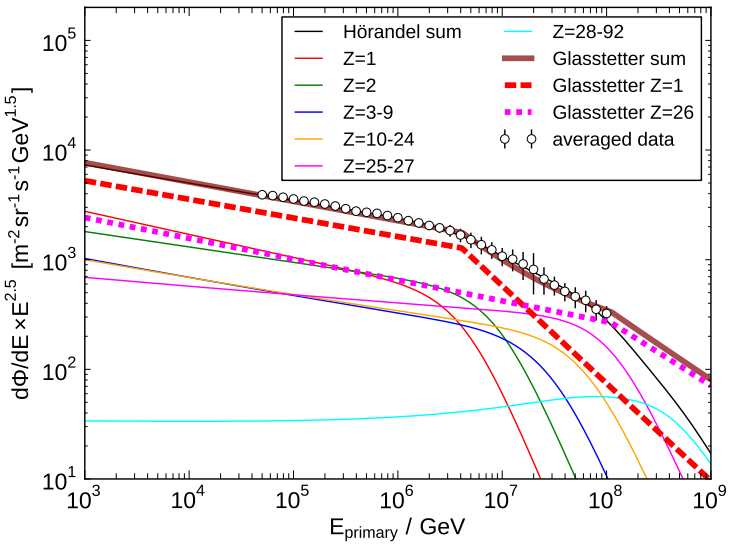

Figure 4.3: The cosmic-ray spectrum is modeled with two broken power laws for proton and iron (red and magenta dashed lines). Their parameters are taken from [119]. The Hörandel model and the data from which it has been derived is shown for comparison (both taken from [118]). The Hörandel model comprises components for each element from hydrogen up to iron, illustrated by solid lines.

light yield between shower and muon can make the resulting event signature look shower-like (see Section 3.2.4).

The cosmic-ray spectrum and composition are input parameters of the simulation. Besides the possibility to simulate power-law spectra of individual elements the modified `CORSIKA` version used here also implements Hörandel's poly-gonato model [118]. An illustration of the individual spectra in this model is shown in Figure 4.3. In each simulated event a nucleus between hydrogen and iron is chosen, its energy is sampled from the corresponding spectrum and the induced air shower is traced. Muons with enough energy to reach the IceCube array are selected. The `UCR` program adapts the output of `CORSIKA` and feeds it into the same simulation chain as described for the neutrino simulation (see Figure 4.2).

When using the poly-gonato model the generation and target spectra are identical. Hence, all events carry the same event weights and the datasets are called unweighted datasets. In order to increase the statistics at higher energies a harder generation spectrum can be used by adjusting

sample	generation spectrum	elements (Z)	energy range	generated events
I	unweighted Hörandel	1,2,..,26	$600 - 10^{11}$ GeV	$4340 \cdot 10^9$
II	weighted Hörandel	1,2,..,26	$600 - 10^{11}$ GeV	$66 \cdot 10^9$
III	E^{-2}	1,26	$10^4 - 10^{11}$ GeV	$2.4 \cdot 10^9$
IV	E^{-2}	1	$2.5 \cdot 10^3 - 10^9$ GeV	$284 \cdot 10^9$
V	$E^{-2.8}$	1	$70 \cdot 10^3 - 2 \cdot 10^6$ GeV	$995 \cdot 10^9$
VI	2x unweighted Hörandel	1,2,..,26	$600 - 10^{11}$ GeV	$460 \cdot 10^9$
VII	2x weighted Hörandel	1,2,..,26	$600 - 10^{11}$ GeV	$23 \cdot 10^9$
VIII	3x unweighted Hörandel	1,2,..,26	$600 - 10^{11}$ GeV	$68 \cdot 10^9$

Table 4.2: Simulated single-, double- and triple-shower `CORSIKA` datasets.

the generation spectrum $\Phi_Z(E)$ of element Z:

$$\Phi_Z(E) \to \Phi_Z(E) \cdot E/E_0. \tag{4.6}$$

The oversampling at higher energies is accounted for by energy dependent event weights. Datasets created with a modified generation spectrum are called weighted datasets.

Due to the size of the detector it is not uncommon that during an event's readout-window muons from more than one air shower are detected. When the individual events occur at rate r then the probability of n events to occur in a time window Δt calculates to:

$$P(n, r\Delta t) = \frac{(r\Delta t)^n e^{-r\Delta t}}{n!}. \tag{4.7}$$

To simulate coincident events two or three single air-shower events from CORSIKA are combined. The remaining detector simulation is the same as for single shower events. However, another factor $w_i^{\text{dipl.}} = P(n, r\Delta t)$, the so-called Diplopia weight, is added to the event weighting scheme.

The IceCube collaboration concentrates its available computing resources and maintains a centralized Monte Carlo production scheme [120]. Atmospheric muon datasets are simulated and further processed to contain the reconstructions necessary for a variety of IceCube analyses. From this effort originates a large part of the `CORSIKA` datasets used in this study, namely the unweighted and weighted datasets I,II,VI,VII and VIII listed in Table 4.2. This table summarizes the available datasets. Furthermore, dataset III has been adopted. It was originally developed for neutrino searches at very high energies.

About 17 days worth of effective livetime in coincident muon events were available. Although this is not much it was sufficient for this study. Coincident events are highly unlikely to create a single cascade signature in the detector and as such they can be effectively suppressed (see

Section 5.3).

In contrast, single muons can mimic the single cascade signature. Hence, the size of the single muon datasets is more of a concern. For an energy interval $[E_1, E_2]$ the number of events N_{evts} expected from cosmic-ray flux $dN/dEdtd\Omega dA$ calculates to:

$$N_{\text{evts}} = T_{\text{live}} A_{\text{sum}} \Omega \int_{E_1}^{E_2} dE \frac{dN}{dEdtd\Omega dA}, \tag{4.8}$$

where $T_{\text{live}} = 1\,\text{year}$ and $A_{\text{sum}}\Omega$ denotes the integral over the solid angle and detector area. In the simulation a cylindrical volume of 800 m radius and 1600 m height is defined. It encloses the IceCube detector and muons are traced inside. This volume is used for the $A_{\text{sum}}\Omega$ calculation. Figure 4.4 illustrates the number of generated proton and iron events in comparison to the number of corresponding air showers expected in one year according to the Hörandel model. Since the generation spectrum is harder than the cosmic-ray spectrum there exists a threshold energy above which more events were simulated than are expected to occur during the livetime of the experiment. Below the threshold the chance increases that rare event classes are underrepresented or even missing in the sample.

The comparison in Figure 4.4 is plotted as a function of the primary nuclei's energy. The combined samples from the centralized production (I,II and III) reach one year of livetime according to the Hörandel model at about 2 PeV. From the experimenter's perspective the more relevant threshold is defined in energy per nucleon E/A. This quantity relates to the muon energy which is measurable at the ground. At energies which by far exceed the nuclear binding energy the interaction between a heavy cosmic-ray ion and an air molecule can be described as if the nucleons would each have energy E/A and would interact individually. For iron primaries the corresponding threshold is $\text{E/A} \geq 35\,\text{TeV}$. The threshold increases for lighter elements. Hence, the problem of limited statistics at lower energies affects foremostly lighter primaries. As mentioned above these are of particular importance.

In order to improve the statistics of light primaries at lower energies two steps were necessary. First, the Hörandel model was replaced with a simplified cosmic-ray composition model which nevertheless reflects the qualitative differences between light and heavy elements. This two-component model considers only the two extrema of cosmic-ray composition and comprises two broken power laws:

$$\frac{dN}{dEdtdAd\Omega} = \Phi_0 \cdot \begin{cases} (E/\,\text{GeV})^{\gamma_1} & E < E_{\text{knee}} \\ (E/\,\text{GeV})^{\gamma_2} \cdot (E_{\text{knee}}/\text{GeV}\,)^{\gamma_1-\gamma_2} & E \geq E_{\text{knee}}, \end{cases} \tag{4.9}$$

one for the proton and one for the iron spectrum, respectively. It is based on air shower measure-

	$\Phi_0 / \left(\mathrm{m}^2\,\mathrm{sr}\,\mathrm{s}\,\mathrm{GeV}\right)^{-1}$	γ_1	γ_2	$E_{\mathrm{knee}} / \mathrm{GeV}$
proton	$17 \cdot 10^3$	-2.67	-3.39	$4.1 \cdot 10^6$
iron	$9 \cdot 10^3$	-2.69	-3.10	$1.1 \cdot 10^8$

Table 4.3: Parameters of the Glasstetter cosmic-ray model.

ments by Glasstetter et al. [119]. The model parameter are given in Table 4.3 and a comparison to the Hörandel model is shown in Figure 4.3. The flux normalization was chosen to resemble the all-particle flux predicted by the Hörandel model. The mean logarithmic mass of the all-particle spectrum formed by the sum of the two power laws is compatible with measurements of this quantity by air shower experiments [118].

Secondly, according to this simplified cosmic-ray model the statistics of iron primaries are sufficient above $\mathrm{E/A} \geq 50\,\mathrm{TeV}$. In order to lower the corresponding threshold also for protons, additional datasets of proton-induced air showers were produced. To this end the simulation and processing pipeline employed by the IceCube collaboration has been adapted. It was stripped down to only those parts relevant for this analysis. Furthermore, the number of events to be generated in one batch has been optimized for the highest throughput on the DESY computing cluster, which at that time comprised 928 CPU cores. This cluster is shared between multiple users. Therefore, in the beginning it was uncertain what throughput would be achievable and hence how far the proton energy threshold could be lowered in the available time. The production started with dataset IV which had an E^{-2} generation spectrum over the energy range of $2.5 \cdot 10^3 - 10^9\,\mathrm{GeV}$. With the experience from this run the production was then changed for dataset V which had an $E^{-2.8}$ generation-spectrum over the energy range of $70 \cdot 10^3 - 2 \cdot 10^6\,\mathrm{GeV}$. Over a time span of four month on average 52% of the spent computing time, corresponding to 158 CPU-core years, was related to simulating or further processing datasets IV and V.

This effort lowered the energy threshold for protons down to $\mathrm{E/A} \geq 90\,\mathrm{TeV}$ (see Figure 4.4). Below this threshold the statistics drop rather quickly and these low energetic events are underrepresented in the event sample. In order to assess the risk of underestimating the background the frequency of muons exhibiting prominent catastrophic energy losses was studied. For this purpose a sample of proton-induced air shower events has been branched off the simulation chain just before any detector and selection effects would be simulated (see Figure 4.2). The muons in these events have been propagated through the detector and energy losses along the track have been simulated by `MMC`. The events were weighted to represent the cosmic-ray flux according to the Glasstetter model. An upper bound for the primary energy E_{primary} has been defined and events below this energy were selected. For these events the individual energy losses E_{cascade}

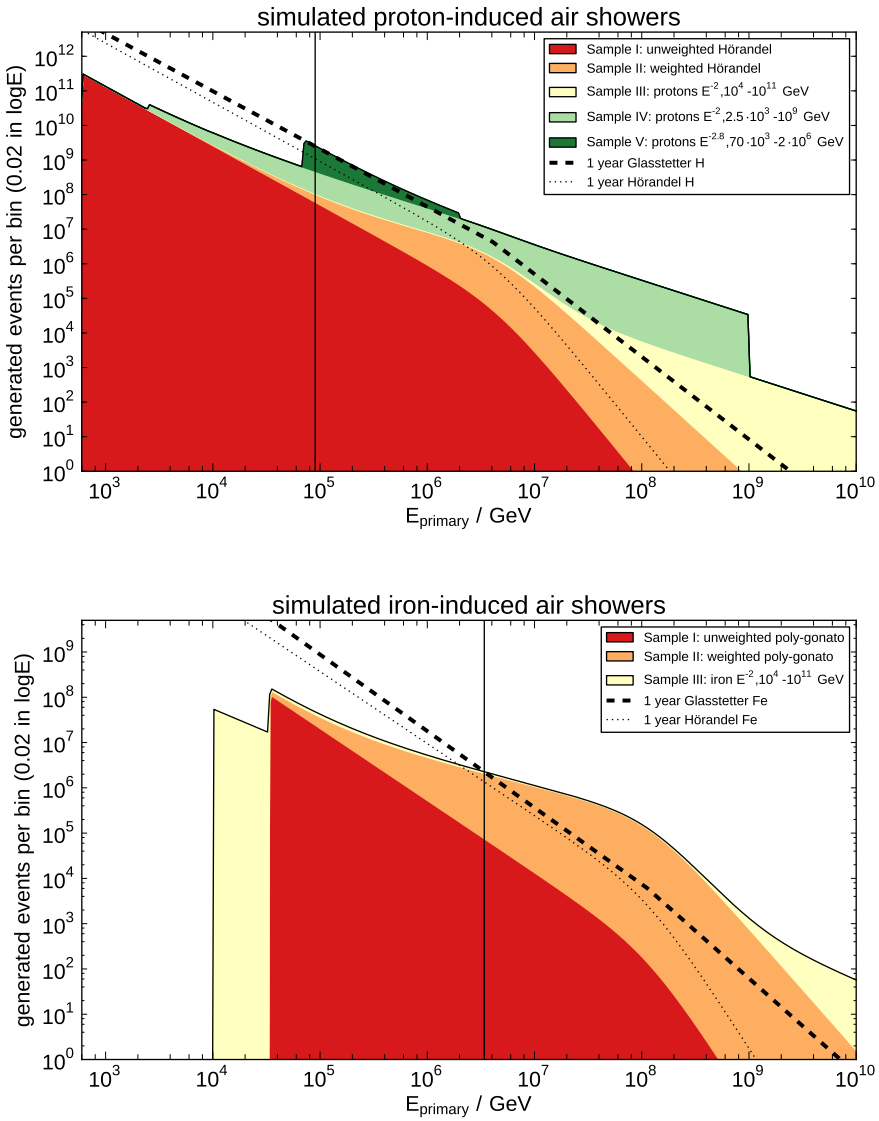

Figure 4.4: Number of simulated muon events from proton- and iron-induced single air showers. The shown stacked distributions illustrate the contribution of individual Monte Carlo datasets to the total available event sample. The dotted and dashed lines represent one year of livetime according to the Hörandel and Glasstetter models, respectively. The vertical solid lines indicate the threshold primary energy at which a year of livetime is reached. Transformed to energy per nucleon these thresholds correspond to $E/A \geq 90\,\mathrm{TeV}$ for proton and $E/A \geq 50\,\mathrm{TeV}$ for iron primaries, respectively.

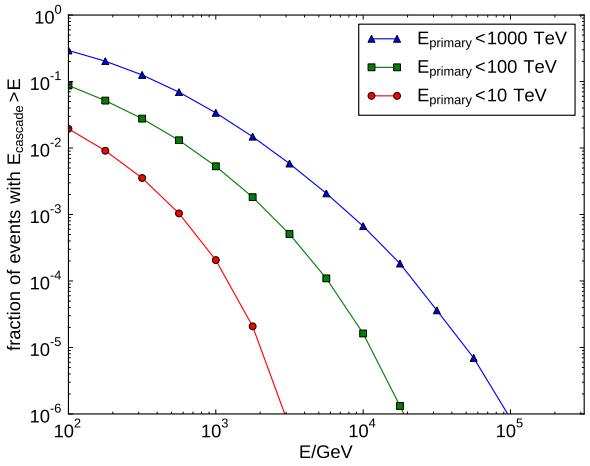

Figure 4.5: Proton air showers are simulated and weighted according to the Glasstetter spectrum illustrated in Figure 4.3. Bremsstrahlung cascades from muons originating in these showers are studied in order to assess the probability to obtain a bremsstrahlung cascade bright enough to pass event selection cuts from air showers below a given energy threshold. The plot shows the fraction of proton air showers with primary energy E_{primary} below 10, 100, 1000 TeV that exhibit catastrophic energy losses of E_{cascade} above a given energy.

along the track have been investigated and the fraction of events was determined, where E_{cascade} in a single energy loss exceeds a given threshold. The results are illustrated in Figure 4.5. Generally, these fractions decrease quickly with increasing energy thresholds. The fraction of air showers with a primary energy below 90 TeV which exhibit bremsstrahlung losses of 2 TeV (10 TeV) is only 1.8×10^{-3} (1.6×10^{-5}).

Finally, a combined dataset had to be created from the individual samples. Datasets I and II were simulated according to the Hörandel model containing air showers induced by all elements between hydrogen and iron. From these only the proton and iron events were used. They were combined with the proton and iron events from datasets III-V and events weights were calculated according to the scheme presented in [121].

Let the individual generation spectra of sample s for element Z be $\Phi_Z^{(s)}(E)$. With the number of generated events in each sample being $N_Z^{(s)}$ the total number of events is $N_{\text{total,Z}} = \sum_s N_Z^{(s)}$. From these the combined generation spectrum $\hat{\Phi}_Z(E)$ is formed:

$$\hat{\Phi}_Z(E) = \sum_s c_Z^{(s)} \Phi_Z^{(s)}(E) \qquad c_Z^{(s)} = \frac{N_Z^{(s)}}{N_{\text{total,Z}}}. \tag{4.10}$$

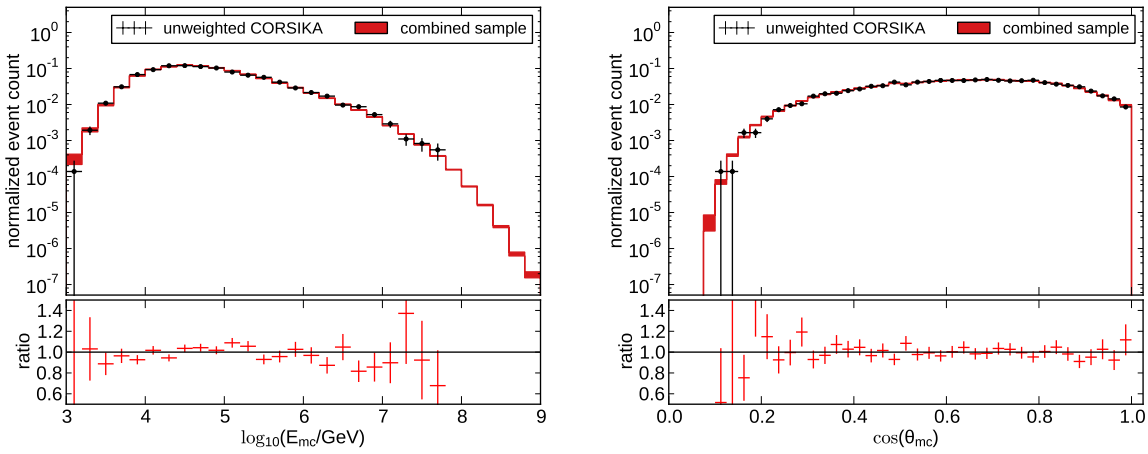

Figure 4.6: The distributions of the cosmic-ray primary energy and zenith angles are shown for the unweighted CORSIKA sample I and the combined event sample. The size of the error bars and error bands indicate the statistical error. Both distributions agree within statistical errors indicating that the weighting scheme works as expected.

The shape of the combined generation spectrum $\hat{\Phi}_Z(E)$ resembles the envelope of the stacked distributions in Figure 4.4. The weight for event i which was induced by primary Z with energy E_i is then:

$$w_i = \frac{w_i^{\text{dipl.}} \cdot A_{sum}\Omega}{N_{\text{total,Z}}} \cdot \frac{\Phi_{\text{target,Z}}(E_i)}{\hat{\Phi}_Z(E_i)}, \tag{4.11}$$

where $\Phi_{\text{target,Z}}(E)$ is the target flux to be represented by the sample. The diplopia weight $w_i^{\text{dipl.}}$ and the area sum $A_{sum}\Omega$ have been described above.

In order to check this weighting scheme the combined sample, with the weights from Eq. 4.11 applied, is compared to the unweighted CORSIKA sample I. The comparison is done for the primary energy and zenith distributions and is shown in Figure 4.6. The shown distributions differ from the cosmic-ray model since they contain detector and selection effects. For both variables the distribution of the combined sample resembles the distribution of the unweighted CORSIKA sample with much smaller statistical errors. No indications for problems caused by the mixing of the samples were found.

5 Analysis

This chapter describes the search for neutrino-induced particle showers in the dataset taken with IceCube-40. Two other searches were performed on the same dataset targeting energies $\gtrapprox 30\,\mathrm{TeV}$ in order to search for astrophysical neutrino-induced cascades. When they unblinded in 2011 the numbers of events found in both searches were consistent with the background expectation resulting in upper limits on the astrophysical neutrino flux [14, 15]. However, both analyses were challenged by the lack of simulated muon data during the development of the event selection, resulting in a high background contamination of their final samples.

The analysis presented here started as the low-energy counterpart to the two other searches with the objective to measure the atmospheric neutrino flux at $\gtrapprox 1\,\mathrm{TeV}$. The measurement of atmospheric neutrino-induced cascades is important as it forms the background for the astrophysical neutrino searches which target higher energies. Only at $\gtrapprox 30\,\mathrm{TeV}$ the harder astrophysical neutrino spectrum is expected to become distinguishable from the atmospheric neutrinos (see also Figure 2.4).

Both the atmospheric and the astrophysical neutrino flux are buried under the atmospheric muon background. The muon background is five orders of magnitude more abundant than the atmospheric neutrino flux. So for both the low- and high-energy searches techniques had to be developed, which reliably suppress the muon background while maintaining sensitivity for neutrinos. Because of the objective to detect atmospheric neutrinos the energy threshold of this analysis has been kept low. However, the event selection presented in the following has also sensitivity to astrophysical neutrinos. Therefore, measuring or constraining the astrophysical diffuse neutrino flux was also a goal of this analysis.

This chapter is organized as follows: after outlining the analysis method the best available cascade reconstruction algorithm will be presented. Afterwards techniques will be described which were found to be effective in characterizing particle shower and in discriminating them from background. Then, their combination to an event selection suitable to reach the aforementioned objectives will be explained. Finally, sources of systematic uncertainties and how they are accounted for will be discussed.

5.1 Analysis Outline

A small number of neutrino generated showers needs to be isolated from a large background of atmospheric muons. This is achieved by finding and applying a set of conditions on the reconstructed event properties that neutrino induced showers fulfill, but atmospheric muons do not. In practice this selection is implemented as a multi-step process. The first steps in the process are aimed at conservatively reducing the background, allowing the use of computationally intensive reconstruction algorithms, that can be applied to a reduced set of events only. Based on these more elaborate reconstructions further selection criteria are applied in subsequent steps.

The outcome of this sequence of steps are two event samples: one low-energy and one high-energy sample. In these event selections the background has been reduced to a degree that statements about the atmospheric and astrophysical neutrino fluxes become possible - either by directly measuring their intensities or by constraining their intensity in case that no neutrino-candidate events are found.

A simple cut-and-count approach is followed here. After applying the event selection a hypothesis test is conducted which compares the number of events passing the event selection to the number of events expected from background. A Bayesian approach is used to account for statistical and systematic uncertainties in passing rate predictions and to quantify deviations of the result from the background-only expectation (see Section 5.6). The established practice in particle physics searches for previously undetected phenomena is to require a deviation corresponding to five standard deviations (5σ) before rejecting the background-only hypothesis. This high benchmark before claiming a detection will be adopted here.

In order to reduce the effect of experimenter's bias during the development of the event selection a blind analysis is performed [122]. The experimental data was taken over the time span of 367.1 days between April 2008 and May 2009. Ten percent of this data, sampled uniformly over the year in order to contain any seasonal effects, are taken for developing the analysis. The data is used together with the simulation datasets to derive cuts and to check the accuracy of the Monte Carlo datasets. An overview of the used simulation datasets has been given in the Sections 4.3 and 4.4. The remaining 90% of the experimental data are kept blind until the cuts are finalized and are then used for the hypothesis test.

5.2 Reconstruction of cascade-like events

Cherenkov light, emitted by charged particles, traverses the optically inhomogeneous detector material and is then sampled by the three-dimensional IceCube array with nanosecond precision. Hence, the light's arrival times and amplitudes are the sole available information on any particle

interaction in the detector. Previous analyses relied on reconstruction algorithms that used only parts of this information, i.e. by considering only the integrated amplitude of all light reaching a DOM or by using only the arrival time of the first photon. A new algorithm `CREDO` [123] was developed. By using the waveform information `CREDO` is able to reconstruct not only the interaction vertex and the deposited energy but also the direction of the incident neutrino. `CREDO` is the first IceCube cascade reconstruction algorithm which is able to estimate the direction of the neutrino. The measurement process is described with a probabilistic model and a maximum likelihood estimator allows information on the vertex of the neutrino interaction, the neutrino direction and the deposited energy to be inferred.

`CREDO` considers the information on an event in the form of time intervals $(t, t + \Delta t)$ in which a DOM at position $\vec{x}$ recorded a given amount of charge n. Formally, the event is then described with the set $\{n_i(\vec{x}, t, \Delta t)\}$, where the index i runs over all such intervals. It should be noted, that this set also contains time intervals in which no charge has been recorded, since these time intervals also carry constraining information. The particle showers are modeled as point-like Cherenkov emitters, in the same way as they are described in simulation. A particle shower is then fully specified by 7 parameters $\alpha = (t_0, x_0, y_0, z_0, \theta, \phi, E)$: the time and position of the vertex, two angles for the direction of the neutrino and the deposited energy. The scattering and absorption of light in the Antarctic ice are depth dependent. The `Photonics` package is used to calculate the light propagation in the ice and to create tables with light arrival times and amplitudes as a function of the depth and the relative position between particle shower and DOM. In order to avoid binning effects the table values are interpolated by multidimensional spline fits prior to being used in the reconstruction (see Section 4.1).

The `Photonics` tables are used to calculate for each time interval i an estimate of the mean expected charge μ_i:

$$\mu_i = \hat{n}_i(\vec{x}, t, \Delta t, \alpha) + r_{noise}\Delta t. \tag{5.1}$$

In this sum $\hat{n}_i$ is the contribution due to the cascade α and $r_{noise}\Delta t$ is a continuous noise contribution. The expected charge from the cascade $\hat{n}_i$ in the time interval $(t, t+\Delta t)$ is calculated from the tabulated values of the mean total charge $\langle n_{\mathrm{pe}} \rangle$ and the delay time probability functions dp/dt_d:

$$\hat{n}_i = \langle n_{\mathrm{pe}} \rangle \int_{t_d}^{t_d+\Delta t} \frac{dp}{dt_d}(\tau) d\tau, \tag{5.2}$$

where $t_d = t - t_{\mathrm{geo}} - t_0$ is the delay time as it was introduced in Section 4.1.

In each time interval a counting experiment is performed, and the probability of a given

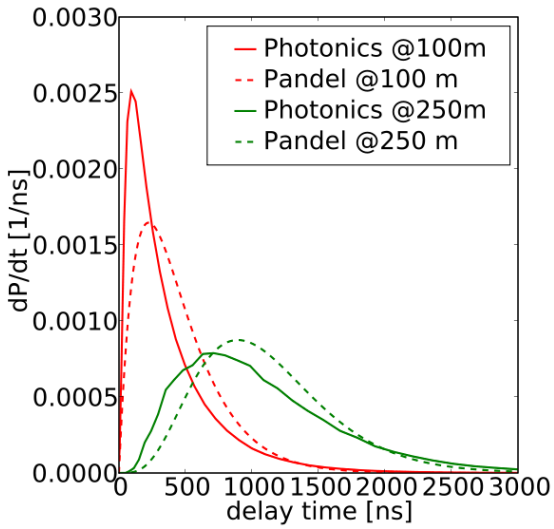

Figure 5.1: The distribution of arrival times of photons at a DOM is specified by the delay time probability function dp/dt_d. This plot shows the dp/dt_d for two cascades in 100 and 250 m distance to a DOM. Values obtained from the `Photonics` tables are shown as well as the analytical Pandel parametrization (see also Section 3.4 and Section 4.1).

measurement $\{n_i\}$ under the condition α can be calculated:

$$P(\{n_i\}|\alpha) = \prod_i \frac{\mu_i(\alpha)^{n_i}}{n_i!} \exp\left(-\mu_i(\alpha)\right). \tag{5.3}$$

From this probability one can construct a maximum likelihood estimator, yielding the parameters $\hat{\alpha}$ best supported by the measurement:

$$\hat{\alpha} = \underset{\alpha}{\operatorname{argmin}}\ \mathcal{L}(\alpha) \quad \text{where} \quad \mathcal{L}(\alpha) = -\log P(\{n_i\}|\alpha). \tag{5.4}$$

The search for the global maximum in the 7-dimensional likelihood space is performed by minimizing the negative logarithm of the likelihood using the SIMPLEX minimizer in the Minuit software package [124]. In order to avoid local minima the search is done iteratively, where in each step the minimizer starts at a different position in the parameter space. The iterative minimization and the many necessary table lookups for each time interval form a time-consuming procedure.

For IceCube-40 a modification to Eq. 5.2 had to be applied. As described in Section 3.3 the time-resolved PMT signal is digitized by two devices. The ATWD covers only the first 425 ns

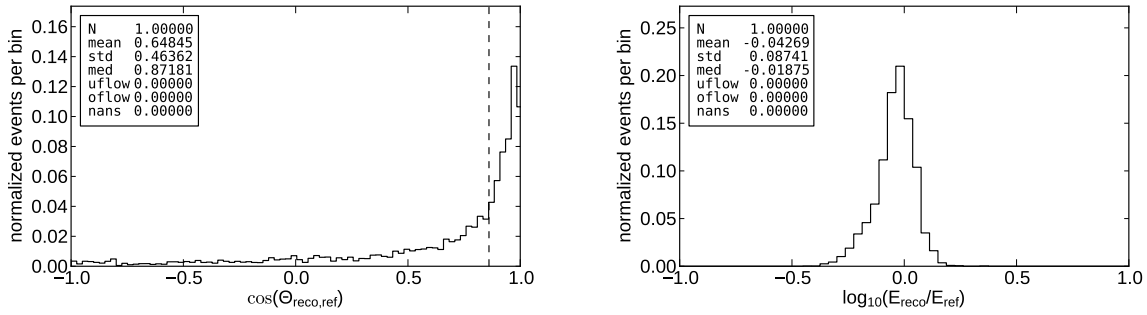

Figure 5.2: Reconstruction performance of CREDO on simulated electron neutrinos. The left plot shows the cosine of the angle between the reconstructed and the true direction. For half of the events the direction of the incident neutrino is reconstructed better than 30°. The right plot shows the logarithmic difference between the reconstructed and the visible energy. On simulated data the energy is reconstructed with a resolution of $\Delta(\log_{10}(E)) = 0.09$ or 23%. A comparison performed on experimental data with a different reconstruction method, which includes a better modelling of the light propagation in ice, leads to the more conservative estimate for the energy resolution of 40%.

with a high sampling rate. In contrast, the fADC covers 6.4 µs, but only with a reduced sampling rate. Problems were found in the software used to simulate and reconstruct the behavior of the fADC. This led to the decision to restrict this analysis only to data digitized by the ATWD. This restriction does not affect the earliest photons at a DOM which are the least affected by scattering and therefore provide crucial information on the event. But it reduced significantly the time-window in which each DOM records light and thus the total charge that can be accumulated. Figure 5.1 illustrates the delay time probability function dp/dt_d for two DOMs in 100 m and 250 m distance to a particle shower. In the latter case most of the scattered photons arrive outside the 425 ns of the ATWD. As discussed in Section 3.2.2 the energy deposited by the neutrino relates to the total number of photons in the event. Hence, in order to avoid biasing the energy estimator the expected mean total charge $\langle n_{\mathrm{pe}} \rangle$ in the event must be modified to account for the reduced time window:

$$\langle n_{\mathrm{pe}} \rangle \rightarrow \langle n_{\mathrm{pe}} \rangle \cdot f_{\mathrm{phot}} \qquad f_{\mathrm{phot}} = \int_0^{425\,\mathrm{ns}} \frac{dp}{dt_d}(\tau) d\tau. \tag{5.5}$$

The integral in Eq. 5.5 must be computed for every individual time interval and every hypothetical cascade parameter α that the minimizer probes during the reconstruction. In order to avoid this computational effort a parametrization was derived. As illustrated in Figure 5.1

the fraction of photons arriving during the first 425 ns decreases with distance $|\vec{x} - \vec{x}_0|$ between the cascade and the DOM. In studies with simulation data the following phenomenological parametrization was found to provide suitable results:

$$f_{\text{phot}} = \frac{2}{3} \exp\left(-\frac{1}{2}\left(\frac{|\vec{x} - \vec{x}_0|}{120\,\text{m}}\right)^2\right). \tag{5.6}$$

For further information on the modifications applied to the `Photonics` predictions see [123].

The reconstruction algorithm described here finds the position of the particle shower with a resolution of 15 m horizontally and, due to the smaller DOM spacing, 5 m vertically. The energy resolution[1] obtained from reconstruction performance studies on simulated data is about 23% (see Figure 5.2). A cross-check was done with another reconstruction algorithm [125] on experimental data. This algorithm does not consider the IceCube-40 specific corrections but it includes a better modelling of light propagation in the ice. Differences up to 40% have been observed. Hence, this more conservative number is adopted for the energy resolution. The angular resolution, defined as the median angle between the reconstructed and the true direction of the neutrino, is about 30°. Other variants of the likelihood reconstruction described here have been developed and used in more recent analyses. By incorporating improvements in the understanding of the detector response and a better modeling of the ice they provide better resolutions and determine IceCube's performance on cascades today [103].

5.3 Background Rejection Methods

Several different techniques and their corresponding cut variables were found to be useful in separating neutrino-induced particle showers from atmospheric muon events. Conceptually these techniques can be grouped into four classes. There are those which are based on reconstructed event parameters and those which reject events outside the instrumented volume. The third group is concerned with the shape of the recorded hit patterns whereas the last group considers the time evolution and charge distribution in the event. The methods will be described in the following.

[1] Only part of the neutrino energy is measurable in IceCube. The energy carried away by the neutrino in neutral-current interactions is not accessible. Also for equal deposited energy an electromagnetic cascade produces more Cherenkov light than a hadronic cascade (see Sections 3.2.2 and 3.2.3). This leads to the definition of the visible or reference energy, which denotes the energy of an electromagnetic cascade that has the same light yield as the neutrino interaction under study. This is the benchmark a reconstruction algorithm should find.

5.3.1 Reconstruction Based Cut Variables

Four different likelihood reconstruction routines are used in the searches described here. The routines differ in runtime, precision, initial assumptions and in the number of neutrino parameters that they infer from the event. Three of the reconstruction routines return parameters with the hypothesis that the event is a particle-shower. The fourth routine assumes that the event contains a muon track.

At earlier cut levels the `cscd_llh` likelihood reconstruction [13] is used. It does not account for the optical inhomogeneities of the ice but provides a quick estimate for the vertex and a quality parameter $\mathrm{rlogL}_{\mathrm{cscd}}$ that describes how well the event fits to the cascade hypothesis.

Using the vertex estimate from `cscd_llh` another estimate for the deposited energy, E_{ACER}, is provided by the `AtmCscdEnergyReco` algorithm [117]. It is quick to compute and considers the optical inhomogeneities of the ice.

At later levels the `CREDO` algorithm described in Section 5.2 provides the best estimates for the reconstructed vertex $\vec{x}^{(n)}_{\mathrm{CREDO}}$, deposited energy $E^{(n)}_{\mathrm{CREDO}}$ and zenith angle $\Theta^{(n)}_{\mathrm{CREDO}}$. The superscript (n) distinguishes, where necessary, applications of the `CREDO` algorithm with differing numbers of iterations.

All events are also reconstructed with another likelihood reconstruction [126] which assumes that the event contains a muon track. This routine gives a zenith angle estimate Θ_{track} and provides a quality of fit parameter $\mathrm{rlogL}_{\mathrm{track}}$ for the track hypothesis. The zenith angle estimator correctly identifies much of the muon background as downgoing. Particle showers are preferentially interpreted as either horizontally or diagonally passing tracks which allows for some signal-background separation.

5.3.2 Containment Cuts and Vetoing

A particularly problematic background are muon events which pass close to the edges of the detector producing a light distribution which is similar to that produced by cascades. To counter this background various containment conditions are placed on the position of the reconstructed vertex, the first-hit DOM and the DOM with the highest collected charge.

Events are excluded if the first hit DOM or the DOM with the highest collected charge is located in the outermost vertical layer (see Figure 5.3). Events are also vetoed if the depth of the first hit DOM $z_{1^{\mathrm{st}}}$ falls in the top or bottom 50 m of the detector.

The reconstructed vertex $\vec{x}_{\mathrm{CREDO}}$ is required to lie inside the instrumented volume. Vertices in the top or bottom 50 m of the detector are excluded as well as vertices whose xy-position falls inside the area illustrated in Figure 5.3.

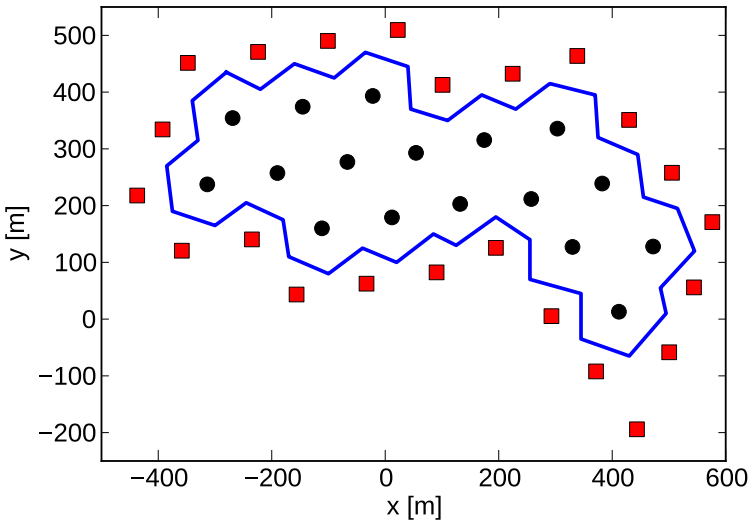

Figure 5.3: IceCube-40 string layout and veto regions as viewed from above. The outer layer of strings denoted by red squares is used to veto incident muons. Reconstructed vertices are required to be located inside the area surround by the blue line.

5.3.3 Topological Characteristics

The hit patterns of particle showers in IceCube are approximately spherical while the muon-track hit patterns are more elongated. A number of different quantities can be calculated to characterize the different topology of cascade and muon events and used to preferentially select cascades.

For example, a quantity analogous to the tensor of inertia of a rigid body, is calculated for each event. The collected charge on each DOM takes the role of the rigid body's mass distribution (see Figure 5.4). The ratio of the smallest eigenvalue to the sum of all of the eigenvalues, $\lambda = \lambda_{\text{min}} / \sum \lambda_i$, tends to $\frac{1}{3}$ for spherical events while muon tracks typically have smaller eigenvalue ratios [126].

Another way to select spherical events is to construct a spherical volume surrounding the reconstructed event vertex $\vec{x}_{\text{CREDO}}$ and consider the proportion of hit DOMs, versus the total number of DOMS, in this sphere (see Figure 5.5). The radius of the sphere considered is chosen to scale with the average distance between reconstructed vertex $\vec{x}_{\text{CREDO}}$ and position of the hit DOMs – a robust estimate for the overall size of the hit pattern. The fill-ratio f denotes the fraction of DOMs, falling within the sphere, on which light is recorded [11]. Hence, fill-ratios close to 100% are obtained for spherical hit patterns, while muon events yield lower values. The

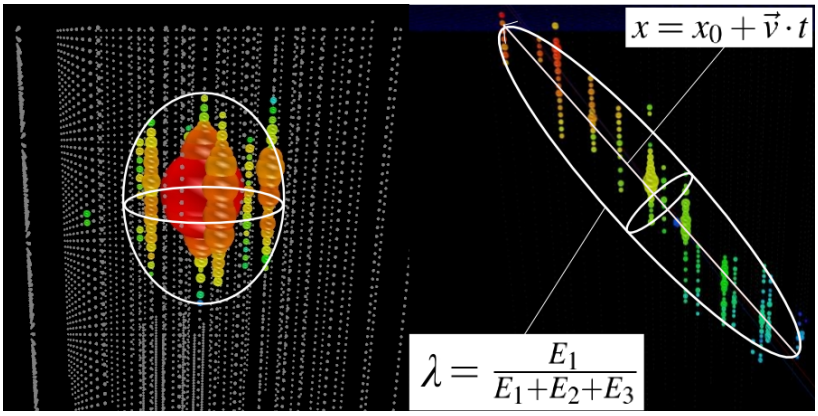

Figure 5.4: Event displays of a simulated particle shower (left) and a muon track (right). Each DOM is represented by a sphere. Their sizes denote the recorded charge. The timing of the event is illustrated by colors ranging from red (early hits) to blue (late hits). For the tensor of inertia eigenvalue ratio λ the hit pattern is interpreted as a rigid body where the recorded charge represents mass. For elongated hit patterns like muon tracks there is one distinguished axis with corresponding low eigenvalue, resulting in a low ratio λ. For spherical events no such axis exists and λ tends to 1/3.

fill-ratio is especially efficient to suppress coincident muon events – two or more muons from different air showers that cross the IceCube detector within microseconds of each other. When coincident muons create disjunct hit patterns in different parts of the detector the enclosing sphere has to be large and the fill-ratio tends to small values.

A second quantity, the difference Δf of two fill-ratios with different radii, is also used. This quantity provides further separation power due to the fill-ratio's dependency on the chosen radius. The dependency is slightly different for the differently shaped hit patterns of cascades and tracks.

5.3.4 Time Evolution and Charge Distribution Variables

Below PeV energies the Cherenkov light of particle showers originates within a few meters of the interaction vertex and then propagates through the detector with the speed of light in ice c_{ice}. In contrast, muon tracks traverse the detector with velocities close to the speed of light in vacuum c and emit Cherenkov photons continuously along their track. Several approaches exploit this difference to separate cascade and track events.

A simple approach, that can be applied before the event vertex has been reconstructed, is the `linefit` algorithm [126]. As illustrated in Figure 5.4 the hit pattern is fitted with a straight

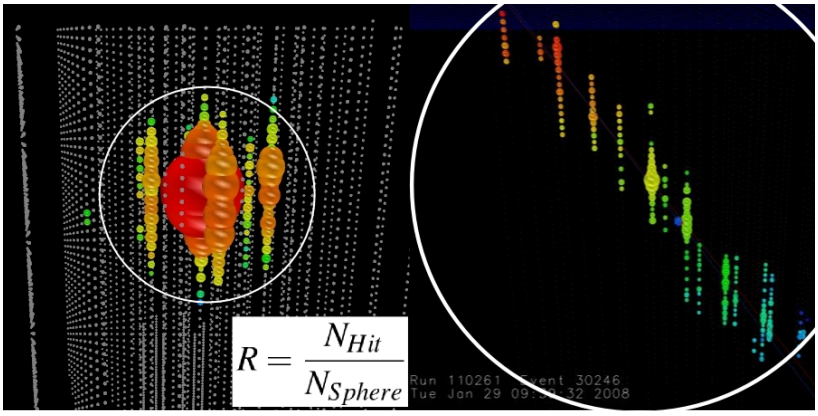

Figure 5.5: The same two events as in Figure 5.4 are shown to illustrate the fill-ratio variable f. A sphere is constructed which encloses the hit pattern. Then, the ratio of hit DOMs to the number of DOMs contained in the sphere is calculated. Spherical events result in fill-ratios close to 1, whereas for tracks the sphere tends to become large, resulting in low fill-ratios.

line propagating with velocity v_{lf}. Relativistic muons often yield `linefit` velocities close to c whereas lower velocities are obtained if the fit is applied to cascades.

If the interaction time and vertex are well-reconstructed, then causality can be used to provide a strong constraint on whether an event contains a neutrino-induced particle shower. For each DOM, light is expected to arrive at the earliest after the geometrical time t_{geo}, i.e. the time necessary to cover the distance between the DOM and the vertex, at velocity c_{ice}. While delayed photon arrivals are common due to light scattering in the ice, much earlier arrival times indicate a problem with the cascade hypothesis. The delay time t_d introduced in Eq. 4.1, which describes the difference between the expected and observed arrival time, is calculated for all DOMs. The quantity Δt_{min} is defined as the smallest such delay time $\Delta t_{\mathrm{min}} = \min(t_d)$. Events with large negative values of Δt_{min} are removed.

Another approach is to sort the DOMs by the time they recorded light and then consider the unit vector from one hit DOM to a subsequent hit DOM as an individual dipole moment. The global dipole moment m is obtained by averaging over all individual dipole moments. Larger moments are expected from tracks and smaller moments from cascades [126].

Yet another way to emphasize the different hit pattern evolution of tracks and cascades is to divide the event into two parts based on the times of the hit DOMs. This splits tracks into two disjunct segments and cascades into two mostly concentric shells (see Figure 5.6). The `cscd_llh` algorithm is used to obtain, for each half, the vertices $\vec{x}_1$ and $\vec{x}_2$. Large radial

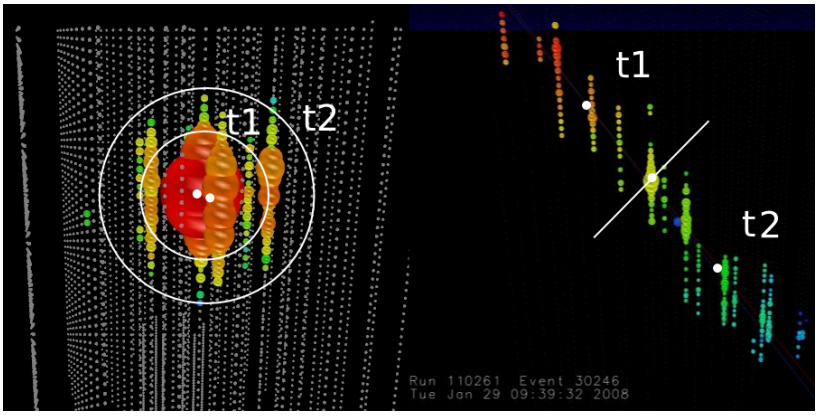

Figure 5.6: The same two events as in Figure 5.4 are shown to illustrate the use of split-reconstructions. The event is divided into two parts based on the times of the hit DOMs. This splits tracks into two disjunct segments (right) and cascades into two mostly concentric shells (left). A cascade reconstruction algorithm is applied to both parts individually to obtain a vertex (white dots). For particle showers the two vertices are close to each other, whereas for tracks larger distances are observed.

and vertical distances Δr_{12} and Δz_{12} between the vertices as well as large differences in the reconstructed time Δt_{12} are then indicative of tracks.

Another feature of cascade events, which is also related to the fact that the particle showers are only a few meters in length, is that most of the light is recorded close to the vertex and hence early in the event. In contrast, since muons emit light continuously along their track it is more likely to see later contributions to the total charge. The variable $\Delta t_{50\%-90\%}$ denotes the fraction of the event length in which the total collected charge rises from 50% to 90%. Greater $\Delta t_{50\%-90\%}$ values indicate a longer time interval for the second half of the event's total charge to be collected and are more likely to occur for muon events.

Some discrimination power comes from DOMs where just enough light arrives to trigger the readout and hence only a single pulse is reconstructed from the waveform. A combination of light yield, scattering in the ice and the geometric shape of the hit pattern results in a slightly higher number of these DOMs for muons. The ratio n_1/n_{hit} of DOMS with only one reconstructed pulse over the total number of hit DOMs tends to smaller values for cascades.

Finally, a useful variable is the ratio of the charge collected in the DOM with the highest charge, compared to the total recorded charge $q_{\text{max}}/q_{\text{tot}}$. Low energetic muons passing very close to one DOM can yield a high charge concentration in this DOM compared to others. These events can resemble cascade-like hit patterns and are prone to be overestimated in energy. Hence, requiring a low ratio $q_{\text{max}}/q_{\text{tot}}$ is useful to reject this class of background events.

5.4 Event Selection

The techniques described in the last section are combined to form a step-wise event selection that successively separates the neutrino signal from the atmospheric muon background. The individual steps are referred to as "Levels". For further reference, a summary of the event selection is given in Table 5.1 on page 89. Up to Level 3 the same event selection is used as developed for the two other cascade searches performed on the IceCube-40 datasets [14,15], from Level 4 on they diverge.

5.4.1 Level 1: Trigger Level

The first level is the trigger level, or Level 1. The trigger requirement for the IceCube-40 cascade search was the Simple Multiplicity Trigger, which required that eight DOMs were hit within a 5000 ns time window. The data rate for IceCube-40 from this trigger was approximately 1 kHz.

5.4.2 Level 2: Online Filter Level

Triggered events are filtered online at the South Pole to reduce the data volume to the bandwidth available for data transfer from the Pole via satellite [127]. The online filter, or Level 2, is a filter on easy-to-compute variables that retains the majority of the neutrino signal while removing a large fraction of the background. It requires the `linefit` velocity to be $v_{\mathrm{lf}} < 0.13\,\mathrm{m/ns}$ and the tensor-of-inertia eigenvalue ratio to be $\lambda > 0.12$. The distributions of these variables are shown in Figure 5.7. After being transferred via satellite to computing facilities in the North, additional processing takes place on the events passing the online filter. A track reconstruction is performed on the events and data quality checks are performed [14].

At this early stage of the event selection, where no event quality cuts are done yet, the distributions show some disagreement between data and simulation. Further steps in the event selection will reduce this disagreement, mostly by removing events that are too low in energy or that are not contained in the instrumented volume. The pole filter reduced the data rate by two orders of magnitude to approximately 16 Hz.

5.4.3 Level 3

Due to the energy threshold of about 100 GeV and the steeply falling energy spectrum, the energy distribution of background events passing Level 2 is strongly peaked at lower energies. As the majority of the events are still atmospheric muons most of the events are reconstructed as downgoing tracks (see Figure 5.8). Consequently, the Level 3 cuts concentrate on reducing the background at low energies.

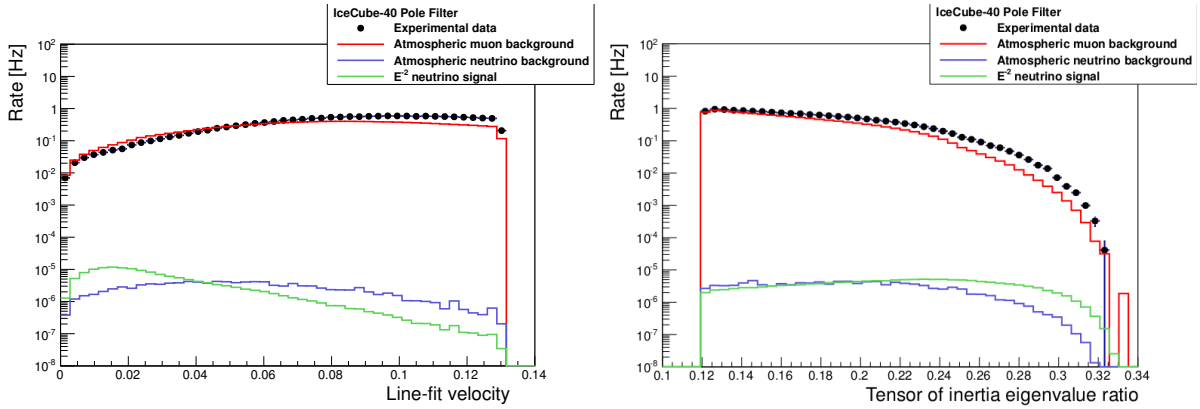

Figure 5.7: Two cuts on easy-to-compute variables define the online filter running at the Pole. Only events with large tensor-of-inertia eigenvalue ratios ($\lambda > 0.12$) and small `linefit` velocities ($v_{\mathrm{lf}} < 0.13\,\mathrm{mn}^{-1}\mathrm{s}$) are transmitted via satellite to the North where more elaborated reconstructions are performed. Plots from [128].

All events with a reconstructed energy $E_{\mathrm{ACER}} > 10\,\mathrm{TeV}$ are kept, whereas lower energetic events are subject to two more cuts. First, when reconstructed under a muon track hypothesis, events reconstructed as downgoing with zenith angles $\Theta_{\mathrm{track}} < 80°$ are rejected. Secondly, those events are removed, where a `cscd_llh` likelihood value of $\mathrm{rlogL}_{\mathrm{cscd}} > 10$ indicates a poorly fitted event. After application of the Level 3 filter the data rate is reduced by another order of magnitude to approximately 1.8 Hz, while contained astrophysical (atmospheric) neutrinos were kept with an efficiency of 76.5% (56.6%).

5.4.4 Level 4 and 5

Previous cuts aimed to provide an optimal efficiency for cascades regardless of their energy and position inside the detector. As a consequence at Level 3 a significant number of events, that are very low in energy or happening at the border of the instrumented volume, remain in the sample. For these events no reliable separation between signal and background could be found.

Therefore, at Level 4 a set of geometric conditions has been defined to remove such events: it is required that the first hit DOM is neither on the outer layer of IceCube-40 (red squares in Figure 5.3) nor in the top or bottom 50 m of the detector. Also DOMs on at least five different strings must have recorded light. This cut reduces the data rate to 79 mHz, while contained astrophysical (atmospheric) neutrinos are kept with an efficiency of 56.1% (37.2%).

After these cuts, at Level 5, additional reconstructions but no cuts were performed. In particular the remaining sample was small enough to perform the `CREDO` likelihood reconstruction

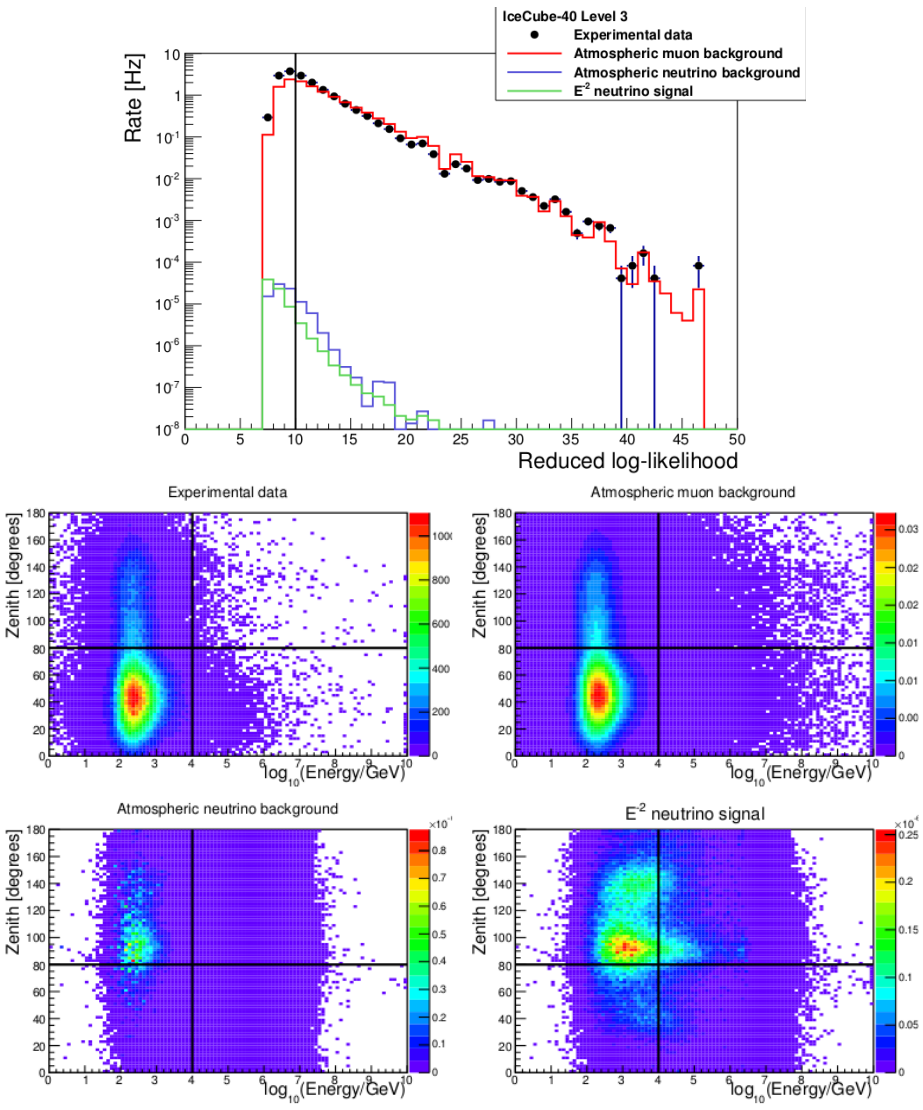

Figure 5.8: The IceCube-40 Level 3 filter variables. The upper plot shows the `cscd_llh` likelihood value $\mathrm{rlogL}_{\mathrm{cscd}}$. The data is shown by the black filled circles, simulated atmospheric muon background by the red line, simulated atmospheric electron neutrinos by the blue line, and simulated electron neutrino signal with spectrum $E^2 dN/dE = 3.6 \times 10^{-8}\,\mathrm{GeV sr^{-1} s^{-1} cm^{-2}}$ by the green line. The lower plots show the parameter space spanned by the zenith angle Θ_{track} obtained from a track reconstruction and the energy estimator E_{ACER}. Most of the background events occur below 1 TeV and reconstruct as downgoing events. Plots from [128].

described in section 5.2 with 8 iterations. Muon background still dominates over atmospheric neutrino-induced showers by three orders of magnitude at selection Level 5. Therefore, the vertex and energy estimates are used to apply another series of event selection conditions.

5.4.5 Level 6

The goal of Level 6 is to further decrease the atmospheric muon background but also to identify a set of variables which have sufficiently good discrimination power and data-to-simulation agreement to be used in a machine learning algorithm.

All available variables span a multi-dimensional parameter space. Cuts on one variable affect the distribution of all the others. Inaccuracies in the modelling of the ice, the particle interactions and the detector response lead to discrepancies between the experimental data and the Monte Carlo datasets. Often these discrepancies are observed only for a part of a variable's distribution and after removing the problematic part the data-to-simulation agreement is sufficiently good. Hence, a set of cuts had to be found which fulfilled two conditions. First of all, the cuts had to further suppress the muon background. But secondly, when cuts removed regions with unsatisfactory data-to-simulation agreement, they had to maintain or improve the agreement in all others.

In regions with unsatisfactory data-to-simulation agreement cuts affect the passing rate of experimental data and simulated muon events slightly differently. Also, the rate prediction obtained from the `CORSIKA` datasets generally underestimates the experimental data rate. By applying after each cut a normalization factor to the `CORSIKA` rate both rates are brought into agreement. At different stages in the event selection, the normalization factor ranges from 1.25 to 2.

The following cuts were found to result in an adequate data-to-simulation agreement. The distributions of the cut-variables are shown in Figure 5.9. First, the energy threshold is set to $E^{(8)}_{\mathrm{CREDO}} > 1.8\,\mathrm{TeV}$. In order to remove events where low energetic muons pass very close to a DOM and where their energy is likely to be overestimated, a cut on $q_{\mathrm{max}}/q_{\mathrm{tot}} < 0.3$ is applied. Furthermore, the containment requirement is enforced: the reconstructed vertex must lie inside the blue solid boundary shown in Figure 5.3, its z-coordinate must be inside the instrumented depth interval and also the DOM with the highest recorded charge in the event must not be on the outer layer. A constraint on the minimum delay time $\Delta t_{\mathrm{min}} > -75\,\mathrm{ns}$ is used to remove events where causality rules out the cascade hypothesis. Together with requiring a fill-ratio $f > 0.6$, this set of cuts reduces the data rate by two orders of magnitude down to 660 µHz, while retaining efficiencies for contained astrophysical and atmospheric neutrinos of 66.4% and 20.1%, respectively.

Figure 5.9 illustrates the degree to which the data and simulation agree before the Level 6 cuts. Especially depth dependent variables like $z^{(8)}_{\mathrm{CREDO}}$ illustrate the inaccuracies of the used ice model. However, after the Level 6 cuts the overall agreement of event properties between simulation and experimental data improved to be sufficiently good. The effect of the Level 6 cuts is illustrated in Figures 5.10-5.13, which compare the distributions of a selection of variables before and after the cuts. These variables were then used in the next step of the analysis.

After the cuts a normalization factor of 1.54 brings the `CORSIKA` rate and the experimental data rate into agreement. After the Level 6 cuts the shapes of the distributions of simulation and experimental data agree. Applying further cuts would not affect the passing rates of simulated and experimental data differently. Therefore, at this point in the event selection the normalization factor is fixed at the value 1.54 for the rest of the analysis.

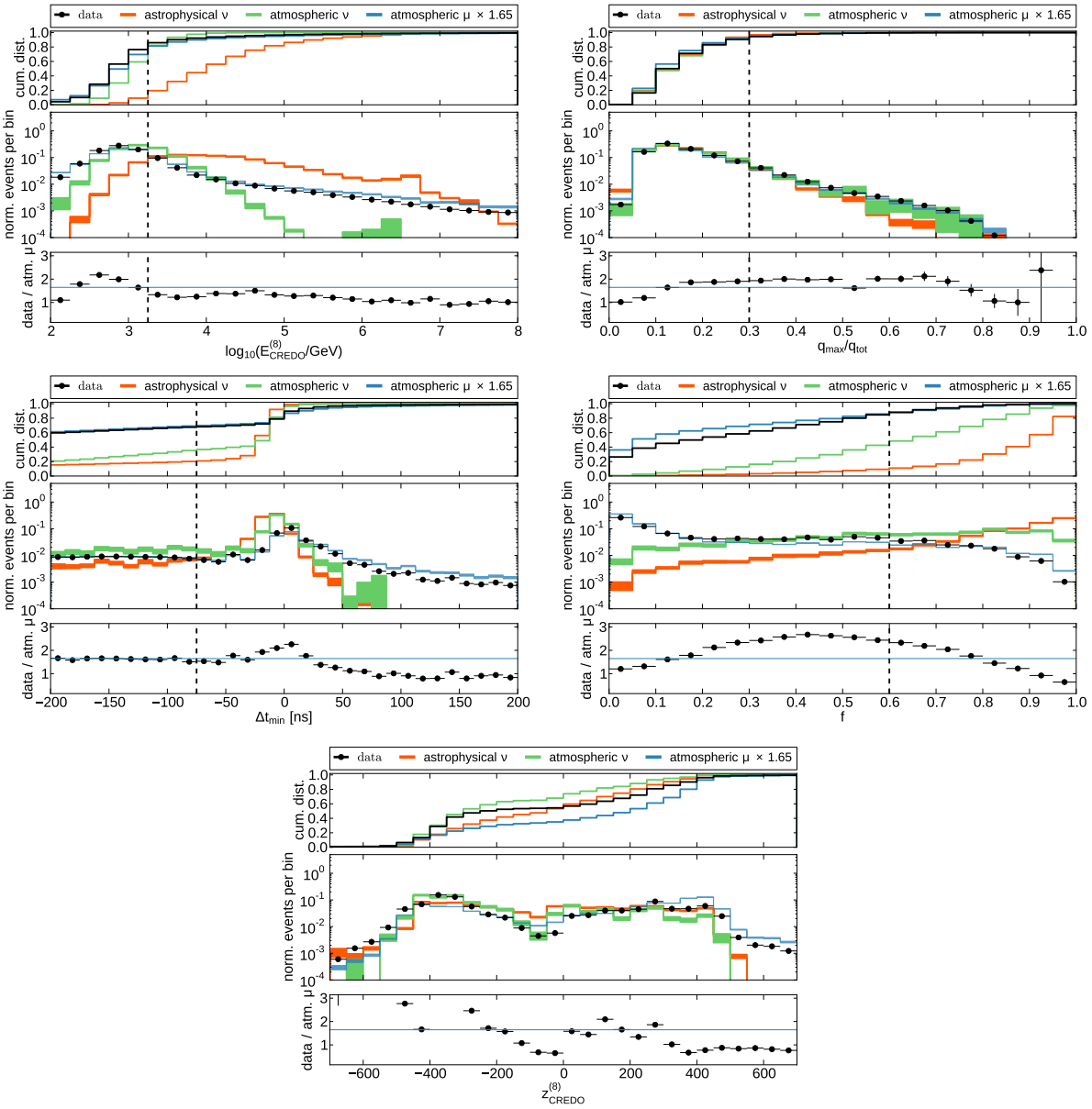

Figure 5.9: Level 6 cut variables: for each variable the normalized distributions are shown for the experimental data, the simulated atmospheric muons and neutrinos as well as for the astrophysical neutrino signal. The cumulative distributions shown in the upper panel illustrate the variable's ability to discriminate signal and background. The lower panels show the data-to-simulation agreement between the experimental data and the simulated muons. The normalization factor applied to the `CORSIKA` rate is shown in the legend. The size of the error bars and bands indicate the statistical error. Vertical dashed lines illustrate the cut.

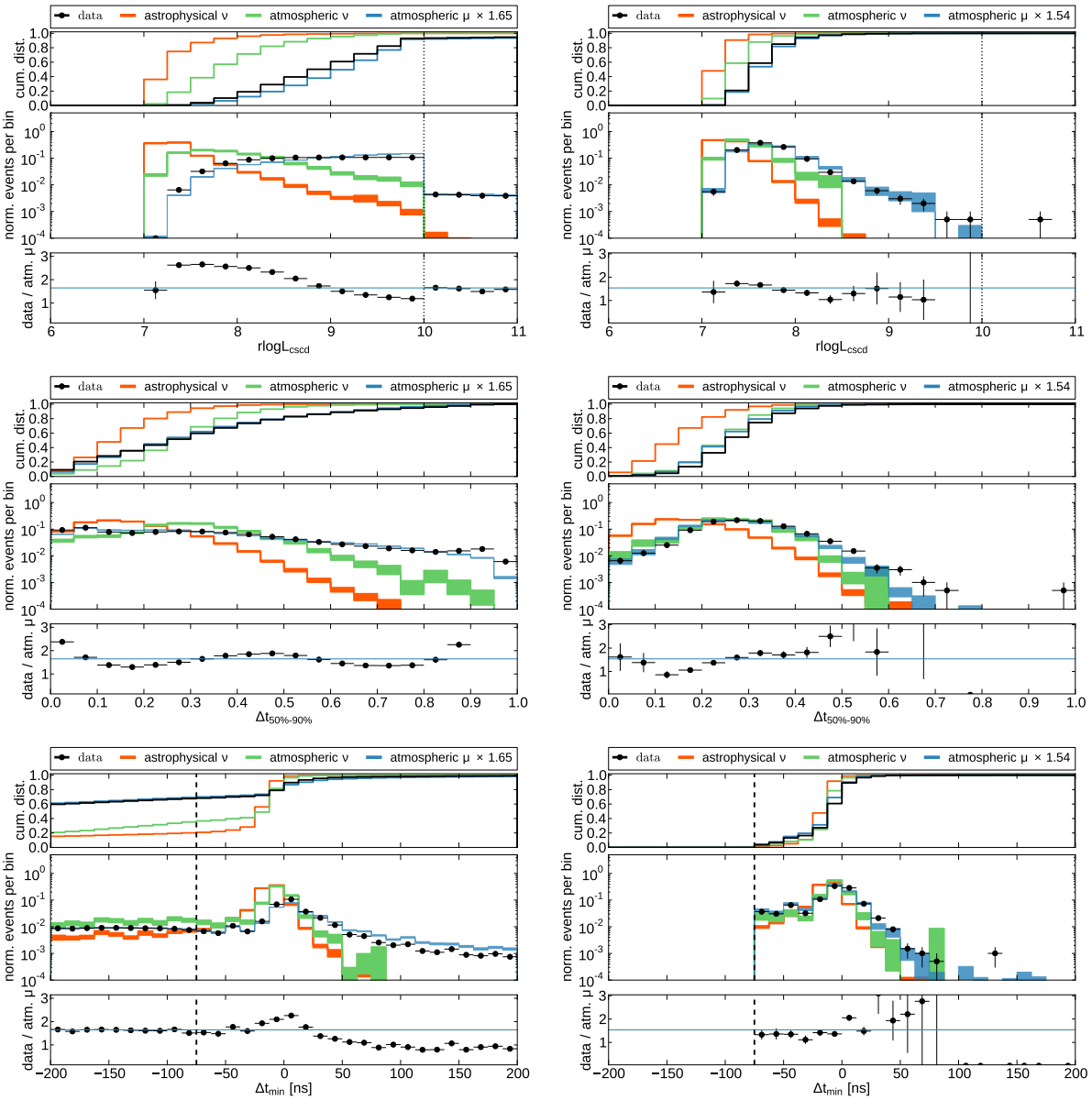

Figure 5.10: Comparison of variables before (left) and after (right) the Level 6 cuts are applied. The Level 6 cuts are shown by a dashed line. Cuts on these variables at previous Levels are indicated through dotted lines. Generally, the Level 6 cuts maintained or improved the data-to-simulation agreement. These variables enter the machine learning algorithm described in Section 5.4.6. From the top to the bottom these are: the `cscd_llh` quality of fit parameter ($\mathrm{rlogL_{cscd}}$), the fraction of the event length in which the total collected charge rises from 50% to 90% ($\Delta t_{50\%-90\%}$) and the smallest delay time (Δt_{min}). A more detailed description of each variable can be found in Section 5.3.

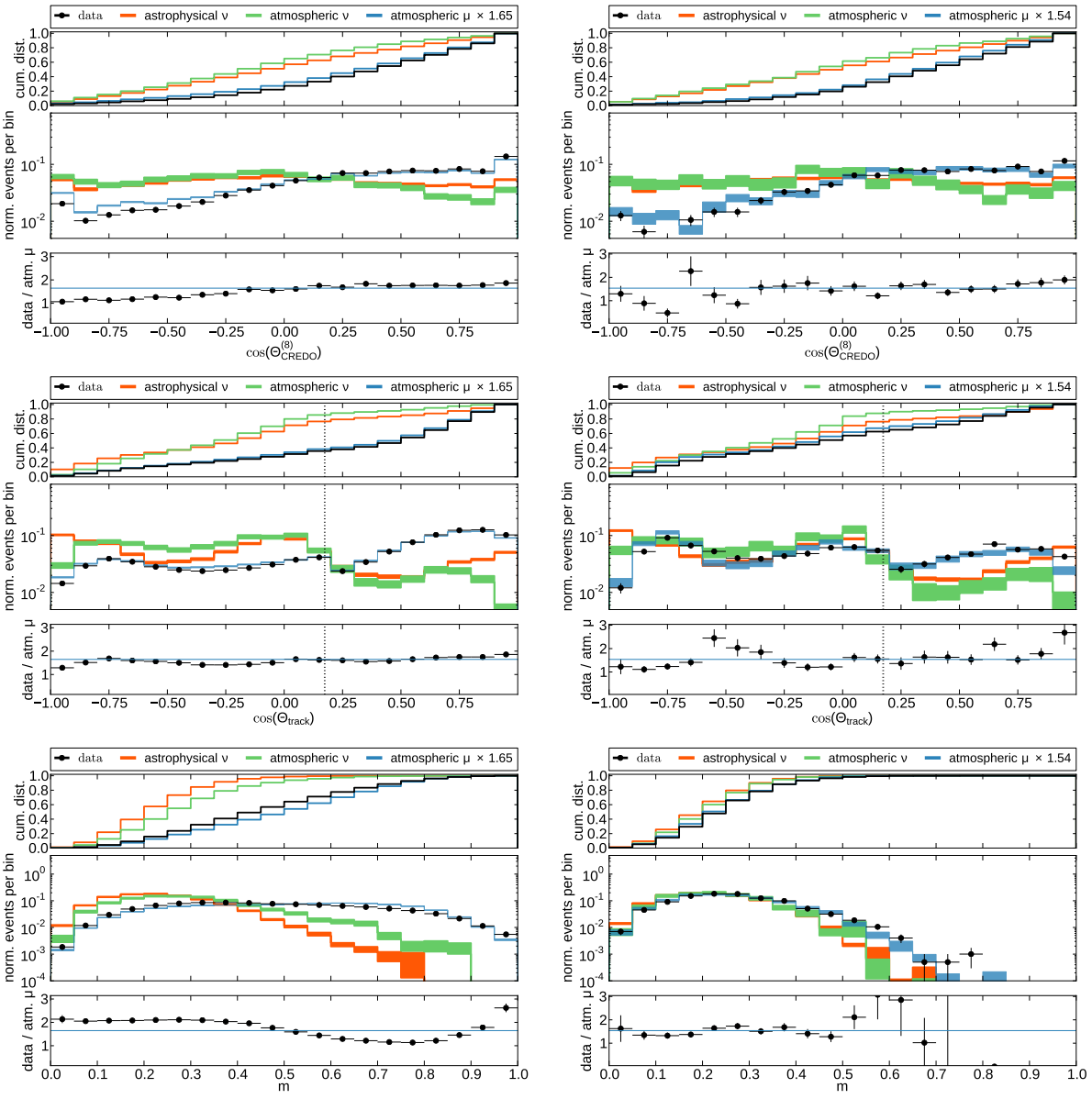

Figure 5.11: Comparison of variables before (left) and after (right) the Level 6 cuts are applied. The Level 6 cuts are shown by a dashed line. Cuts on these variables at previous Levels are indicated through dotted lines. Generally, the Level 6 cuts maintained or improved the data-to-simulation agreement. These variables enter the machine learning algorithm described in Section 5.4.6. From the top to the bottom these variables are: the cosine of the zenith angle obtained with the `CREDO` cascade reconstruction ($\cos(\Theta^{(8)}_{\mathrm{CREDO}})$), the cosine of the zenith angle obtained with a track reconstruction ($\cos(\Theta_{\mathrm{track}})$) and the dipole magnet amplitude (m). A more detailed description of each variable can be found in Section 5.3.

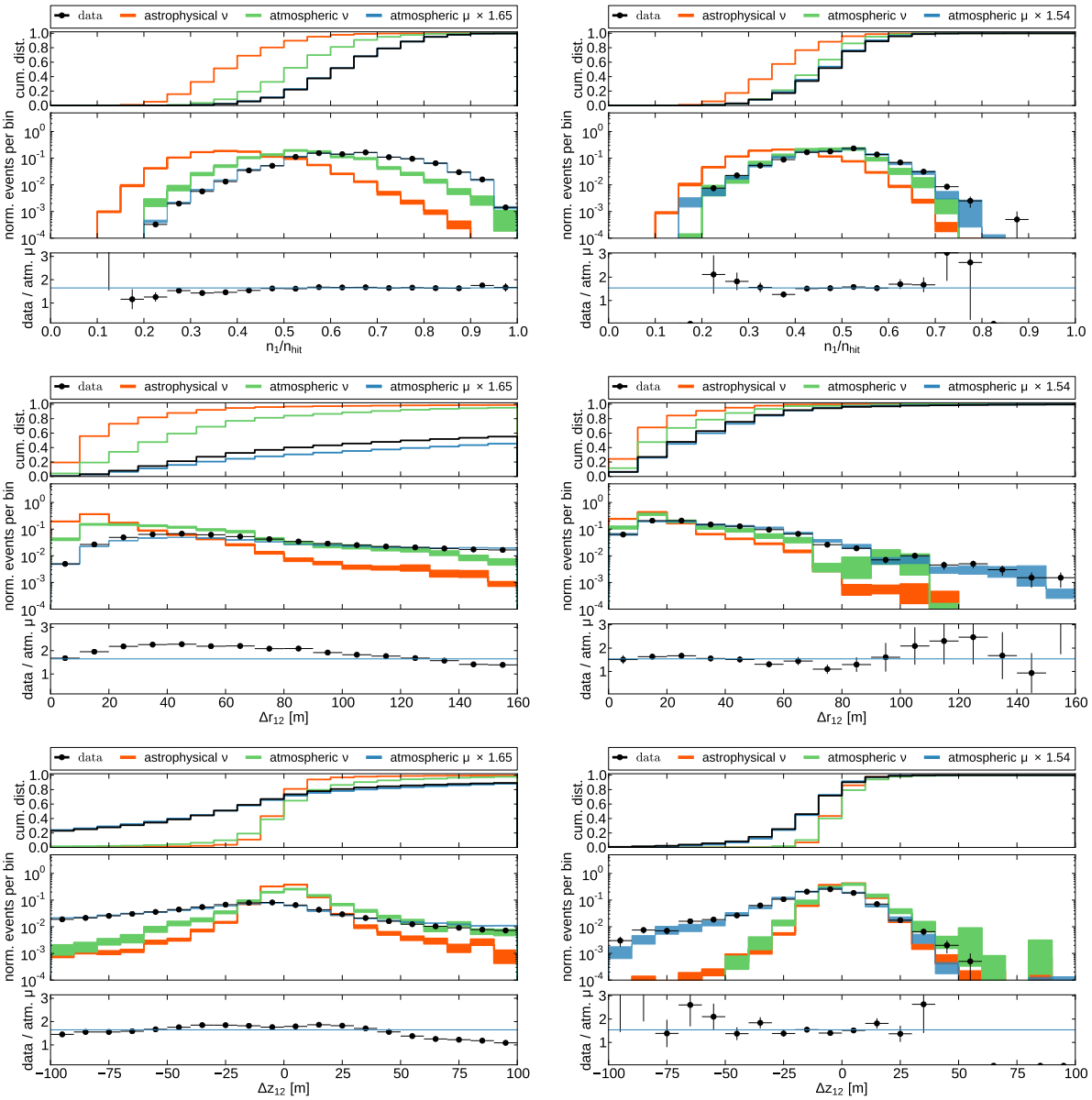

Figure 5.12: Comparison of variables before (left) and after (right) the Level 6 cuts are applied. The Level 6 cuts are shown by a dashed line. Cuts on these variables at previous Levels are indicated through dotted lines. Generally, the Level 6 cuts maintained or improved the data-to-simulation agreement. These variables enter the machine learning algorithm described in Section 5.4.6. From the top to the bottom these variables are: The ratio of DOMS with only one reconstructed pulse over the total number of hit DOMs (n_1/n_{hit}) as well as the radial and vertical distances between split reconstructions ($\Delta r_{12}, \Delta z_{12}$). A more detailed description of each variable can be found in Section 5.3.

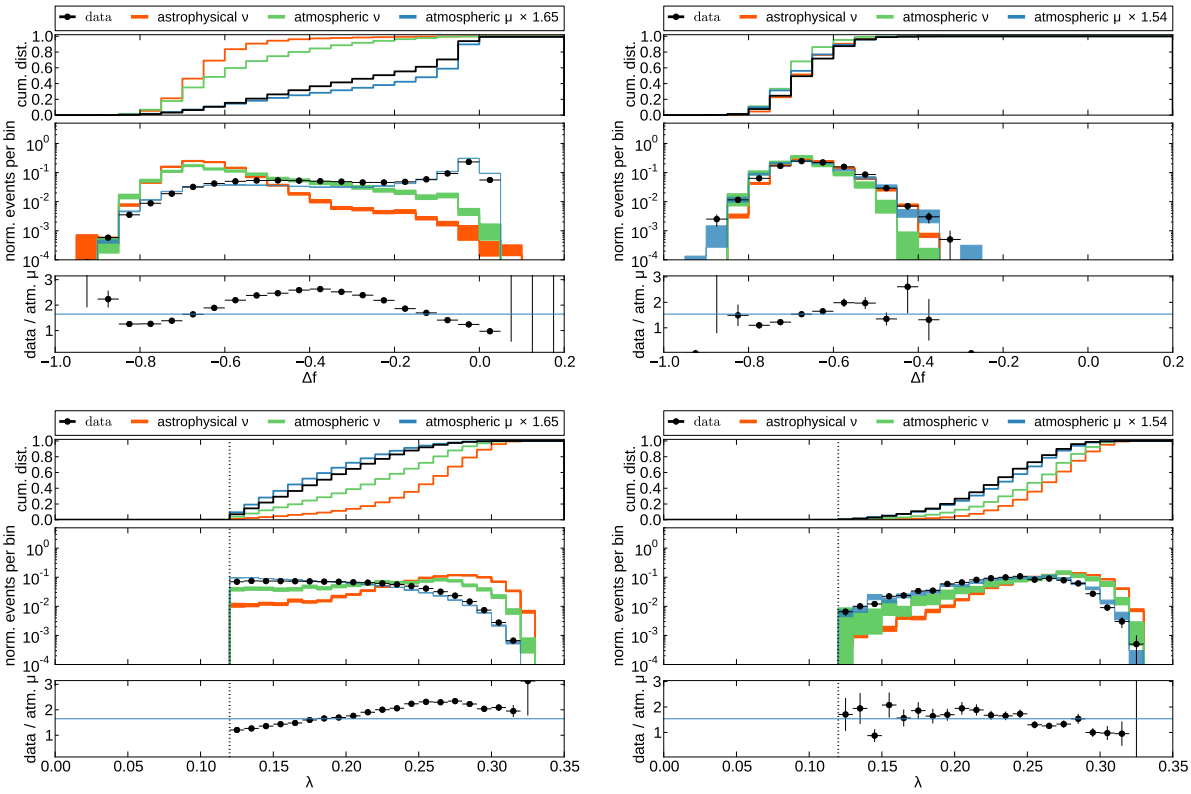

Figure 5.13: Comparison of variables before (left) and after (right) the Level 6 cuts are applied. The Level 6 cuts are shown by a dashed line. Cuts on these variables at previous Levels are indicated through dotted lines. Generally, the Level 6 cuts maintained or improved the data-to-simulation agreement. These variables enter the machine learning algorithm described in Section 5.4.6. From the top to the bottom these variables are: the fill-ratio difference (Δf) and the tensor-of-inertia eigenvalue ratio (λ). A more detailed description of each variable can be found in Section 5.3.

5.4.6 Event Classification with boosted decision trees

The final step of the event selection is to remove the remaining background and obtain a sample dominated by neutrinos. For this purpose event properties that still provide separation power are used as input to a multivariate algorithm to obtain a single quality parameter for each event. The TMVA package [129] is used to train a boosted decision tree (BDT).

The input variables to the algorithm span a parameter space in which separable signal and background events of a training dataset occupy different regions. A partitioning of the parameter space needs to be found which separates the signal and background regions best. Decision trees

implement this partitioning as a set of straight cuts. A cut on one variable splits the parameter space into two regions. Each of these regions is split again by cutting on another variable. Further cuts are chosen until a stopping condition is fulfilled. Each of the resulting hypercubes is classified as either more signal-like or more background-like depending on which class of events of the training sample dominates there. The training sample is used to construct the decision tree which is afterwards used to classify arbitrary events: events are labeled signal-like or background-like depending on which hypercube in the parameter space they occupy. The name "decision tree" originates from the fact that this way of partitioning resembles binary trees [130].

Boosted decision trees are an extension of the concept of decision trees by replacing a single tree with a forest of N trees. Boosting refers to an iterative technique where after classifier i has been trained the misclassified events are used to train classifier $i+1$, which is specifically tailored to these events. The method employed here is called adaptive boosting (AdaBoost) [129]. First a decision tree is trained and the fraction of misclassified training events $\epsilon \leq 0.5$ is calculated. These events are then given a boost weight:

$$\alpha = \frac{1-\epsilon}{\epsilon} > 1. \tag{5.7}$$

The sum of all weights in the event sample is kept constant by normalizing the weights. With the boost weights applied the previously misclassified events are more important during the training of the next tree, which therefore learns the specifics of these events. This procedure is repeated until all N trees are trained. The output $h_i(\boldsymbol{x})$ of decision tree i in the forest classifies an event, described by the vector of input variables $\boldsymbol{x}$, as either signal-like ($h_i(\boldsymbol{x}) = +1$) or background-like ($h_i(\boldsymbol{x}) = -1$). The outputs of all trees are combined to a single parameter:

$$BDT = \frac{1}{N}\sum_{i}^{N} \ln(\alpha_i) \cdot h_i, \tag{5.8}$$

which tends to small values for background-like events and to large values for signal-like events.

A BDT classifier is trained to separate simulated electron neutrinos weighted according to an E^{-2} spectrum (signal) from `CORSIKA` events (background. The 11 variables shown in the Figures 5.10-5.13 are used to train the BDT and the resulting score is used as one final event quality variable BDT. The variables are the `cscd_llh` algorithm's quality parameter $\mathrm{rlogL_{cscd}}$, the vertical and radial distances $\Delta z_{12}, \Delta r_{12}$ of the time-split reconstructions, the fraction of DOMs with only one reconstructed pulse n_1/n_{hit} and the fraction of the event duration needed to accumulate the second half of the total charge $\Delta t_{50\%-90\%}$. The two zenith angle estimators $\Theta^{(8)}_{\mathrm{CREDO}}$ and Θ_{track} enter the BDT. The use of `CREDO`'s reconstructed cascade direction is

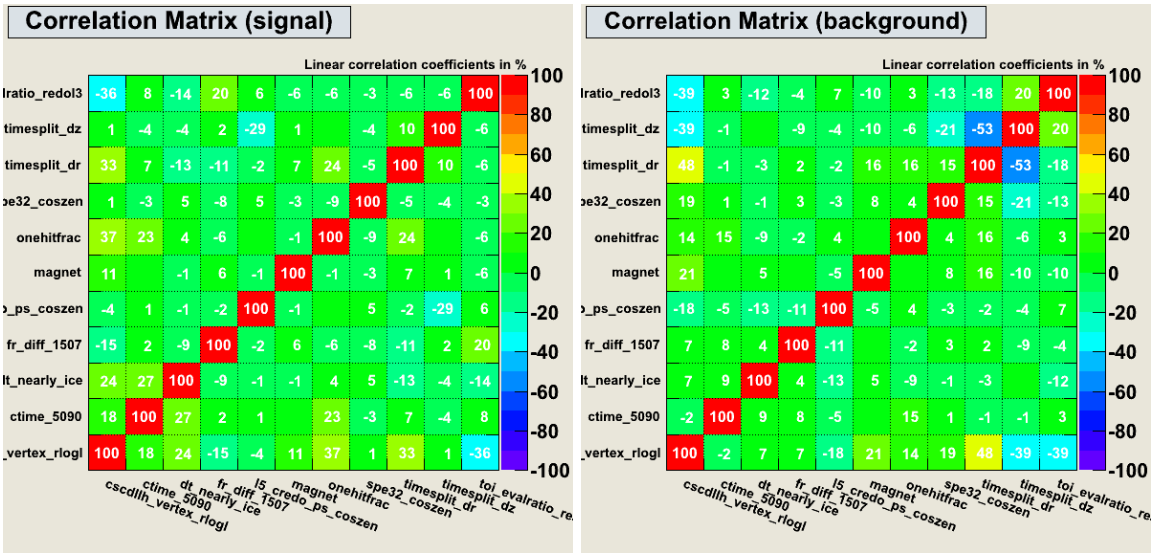

Figure 5.14: Linear correlation coefficients of the BDT input variables for signal events (left) and background events (right).

noteworthy as IceCube-40 is the first detector configuration in which the cascade direction is sufficiently well constrained to be used in the analysis. The next two variables that enter the BDT are the dipole moment m and the fill-ratio difference for two radii Δf. Finally, the eigenvalue ratio λ and the minimum delay time Δt_{min} are used, too. They have already been used at earlier cut levels but still provide some discrimination power. As illustrated in Figure 5.14 the chosen set of input variables exhibit only small correlations between individual variables.

The signal and background samples given to TMVA are again split into a training and a test sample. The BDT is trained with the former. Then the classification result is cross-checked with the test sample. When the distribution of the BDT output variable is different for the training and test samples this indicates that the classifier has been overtrained. In that case it identifies the specifics of the training set rather than the characteristic differences between the signal and background datasets. The overtraining check is illustrated in Figure 5.15. The comparison of the BDT distributions of the test and training samples agree sufficiently well. An additional overtraining check is possible for the background sample by comparing the BDT distribution of `CORSIKA` events and the experimental data (see Figure 5.16).

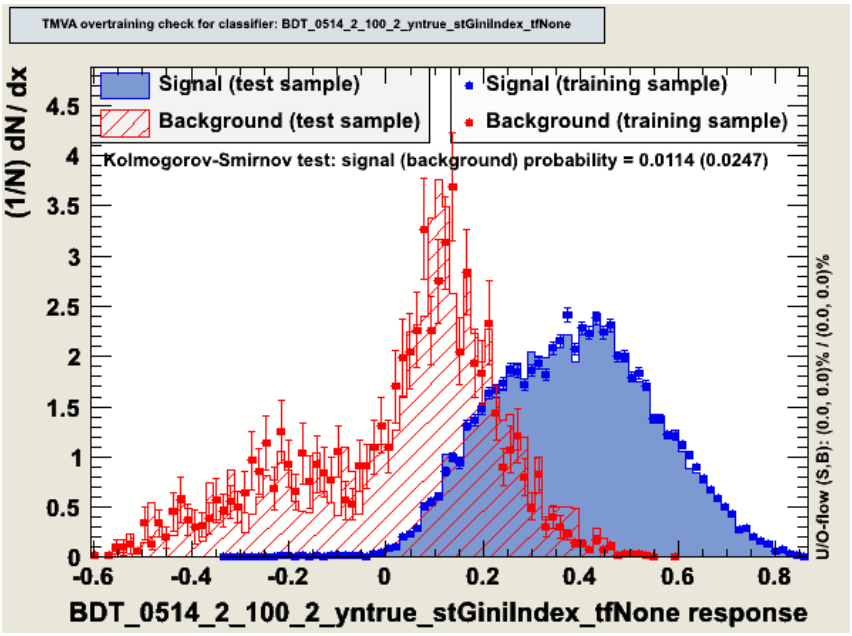

Figure 5.15: The distribution of the BDT output variable is compared for the training and test samples and for signal and background, respectively. No signs of overtraining are found.

5.4.7 Search for atmospheric neutrinos

The distribution of the BDT output variable and its ability to separate signal from background is shown in Figure 5.16. The good data-to-simulation agreement of the input parameters result in a similar good agreement for the BDT output variable. At low values, the distribution is dominated by the atmospheric muon background and the experimental data is adequately described by the `CORSIKA` simulation.

The neutrino distributions center at higher BDT scores, but even there a contribution from atmospheric muons is present. Closer inspection reveals that these events are muons with prominent bremsstrahlung cascades and little to no hint of the muon track. The events resemble neutrino-induced particle showers rather well. This is illustrated by event displays of `CORSIKA` events and experimental data events with a BDT scores > 0.5 in Figures 5.17 and 5.18.

The geometry of IceCube-40 with one dimension being much shorter than the others is obviously vulnerable to this class of background events. In the energy range below 100 TeV, with the given detector and the aforementioned background rejection methods, including their combination within a multivariate classifier, these events turn out to be irreducible background.

This limits the possible background suppression for this sample. Atmospheric neutrino signal

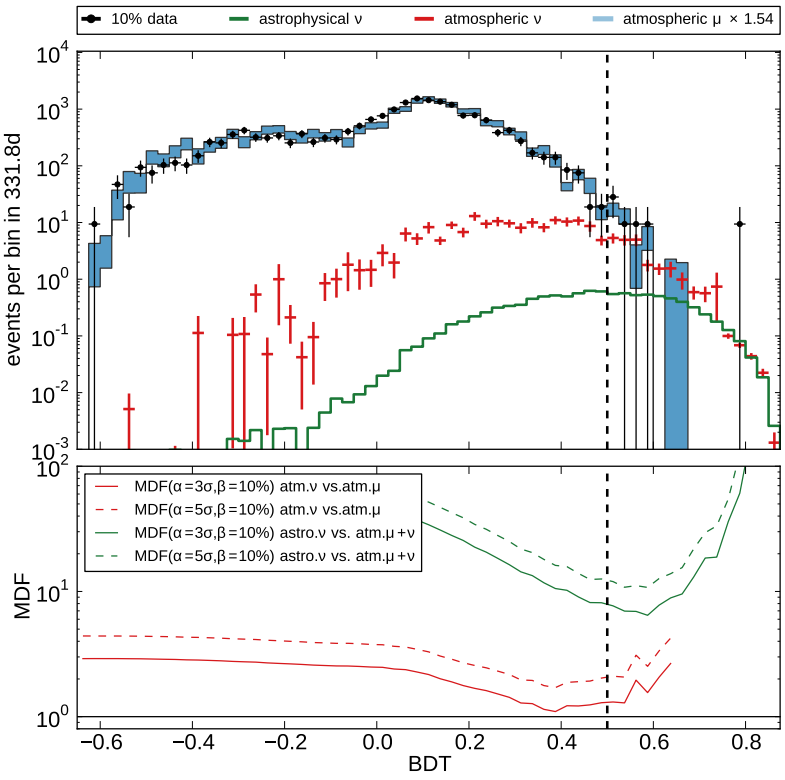

Figure 5.16: The distribution of the BDT output variable. The cut on this variable is chosen by minimizing the model discovery factor (MDF) shown in the lower panel. A cut of BDT > 0.5 is found to be optimal.

and muon background are similarly distributed at BDT scores > 0.5. Cutting at a higher value removes the atmospheric neutrino signal as much as the atmospheric muon background.

The optimal separation point between background and signal is chosen by maximizing the detection potential for an atmospheric neutrino flux [131, 132].

The detection potential is quantified with the model discovery factor:

$$MDF = \frac{\mu_{\mathrm{lds}}(\alpha, \beta, \mu_{\mathrm{bg}})}{\mu_{\mathrm{sig}}}, \tag{5.9}$$

where μ_{sig} and μ_{bg} are the predicted passing rates of signal and background events. The least detectable signal $\mu_{\mathrm{lds}}(\alpha, \beta, \mu_{\mathrm{bg}})$ denotes the signal prediction required to obtain an observation at significance level α with probability $(1 - \beta)$. A cut that minimizes the MDF is optimal.

The lower panel of Figure 5.16 illustrates the MDF calculated for a 90% chance to obtain a 3σ or 5σ observation of atmospheric neutrinos. With MDF values > 1 a 5σ observation is out of reach. But the 3σ-MDF gets close to 1 for BDT values of $0.4 - 0.5$. In this range it forms a nearly flat plateau with some statistical fluctuations before increasing for values of BDT > 0.5. Therefore, a BDT value of 0.5 at the end of the plateau is the optimal separation point. Events passing this cut form the low-energy sample of this analysis.

The 10% sample used to develop the cuts contains 7 casade-like events which pass this cut (see Figure 5.18). Hence, for the 90% sample a rather large number of 71 events is expected. From these events 41 are expected to be atmospheric muons and 30 conventional and prompt neutrinos. Both numbers are affected by rather large systematic uncertainties (see discussion in Section 5.5).

The lowest model discovery factor for an astrophysical neutrino flux of all-flavor intensity $\mathrm{E}^2\Phi = 3.6 \cdot 10^{-8}\,\mathrm{GeVsr^{-1}s^{-1}cm^{-2}}$ is reached at a BDT score of 0.6 (see Figure 5.16). There the least detectable flux with a 90% chance to obtain a 3σ discovery is still 6.5 times higher than the intensity given above. Hence, the low-energy sample's discovery potential for astrophysical neutrinos is low.

5.4.8 Search for astrophysical neutrinos

The remaining background events can be removed by increasing the energy threshold of the analysis. Because of their steeply falling spectrum conventional atmospheric neutrinos are severely reduced by an energy cut. However, the harder spectra of prompt neutrinos and the assumed diffuse astrophysical neutrino flux are not so much affected. This fact is used to define the high-energy sample with an energy threshold of $E^{(8)}_{\mathrm{CREDO}} > 100\,\mathrm{TeV}$. A comparatively loose requirement on the BDT score of BDT > 0.1 is then sufficient to remove all simulated background events (see Fig. 5.19). In contrast to the low energy sample, which was designed to find atmospheric neutrinos, this sample has a significantly better performance for detecting a prompt or astrophysical neutrino flux. In fact, of the 10% experimental data sample one event with $135 \pm 50\,\mathrm{TeV}$ survives the high-energy event selection, whereas it is removed by the tighter BDT cut of the low-energy sample.

For this sample, the background contribution of atmospheric muons cannot be determined from simulation anymore as all events have been removed. In order to estimate the muon rate, the reconstructed energy distribution is extrapolated from the low-energy region, where simulated events are still available, to higher energies.

As shown in the last section, the atmospheric muon events that survive up to this point in the event selection are muons with catastrophic energy losses. They resemble neutrino-

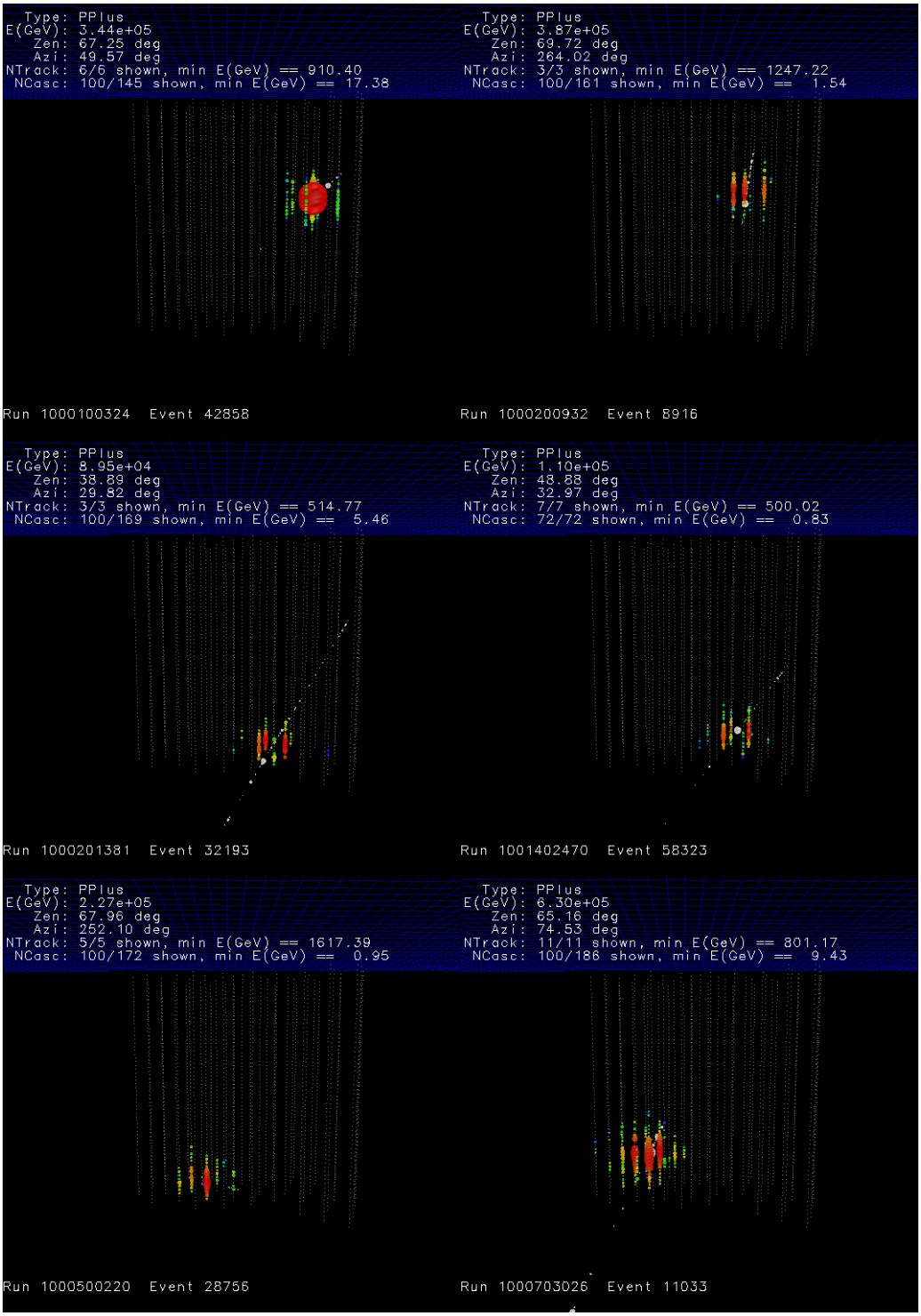

Figure 5.17: Selection of simulated muon events in the low-energy sample. These events resemble the hit-patterns of neutrino-induced cascades and form an irreducible background.

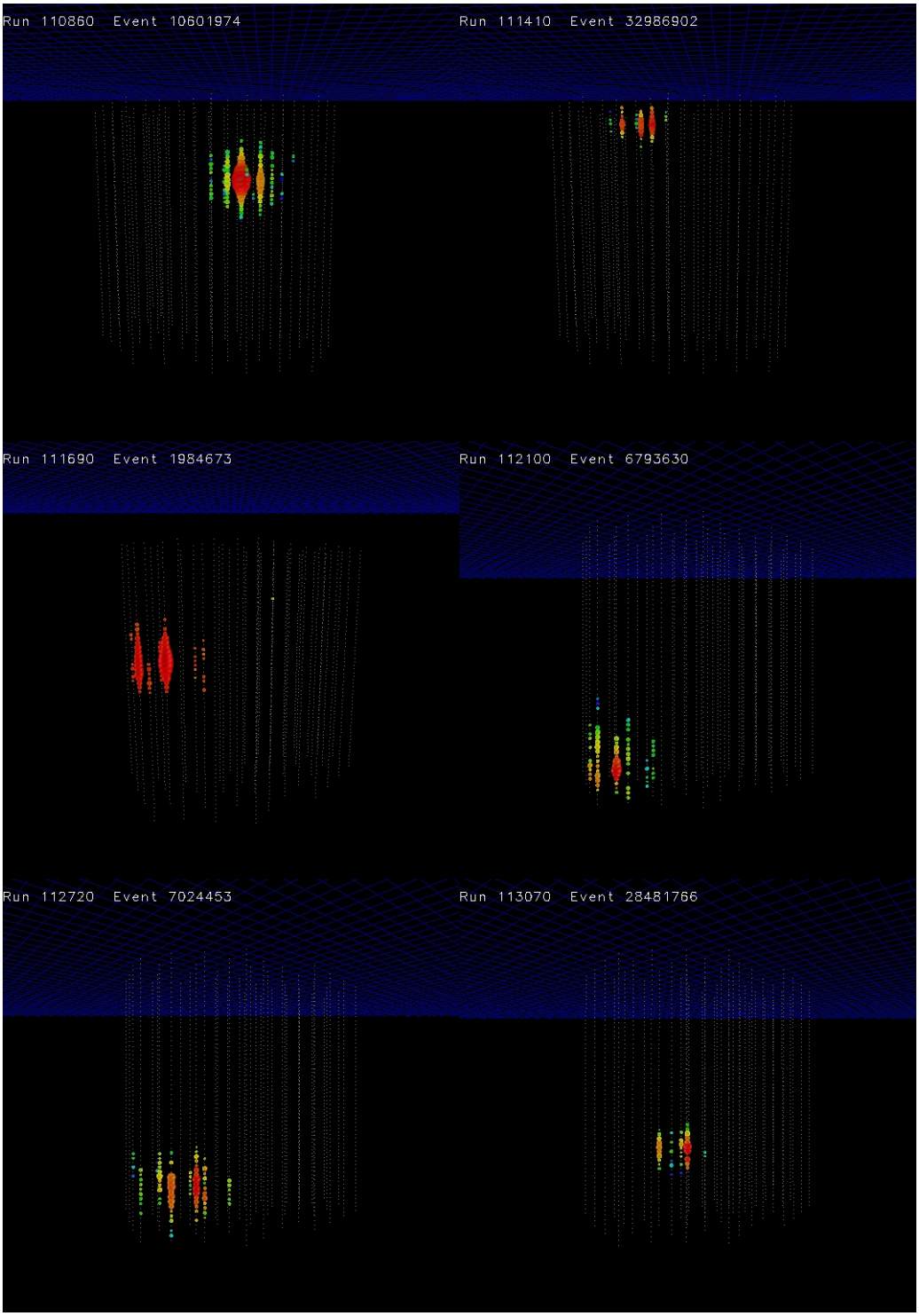

Figure 5.18: 6 of 7 events in the 10% sample used to develop that pass the event selection of the low-energy sample.

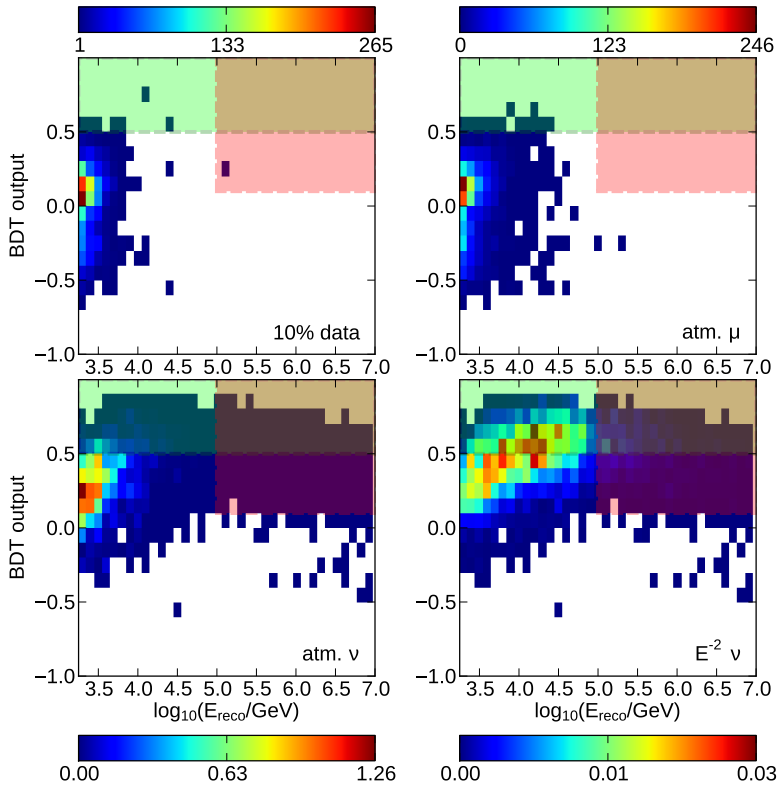

Figure 5.19: The parameter space spanned by the BDT output variable and the reconstructed energy. The green shaded area (BDT $>$ 0.5) and the red shaded area (BDT $>$ 0.1)&($\log_{10}(E_{\mathrm{reco}}/\,\mathrm{GeV}) > 5$) denote the cuts of the low-energy and high-energy samples, respectively. The color scale denotes linearly the expected/seen number of events per bin in 10% of the livetime.

induced particle showers very much. The energy spectrum of the brightest bremsstrahlung cascades along simulated muon tracks, unaffected by any detector effects, has been studied with simulated events. Up to PeV energies, the energy spectrum can be described by a power law $dN/dE \propto E^{-3.72}$. For muon events passing the event selection the corresponding energy spectrum is not necessarily the same because of the energy-dependent performance of the cuts. For example muon events with bright bremsstrahlung cascades are suppressed with increasing energy, since the muon becomes more likely to be detected in the veto region. On the other hand, the selection efficiency for particle showers rises with increasing deposited energy. The selection efficiency of the BDT cut ϵ for contained particle showers as a function of deposited energy has

been derived from simulated electron neutrino events (see the left plot of Figure 5.20).

The reconstructed energy spectrum of CORSIKA events below 100 TeV is shown in the right plot of Figure 5.20. The same BDT score > 0.1 is required for these events as for the events in the high-energy sample. Three models have been tested to extrapolate the muon background into the signal region. The first model represents the spectrum of the bremsstrahlung cascades as given above. It fits the normalization of the power law[2] $dN/dE = 10^a \cdot (E/\mathrm{GeV})^b$ with $b = -2.72$. In the second model also the index of the power law is left free. The last model is the product of two functions: the aforementioned selection efficiency ϵ for particle showers as a function of deposited energy and a power law with the index and normalization as free parameters: $dN/dE = \epsilon \cdot 10^a \cdot (E/\mathrm{GeV})^{-b}$.

The third model provides a reasonable fit to the energy spectrum of the last CORSIKA events. Instead of the index -3.72 given above, the fit results in a slope of -4.43 ± 0.06. As it has been motivated above, this difference in slope can be attributed to the improving rejection capabilities of the veto region. With a $\chi^2/\mathrm{ndof} = 6.3/4$ this model is a better fit than the two other tested models ($\chi^2/\mathrm{ndof} = 19.8/4$ and $\chi^2/\mathrm{ndof} = 22.3/5$). The fit is consistent with the expectation that the remaining background events are dominated by high bremsstrahlung cascades and that the energy estimator describes their energy spectrum. This confirms the physical motivation of the extrapolation in the signal region. From the extrapolation one can amount the muon contribution to $0.04^{+0.06}_{-0.02}$ events, where the errors are derived from varying the parameters within the uncertainties obtained from the fit. Additional 0.21 events are expected from conventional and prompt atmospheric neutrinos.

This event selection reduces the muon background by seven orders of magnitude from the rate after the online filter. This high suppression comes at the price of a low total efficiency of 5% (0.5%) for contained astrophysical (atmospheric) neutrinos.

The energy-dependent selection efficiencies are presented in the form of effective areas for both samples in Figure 5.21. This quantity, which can be interpreted as the size of a hypothetical, 100% efficient detector translates the neutrino flux into an event rate:

$$\frac{dN}{dt} = \Omega \int dE A_{\mathrm{eff}}(E) \frac{dN_\nu}{dE dA dt d\Omega}. \tag{5.10}$$

Table 5.2 summarizes the performance of both event selections at different cut levels.

[2] The index is shifted by one because the integrated bin content is fitted in Figure 5.20.

	low-energy sample	high-energy sample
Optimized for	Atmospheric neutrinos	Astrophysical neutrinos
Level 1	light recorded on 8 different DOMs within a 5 µs time window	
Level 2	$v_{\mathrm{lf}} < 0.13\,\mathrm{m/ns}$, $\lambda > 0.12$	
Level 3	($E_{\mathrm{ACER}} > 10\,\mathrm{TeV}$) or ($E_{\mathrm{ACER}} < 10\,\mathrm{TeV}$, $\Theta_{\mathrm{track}} > 80°$, $\mathrm{rlogL_{cscd}} < 10$)	
Level 4	$N_{\mathrm{strings}} > 5$, $-450\,\mathrm{m} < z_{1^{\mathrm{st}}} < +450\,\mathrm{m}$, DOM with first hit not on outer string	
Level 5/6	DOM with largest charge not on outer string, $\vec{x}^{(8)}_{\mathrm{CREDO}}$ contained, $-500\,\mathrm{m} < z^{(8)}_{\mathrm{CREDO}} < +500\,\mathrm{m}$, $E^{(8)}_{\mathrm{CREDO}} > 1.8\,\mathrm{TeV}$, $\Delta t_{\mathrm{min}} > -75\,\mathrm{ns}$, $q_{\mathrm{max}}/q_{\mathrm{total}} < 0.3$, $f > 0.6$	
BDT input	$\mathrm{rlogL_{cscd}}, \Delta r_{12}, \Delta z_{12}, n_1/n_{\mathrm{hit}}, \Delta t_{50\%-90\%}, \Delta t_{\mathrm{min}}$, $\cos(\Theta^{(8)}_{\mathrm{CREDO}}), \cos(\Theta_{\mathrm{track}}), \Delta f, \lambda, m$	
Final Cuts	$BDT > 0.5$	$BDT > 0.1$ $E^{(8)}_{\mathrm{CREDO}} > 100\,\mathrm{TeV}$

Table 5.1: Overview of the event selections. The symbols used here are described in section 5.3.

Cut Level	Experimental data	Contained neutrinos	
		$3.6 \times 10^{-8} E^{-2}$	HKKMS07 (no knee)
	Rates in µHz		
Level 2	16.03×10^6	1.28 ± 0.03	153 ± 4
Level 3	1.74×10^6	0.97 ± 0.01	86 ± 1
Level 4/5	78980	0.550 ± 0.008	32.1 ± 0.7
Level 6	660	0.365 ± 0.006	6.5 ± 0.3
low-energy sample	2.34	0.156 ± 0.004	0.73 ± 0.08
high-energy sample	0.105	0.068 ± 0.001	0.0021 ± 0.0003
	Efficiencies with respect to previous level		
Level 3	10.8%	76.5%	56.6%
Level 4/5	4.5%	56.1%	37.2%
Level 6	0.8%	66.4%	20.1%
low-energy sample	0.4%	42.8%	11.3%
high-energy sample	0.02%	18.6%	0.04%

Table 5.2: Event rates and cut efficiencies at the different levels leading to the low-energy and high-energy samples. While the data column refers to all recorded events that pass the cuts, the neutrino rates refer to contained events, i.e. neutrinos which have their interaction vertex inside the area circumscribed by the blue solid line in Fig. 5.3. For charged current ν_μ interactions the muon must have its highest energy loss inside the area.

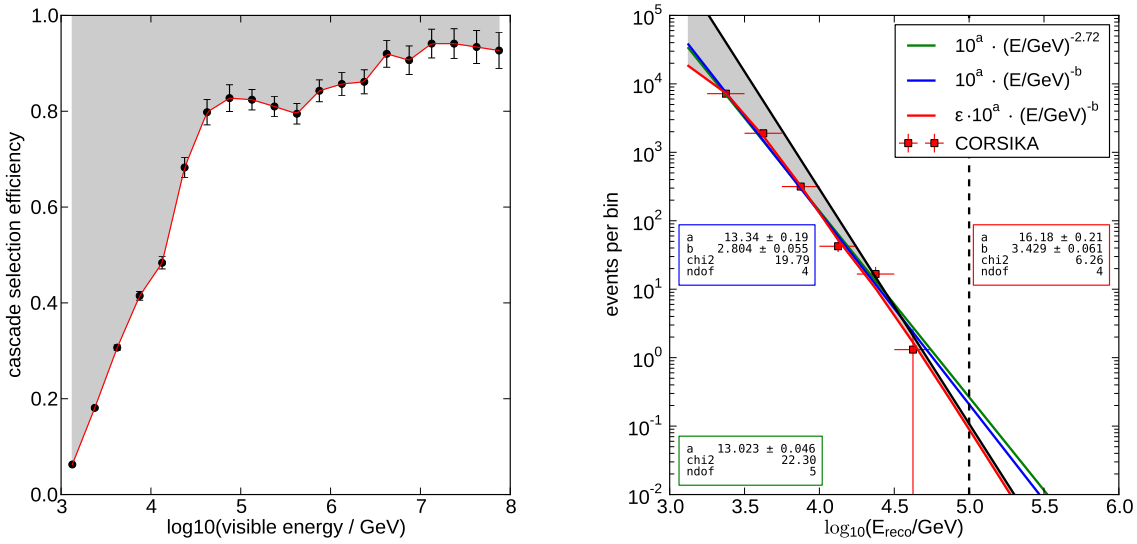

Figure 5.20: Left: The selection efficiency ϵ for particle showers as a function of deposited energy. Right: The reconstructed energy spectrum of the last `CORSIKA` events. Three models are fitted to the spectrum to obtain an extrapolation to energies above 100 TeV. The model plotted in red is the product of a power law and the efficiency shown in the left plot. The influence of the efficiency in this model is illustrated through the grey shaded area.

5.5 Systematic Uncertainties

Both event selections face sizable systematic uncertainties. The largest uncertainties on the expected event count arise from the limited knowledge of the optical ice properties at the South Pole, the selection efficiency of the muon background and the theoretical predictions for the atmospheric neutrino flux. Table 5.3 summarizes the systematic uncertainties for the low-energy and high-energy samples. In the following individual sources of systematic uncertainties are discussed in more detail.

As shown in the Sections 3.4 and 4.1 the knowledge about the optical properties of the detector is reflected in so-called ice models. The AHA ice model [98] was used in all simulations for this analysis. For a study of the uncertainties arising from the ice model, simulated neutrino datasets were produced using an alternative ice model, called SPICE [133] which was developed after this analysis was completed. The systematic uncertainty from the ice models was estimated to be $\pm 24\%$ for an E^{-2} neutrino spectrum signal and $\pm 11\%$ for the atmospheric neutrino background for both samples.

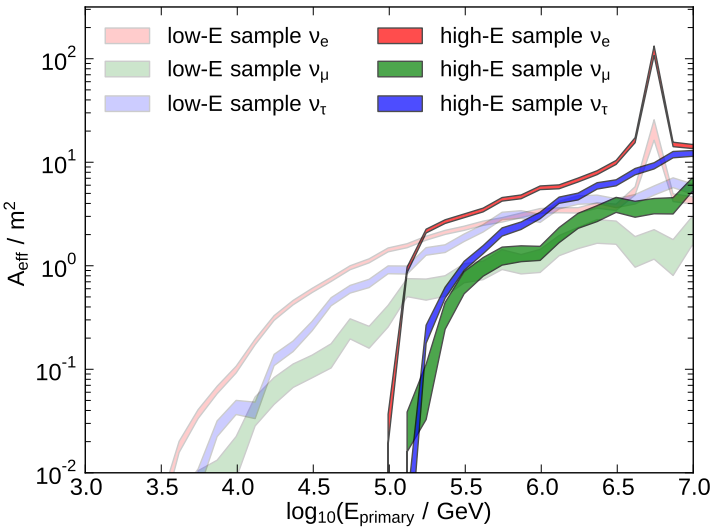

Figure 5.21: This plot shows the effective area of the low- and high-energy samples and of each neutrino flavor. The effective area culminates for electron neutrinos at the Glashow resonance at 6.3 PeV. While the low-energy sample has a lower energy threshold the BDT cut limits the effective area at higher energies. The high-energy sample has a looser BDT cut and therefore eventually reaches a higher effective area.

The estimate of the rate of atmospheric muons that pass the selection cuts is also affected by a rather large uncertainty. The simulation falls short in providing an absolute rate estimate, by systematically underestimating the measured muon rate. At cut levels before Level 6, where the data-to-simulation agreement is not yet optimal, cuts affect data and simulation events slightly differently. Hence, the rate discrepancy changes slightly between cut levels. At each of these levels the rate estimate from atmospheric muon simulation can be normalized to match the measured data rate by applying factors of 1.25–2. As described in section 5.4, the event selection removes problematic event classes and creates a sample with good data-to-simulation agreement before training the boosted decision tree. At that point the normalization factor is 1.54 and is fixed for the rest of the analysis. The observed ±50% variation of this normalization factor at early cut levels is used as an estimate for the total systematic uncertainty on the muon rate of the low energy sample. The variation encompasses uncertainties on the cosmic-ray spectrum and composition, the particle interactions within air showers, the DOM efficiencies (see below) and the optical properties of the ice. About 10% of it can be attributed to the uncertainty of the cosmic-ray energy spectrum. This value is obtained by varying the broken power law parameters in the range of their published uncertainties [119]. Optimally, the other uncertainties would be

quantified by varying the respective parameters in the simulation. However, the generation of several additional sufficiently sized background samples is computationally intractable. Hence, the empirical estimate of 50% uncertainty for the atmospheric muon background is used.

For the high energy sample the atmospheric muon background is estimated from a fit of the reconstructed energy distribution and its extrapolation to higher energies. From varying the fitted parameters within the uncertainties reported by the fit, the systematic uncertainty of the muon rate in the high energy sample is estimated to be $(-50\%, +150\%)$. This uncertainty is larger than for the low energy sample. However, here the background contribution from atmospheric muons is much smaller than the contribution from atmospheric neutrinos, which consequently dominate the total systematic uncertainty of the combined background.

A DOM's efficiency is the ratio of the light collected by a DOM to the total light incident upon that DOM. The DOM efficiency includes the quantum efficiency of the PMT and the transmissivity of the optical gel and glass of each sphere. A $\pm 10\%$ uncertainty in DOM efficiency is estimated for IceCube DOMs [96]. By changing the DOM efficiency in the simulation the effect on astrophysical (atmospheric) neutrinos event rates can be quantified to $\pm 4\%$ ($\pm 14\%$) for the low-energy sample, and $\pm 4\%$ ($\pm 17\%$) for the high-energy sample.

The simulation for this analysis assumes neutrino-nucleon cross sections based on CTEQ5 parton distributions [134]. The updated CSS [135] calculation using the ZEUS global PDF fit predicts smaller cross sections. By comparing simulated neutrino datasets with both models the systematic uncertainty from the neutrino cross-section model is quantified as $\pm 6\%$ ($\pm 3\%$) for astrophysical (atmospheric) neutrinos.

The uncertainty in the atmospheric neutrino flux prediction has two components: the theoretical uncertainty from the original calculations and the uncertainty in modifying the HKKMS07 model to include the atmospheric neutrino knee. The theoretical uncertainty of the conventional neutrino flux in the HKKMS07 model is about 25% [66]. Since the ERS model is used as a baseline for the prompt component its uncertainties are adopted [65]. Combined, these result in a systematic uncertainty of the atmospheric neutrino flux of $(-26\%, +25\%)$ and $(-37\%, +27\%)$ in the low- and high-energy samples, respectively. The knee in the cosmic-ray spectrum should lead to a similar feature in the atmospheric neutrino spectrum. The effect depends on the respective model for the cosmic-ray spectrum and the energy transfer from the primary to the neutrino. Due to the different energy ranges the samples are affected differently. The uncertainty was quantified to be $(-16\%, +0\%)$ and $(-23\%, +4\%)$ for the low- and high-energy samples, respectively.

Table 5.3 shows the resulting systematic uncertainty for the various samples, where the total uncertainties are obtained from adding each systematic uncertainty in quadrature.

	low-energy sample		high-energy sample	
	Atm. ν	$E^{-2}\nu$	Atm. ν	$E^{-2}\nu$
DOM efficiency	14%	4%	17%	4%
Ice model	24%	11%	24%	11%
ν cross sections	3%	6%	3%	6%
Theoretical	$-26\% + 25\%$	n/a	$-37\% + 27\%$	n/a
Neutrino knee	-16% +0%	n/a	-23% +4%	n/a
Total	$-41\% + 37\%$	13%	$-50\% + 40\%$	13%
	Atm. μ (simulated)		Atm. μ (extrapolated)	
Total	50%		$-50\% + 150\%$	

Table 5.3: Overview on systematic uncertainties on the event count for both samples.

5.6 Bayesian Treatment of Systematic Uncertainties

The experiment under consideration is a counting experiment in the presence of background. In order to incorporate systematic and statistical uncertainties into the interpretation of the result, a Bayesian approach was chosen [136]. The probability to have observed n_{obs} events in the presence of n_{sig} signal events, with signal selection efficiency ϵ and n_{bg} background events is given by the Poisson probability:

$$P(n_{\mathrm{obs}}|n_{\mathrm{sig}}, n_{\mathrm{bg}}) = \frac{(\epsilon n_{\mathrm{sig}} + n_{\mathrm{bg}})^{n_{\mathrm{obs}}}}{n_{\mathrm{obs}}!} \exp\left(-(\epsilon n_{\mathrm{sig}} + n_{\mathrm{bg}})\right). \tag{5.11}$$

From having observed n_{obs} one wants to infer, whether a given value of n_{sig} is supported or ruled out by the experimental result. This information is given by the posterior probability of n_{sig}, which can be obtained by applying Bayes theorem. In order to use the theorem, available information on the expected signal as well as the uncertainty of the other parameters must be quantified in the form of priors. By marginalizing over all parameters other than n_{sig}, remaining uncertainties are then incorporated into the final result.

The background uncertainties from model predictions and selection efficiencies are described by $p(n_{\mathrm{bg}})$. For the signal all uncertainties are modeled with $p(\epsilon)$ and the prior belief with $p(n_{\mathrm{sig}})$. The posterior probability can then be calculated:

$$P(n_{\mathrm{sig}}|n_{\mathrm{obs}}) \propto \int dn_{\mathrm{bg}} d\epsilon P(n_{\mathrm{obs}}|n_{\mathrm{sig}}, n_{\mathrm{bg}}) p(n_{\mathrm{bg}}) p(\epsilon) p(n_{\mathrm{sig}}) \tag{5.12}$$

A constant is chosen for the signal prior to reflect no prior knowledge on the signal. For the

background prior a Gaussian is used. The mean is centered at the rate prediction, the width represents the modeled uncertainty and it is truncated at zero since rates have to be positive. The uncertainty in the signal efficiency is modeled with the factor ϵ that is applied to the number of signal events after all cuts. The prior for ϵ is modeled with a Gaussian centered at 1 and having a width corresponding to the uncertainty. It is also truncated at zero.

The decision to model all signal-related uncertainties with ϵ and to calculate the posterior probability for n_{sig} was made here for practical reasons. Alternatively, when searching for an astrophysical neutrino flux with spectrum $dN/dE = \Phi_0 \cdot E^{-2}$, the posterior could also be calculated for the flux normalization constant Φ_0. Both choices are equivalent since n_{sig} and Φ_0 are directly proportional to each other. Presenting the final result in terms of n_{sig} has the advantage, that the posterior can be compared to astrophysical signal predictions which do not follow an unbroken power law.

6 Results and Discussion

Until this point 90% of the data have been kept blind. Now, after the event selection has been prepared and reviewed, this sample is finally unblinded. The events passing the cuts of the low- and high-energy samples are counted and their number is compared to the passing rates estimated from simulations. A hypothesis test is performed and the significance of deviations from the background-only estimates are calculated. In this chapter the findings in the individual samples are presented and discussed. A comparison between the observed and expected event counts is presented in Table 6.1.

6.1 Search for atmospheric neutrinos

The low-energy sample with an energy threshold of about 2 TeV aimed at the observation of atmospheric neutrinos, which for this sample will be called the signal. In total 67 events were observed over an expectation of 41.1 events from atmospheric muons, 27.8 from conventional neutrinos and 2.25 from prompt atmospheric neutrinos, respectively. Accordingly, the excess above atmospheric muons is quantitatively well-described by the atmospheric neutrino prediction by the HKKMS07 and ERS models. Also, the properties of the found events match the expectations from the simulation datasets. This is illustrated for the distribution of the BDT output variable in Figure 6.1 and the reconstructed energy spectrum in Figure 6.2. A representative selection of 6 event displays is shown in Figure 6.4.

The rather large uncertainty of the atmospheric muon background requires a careful evaluation of the significance of the atmospheric neutrino excess. By marginalizing over the uncertainty in the background and signal predictions, using the method described in Section 5.6, the posterior probability for the number of signal events is obtained (see Figure 6.3). The observed excess over the atmospheric muon prediction matches the number of expected atmospheric neutrinos very well. Hence, also the posterior peaks around 30 non-background events, or 100% of the predicted conventional and prompt neutrino flux (as illustrated by the upper axis of Figure 6.3). The 90% credible interval ranges from 5 to 62 non-background events, or 16% to 206% of the atmospheric neutrino flux. The steep drop of the posterior for much higher numbers of atmospheric neutrinos indicates that such a scenario would be in contradiction with this result. A similar drop of the

posterior is not observed for small numbers of signal events. Instead, the levelling of the posterior indicates that the low-energy sample is not sensitive enough to rule out the possibility of a very small atmospheric neutrino flux.

The significance of the excess over atmospheric muons including systematic errors is 1.1σ. Hence, no observation of atmospheric neutrinos is claimed. The average event energies of atmospheric neutrinos are 6 TeV and hence comparable to the highest energy bin of the analyses of contained events inside the DeepCore/IceCube 79-string configuration (see Ref. [68] and Figure 2.4).

Two events in the $100 - 180$ TeV bin of Figure 6.2 stand out. But in the cut-and-count approach used here their effect in the significance calculation is dwarfed by the large muon background and its uncertainty. However, these two events were also found in the high-energy sample.

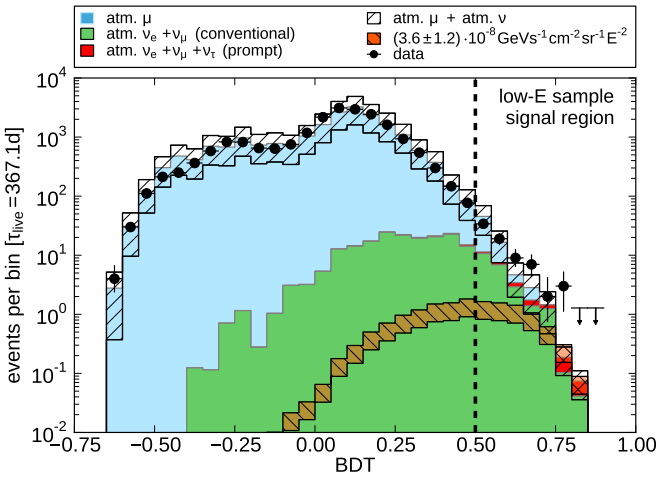

Figure 6.1: The BDT output variable. A cut at BDT > 0.5 defines the low-energy sample. The atmospheric muon and neutrino components are stacked on top of each other. The white hatched area shows the combined distribution of atmospheric muons and neutrinos, including systematic and statistical uncertainties. The shown experimental data comprises 100% of the sample and is well-described by the background prediction. For bins in which no event was observed a 68% C.L. upper limit is shown. The orange hatched area illustrates the prediction of astrophysical neutrinos according to the flux estimate from [1].

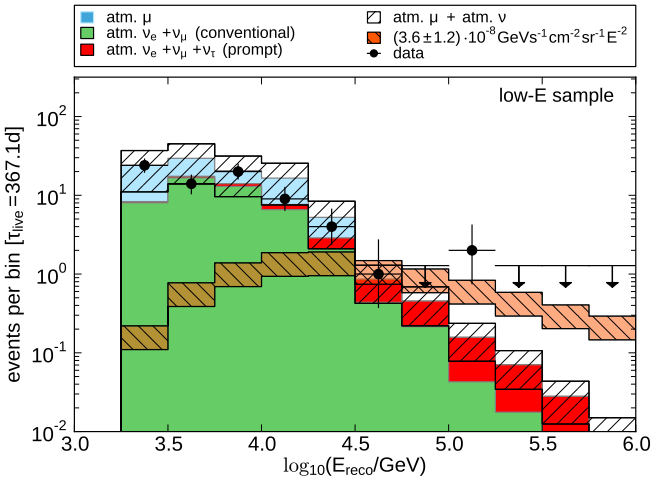

Figure 6.2: The reconstructed energy spectrum of the low-energy sample. The experimental data shown comprises 100% of the sample. The same stacking of background distributions is used as in Figure 6.1.

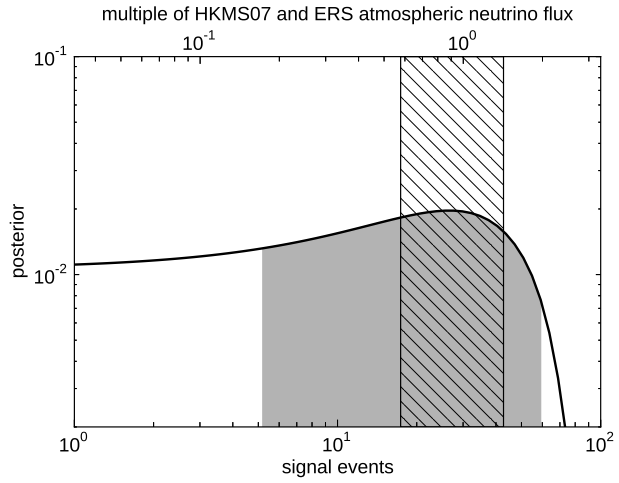

Figure 6.3: The posterior probability for the number of non-background events after the observation of 67 events in the low-energy sample. The upper axis transforms the number of signal events into multiples of the atmospheric neutrino flux. The grey shaded area indicates the 90% credible interval ranging from 16% to 206% of the atmospheric neutrino flux. The hatched area indicates the prediction of the HKKMS07 and ERS models including its uncertainty.

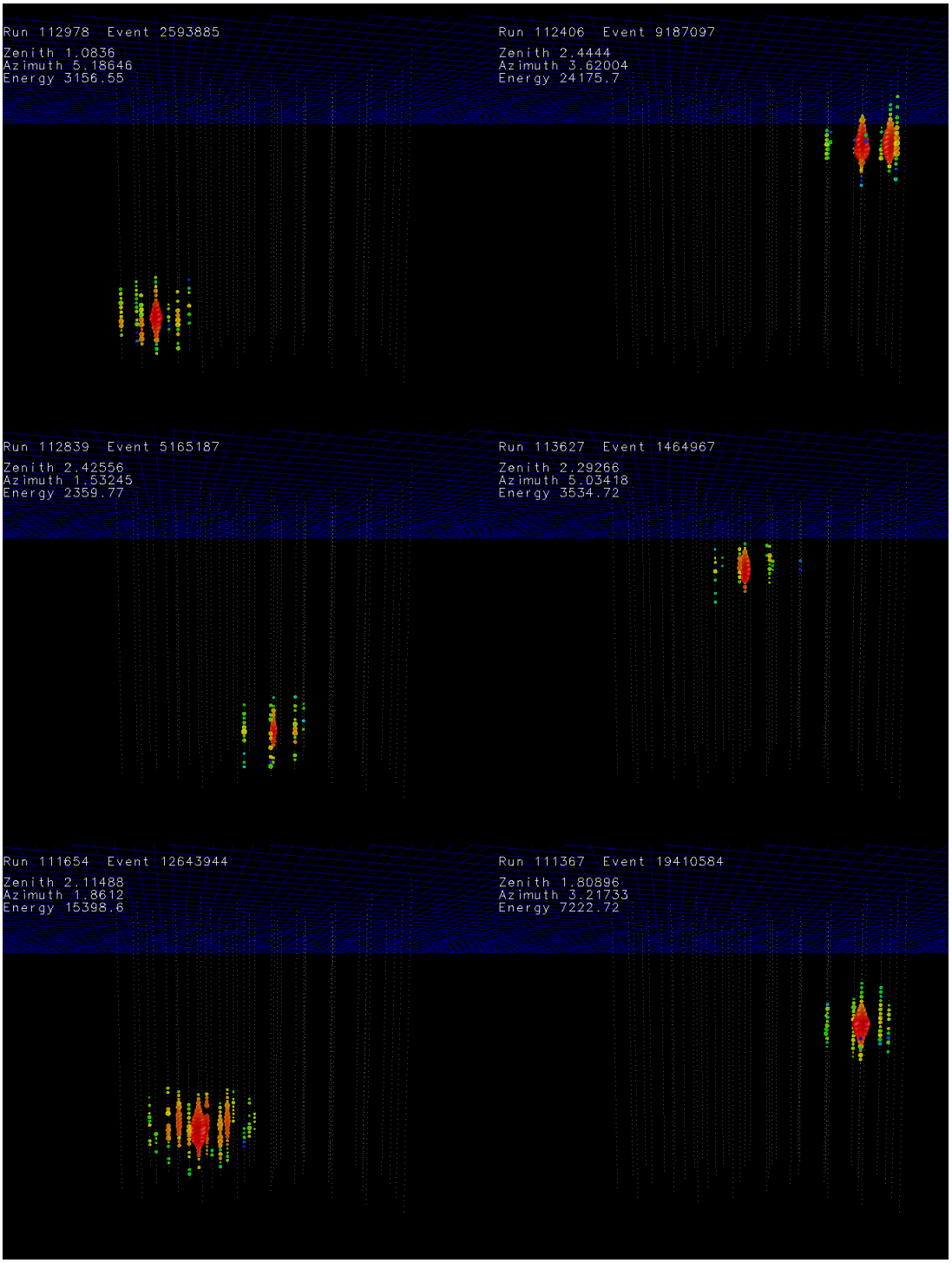

Figure 6.4: Event displays for 6 out of 67 events that pass the cuts of the low-energy sample are shown. As intended the events passing the event selection resemble cascade-like events.

Sample	low-energy	high-energy
E_{cut}	2 TeV	100 TeV
10% sample	7	1
90% sample	67	3
atm. μ	41.1 ± 9.5	0.04
Bartol (no knee) [74]	25.5 ± 2.8	0.078 ± 0.012
HKKMS07 (+knee) [16, 66, 75]	27.8 ± 3.0	0.054 ± 0.009
ERS [65] (max.)	2.76 ± 0.07	0.198 ± 0.005
ERS [65]	2.25 ± 0.06	0.155 ± 0.004
ERS [65] (min.)	1.29 ± 0.03	0.090 ± 0.002
Martin GBW [70]	1.14 ± 0.03	0.078 ± 0.002
$3.6 \times 10^{-8} E^{-2}$	4.54 ± 0.12	1.96 ± 0.05

Table 6.1: Event count predictions and results for the different samples and for models of conventional, prompt and astrophysical neutrinos. The model predictions are calculated for 90% of the experimental data. Where they are derived from simulation the statistical errors are given. The three lines of the ERS model show the uncertainty band.

6.2 Search for astrophysical neutrinos

The high-energy sample with an energy threshold of 100 TeV differs from the low-energy sample only in the lower BDT cut and higher energy cut. The cuts were optimized for highest sensitivity towards an E^{-2} spectrum and the tighter cuts lead to a purer neutrino sample. In total 3 events were found over an expectation of 0.04 from atmospheric muons and 0.21 from atmospheric conventional and prompt neutrinos. At these higher energies the expected contribution from prompt neutrinos exceeds the conventional neutrinos by a factor of 3. The events have energies of 144 ± 60 TeV, 144 ± 60 TeV and 224 ± 90 TeV. One additional event with 135 ± 50 TeV was also in the 10% sample which was used to develop the analysis. It is not considered in the significance calculation. Three of the events are reconstructed as horizontal events with zenith angles of $103° \pm 30°$, $70° \pm 30°$ and $69° \pm 30°$. The other event is reconstructed as an upgoing particle with a zenith angle of $146° \pm 30°$. Images illustrating the hit patterns of all four events are shown in Figure 6.5.

The 3 events found are a rather large excess, not only above the muonic background but also above the atmospheric neutrinos. It corresponds to 2.7σ above both classes of background. Again, no observation of the diffuse astrophysical neutrino flux is claimed. The method described in Section 5.6 is employed to account for all systematic and statistical errors on the background expectation and to calculate the posterior probability for the potential signal flux. The result is shown in Figure 6.7.

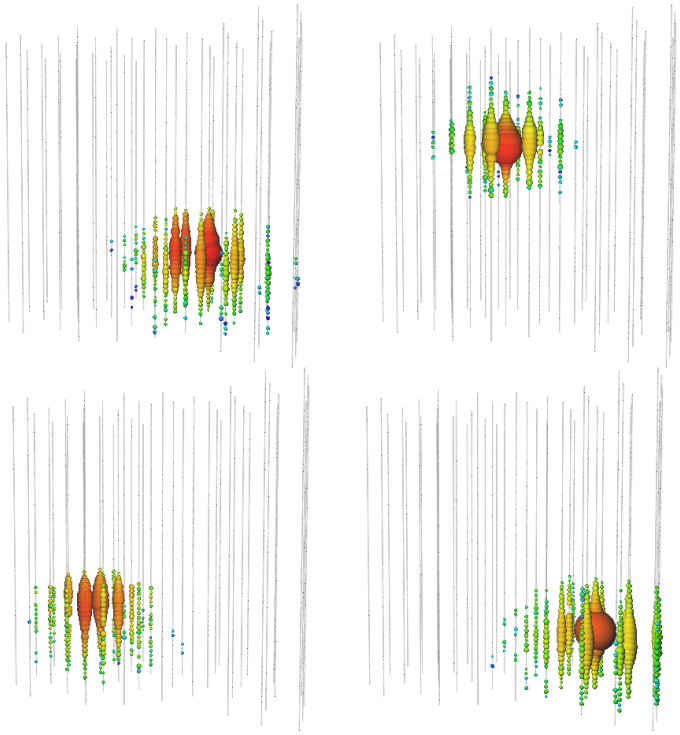

Figure 6.5: Three cascade-like events above 100 TeV were found in the high-energy sample. An additional event was already found in the 10% sample used to develop the cuts.

As a consequence of the observed excess the posterior peaks around a flux normalization for an unbroken all-flavor E^{-2} flux of $5 \times 10^{-8}\,\mathrm{GeVsr^{-1}s^{-1}cm^{-2}}$. The 90% credible interval covers the range $(2 - 14) \times 10^{-8}\,\mathrm{GeVsr^{-1}s^{-1}cm^{-2}}$. For the 1:1:1 flavor ratio at Earth, that is assumed throughout this analysis, 64% of the expected events would stem from electron neutrinos, 23% from tau neutrinos and 13% from muon neutrinos.

The flux estimate derived from the high-energy sample is compatible[1] with the astrophysical flux derived in [1], taking into account the systematic uncertainties. The flux is higher than the upper limit found in a search for high-energy muon neutrinos with the larger IceCube-59 [16]. This is not necessarily a contradiction, since the upper limit is set under the assumption of an unbroken power law - a practical premise until more measurements of high energetic neutrinos provide a handle on any cutoff in the spectrum. A non-equalized flavor ratio or a slightly different slope of the neutrino spectrum could explain this, too.

[1] The upper axis in Figure 6.7 transforms the number of signal events into a flux normalization for an unbroken E^{-2} power law. The measurement in [1] found indications for a cutoff at 2 PeV which is taken into account in Figure 6.7. Hence, the corresponding flux normalization constant shown here is lower than the published value of $\mathrm{E^2\Phi} = (3.6 \pm 1.2)\,\mathrm{GeVsr^{-1}s^{-1}cm^{-2}}$

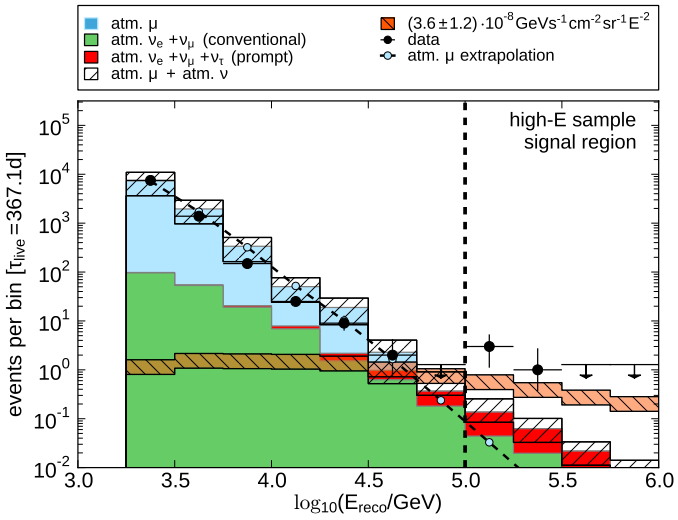

Figure 6.6: The reconstructed energy spectrum of the high-energy sample. The same stacking of background distributions is used as in Figure 6.1. The energy spectrum of simulated atmospheric muon events is extrapolated (dashed line) from lower energies up to the signal region above 100 TeV. The experimental data shown comprises 100% of the sample. For bins in which no event was observed a 68% C.L. upper limit is shown. The orange hatched area illustrates the prediction of astrophysical neutrinos according to the flux estimate from [1].

The results of the low- and high-energy samples are consistent, with an excess appearing only towards larger energies. Of the three events in the high-energy sample two are also in the low-energy sample.

The other two cascade searches performed on the IceCube-40 dataset resulted in upper limits on the diffuse neutrino flux. The lower of both limits [15, 128] is also shown in Figure 6.7. This analysis had an energy threshold of about 25 TeV and was optimized for highest sensitivity towards a diffuse E^{-2} spectrum. In total 14 events were observed including the three events found here. With a background expectation of 10.7 events the sample had a similar high background contamination as the low-energy sample. The obtained upper limit of $E^2\Phi = 7.46\,\mathrm{GeV sr^{-1} s^{-1} cm^{-2}}$ is only slightly higher than the flux estimate derived from the high-energy sample. It is because of the more robust background estimate achieved here that the high-energy sample was defined with tighter cuts and resulted in a more significant excess.

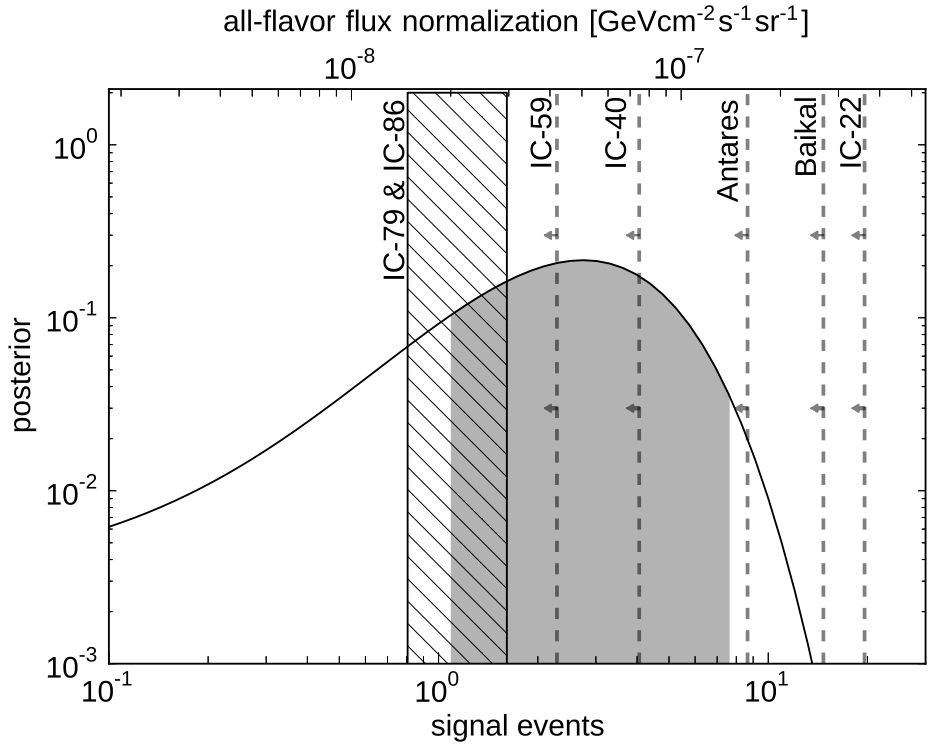

Figure 6.7: The posterior probability for the number of non-background events after the observation of 3 events in the high-energy sample. The upper axis transforms the number of signal events into the all-flavor flux normalization of an unbroken power law with index -2 (see also the footnote at page 100). The grey shaded area indicates the 90% credible interval ranging from $(2-14)\times10^{-8}\,\mathrm{GeVsr^{-1}s^{-1}cm^{-2}}$. The hatched area indicates the measurement of the astrophysical neutrino flux from [1]. The vertical lines indicate previous upper limits established by IceCube-59 [16], IceCube-40 [15, 128], Antares [77], Baikal [76] and IceCube-22 [11].

7 Summary & Outlook

This dissertation presented a search for neutrino-induced particle showers, also called cascades, conducted on a dataset recorded with the IceCube detector between April 2008 and May 2009. During this period 40 IceCube strings were deployed and operational instrumenting about half a cubic-kilometer of glacial ice at the geographic South Pole. The analysis aimed at detecting the astrophysical diffuse neutrino flux while maintaining sensitivity to atmospheric neutrinos. These neutrino fluxes had to be isolated from a much more abundant background of air-shower-induced muons. For these purposes problems identified in previous cascade searches had to be overcome and new techniques had to be developed.

Firstly, the improved cascade reconstruction algorithm `CREDO`, which had been developed prior to the start of this analysis [123], has been brought to application. In IceCube this algorithm was the first to provide an estimate on the neutrino direction in cascade-like events by achieving an angular resolution of 30°.

Secondly, previous cascade searches were impeded by the lack of sufficiently sized simulated atmospheric muon datasets. Their creation is computationally challenging and care must be taken that proton-induced air showers are not underrepresented. This problem has been addressed by resorting to a simplified cosmic-ray composition model. Although it comprises only two components, it nevertheless reflects the qualitative differences between light and heavy elements. This facilitated the creation of an atmospheric muon dataset corresponding in size to more than one year of detector livetime at energies per nucleon $E/A > 90\,\mathrm{TeV}$. During the development of the event selection this dataset provided a robust background estimate.

Two event selections were prepared on simulation data and 10% of the experimental data, keeping the remaining 90% blind to prevent experimenter's bias. A low-energy sample with an energy threshold of about 2 TeV aimed at the detection of atmospheric neutrinos and a high-energy sample with an energy threshold of about 100 TeV targeted the astrophysical neutrino flux. The event selections were implemented as a step-wise process. Early steps in the event selection focussed on reducing the muon background, allowing to perform computationally more elaborate reconstructions at later steps. Eventually, a set of event describing variables with good data-to-simulation agreement and discrimination power were combined in a machine learning algorithm to obtain a single event quality parameter. Different thresholds on this parameter

and the reconstructed energy defined the low- and high-energy samples.

In the preparation of the low-energy sample a class of irreducible background events has been identified. These were atmospheric muon events exhibiting prominent bremsstrahlung cascades and little to no hint of the muon track. The geometry of the IceCube-40 configuration was especially vulnerable to this class of background events. As these events could not be removed without also eliminating the atmospheric neutrino signal, a high background contamination had to be accepted for the low-energy sample. Additionally, sizable systematic uncertainties had to be taken into account. They originated mostly from the limited knowledge of the optical ice properties at the South Pole, the selection efficiency of the muon background and the theoretical neutrino flux predictions.

When the 90% dataset was unblinded, in the low-energy sample an excess of events over the expectation from atmospheric muons was observed. Taking systematic uncertainties into account the significance of the excess was 1.1σ. The result can quantitatively be explained well by atmospheric neutrinos. But due to the high background contamination and the uncertainties involved, the result is also well-compatible with a background-only hypothesis.

Better background suppression was possible for the high-energy event selection resulting in a much purer event sample. In this sample 3 events with energies $> 100\,\mathrm{TeV}$ were observed over an expectation of 0.25 events of atmospheric neutrinos (both conventional and prompt) as well as atmospheric muons — a $2.7\,\sigma$ excess. The 10% sample contained a fourth event which has not entered the significance calculation.

This excess is noteworthy. Although not significant enough to claim evidence for an astrophysical neutrino flux, it is consistent with similar excesses found in diffuse neutrino searches with IceCube-59 using muon neutrino events [16], the two PeV events found in [10] and the evidence for the astrophysical diffuse neutrinos established by the completed IceCube detector [1]. This analysis thereby provided three neutrino event candidates between 144 TeV and 224 TeV — an intermediate energy scale — with unprecedented low background contamination of conventional atmospheric neutrinos and muons. The constraints on the all-flavor normalization of the diffuse astrophysical neutrino flux with equal flavor contributions are summarized in Figure 6.7. A 90% credible interval covers the range $(2 - 14) \times 10^{-8}\,\mathrm{GeV sr^{-1} s^{-1} cm^{-2}}$ and is compatible with the more stringent flux estimates obtained in [1]. This sensitivity towards the diffuse flux of high-energy neutrinos was reached using data from only 50% of the final IceCube configuration. Together with the findings of other IceCube searches this result enters a global likelihood fit in which it contributes to further constrain the estimates on the diffuse astrophysical neutrino flux [137].

Additionally, the tools and techniques developed for this thesis helped paving the way for later cascade searches with IceCube. The approach to the background simulation problem presented

here has led to optimization studies performed elsewhere. After its extension to a cosmic-ray composition model with not only two, but five components, the approach enabled the creation of a similar-sized atmospheric muon dataset also for the follow-up search conducted with the IceCube-59 configuration [138]. Furthermore, background rejection techniques developed for this analysis proved to be useful in the cascades searches with the IceCube-79 configuration [139]. Finally, the `CREDO` program has been the basis for more advanced reconstruction algorithms which incorporate improvements in the understanding of the detector response and a better modeling of the ice [103]. The ability to reconstruct the cascade direction was of crucial importance in the search that finally established the evidence for the astrophysical neutrino flux [1].

With their good energy resolution and the little intrinsic background associated with the signature of high-energy neutrino-induced particle showers, cascade searches provide large sensitivity to the diffuse astrophysical neutrino flux. Consequently, they will continue to play a prime role in the exploration of the non-thermal universe with neutrinos — an endeavor that has just begun.

Bibliography

[1] M. Aartsen *et al.*, "Evidence for High-Energy Extraterrestrial Neutrinos at the IceCube Detector", *Science* **342** (2013) 1242856, arXiv:1311.5238.

[2] V. Hess, "Über die Bedeutung der durchdringenden Strahlung bei sieben Freiluftballonfahrten", *Phys.Zeitschr.* **12** (1912) 998.

[3] L. Anchordoqui and F. Halzen, "IceHEP high energy physics at the south pole", *Annals Phys.* **321** (2006) 2660–2716, arXiv:hep-ph/0510389.

[4] I. Belolaptikov *et al.*, "The Baikal underwater neutrino telescope: Design, performance and first results", *Astropart.Phys.* **7** (1997) 263–282.

[5] E. Aslanides *et al.*, "A deep sea telescope for high-energy neutrinos", arXiv:astro-ph/9907432.

[6] C. Spiering, "Towards High-Energy Neutrino Astronomy. A Historical Review", *Eur.Phys.J.* **H37** (2012) 515–565, arXiv:1207.4952.

[7] A. Achterberg *et al.*, "First year performance of the IceCube neutrino telescope", *Astroparticle Physics* **26** no. 3, (2006) 155 – 173.

[8] J. F. Beacom and J. Candia, "Shower power: Isolating the prompt atmospheric neutrino flux using electron neutrinos", *JCAP* **0411** (2004) 009, arXiv:hep-ph/0409046.

[9] M. Kowalski, "Measuring diffuse neutrino fluxes with IceCube", *JCAP* **0505** (2005) 010, arXiv:astro-ph/0505506.

[10] M. Aartsen *et al.*, "First observation of PeV-energy neutrinos with IceCube", *Phys.Rev.Lett.* **111** (2013) 021103, arXiv:1304.5356.

[11] R. Abbasi *et al.*, "First search for atmospheric and extraterrestrial neutrino-induced cascades with the IceCube detector", *Phys.Rev.* **D84** (2011) 072001, arXiv:1101.1692.

[12] M. P. Kowalski, "Search for Neutrino-Iduced Cascades with the AMANDA-II Detector". PhD thesis, Humboldt University to Berlin, 2003.

[13] R. Abbasi, Y. Abdou, T. Abu-Zayyad, O. Actis, J. Adams *et al.*, "Search for neutrino-induced cascades with five years of AMANDA data", *Astropart.Phys.* **34** (2011) 420–430.

[14] S. Panknin, "Search for Neutrino-Induced Cascades with the IceCube Neutrino Detector". PhD thesis, Humboldt Universität zu Berlin, 2011.

[15] S. Hickford, "A Cascade Analysis for the IceCube Neutrino Telescope". PhD thesis, University of Canterbury, 2012.

[16] A. Schukraft, "A view of prompt atmospheric neutrinos with IceCube", *Nucl.Phys.Proc.Suppl.* (2013) , arXiv:1302.0127.

[17] T. Sanuki *et al.*, "Precise Measurement of Cosmic-Ray Proton and Helium Spectra with the BESS Spectrometer", *The Astrophysical Journal* **545** no. 2, (2000) 1135.

[18] N. Grigorov *et al. Yad. Fiz.* **1058** (1970) . Plotted values extracted from astro-ph/0608553.

[19] M. Amenomori *et al.*, "The All-Particle Spectrum of Primary Cosmic Rays in the Wide Energy Range from 10^{14} to 10^{17} eV Observed with the Tibet-III Air-Shower Array", *The Astrophysical Journal* **678** no. 2, (2008) 1165.

[20] M. G. Aartsen *et al.*, "Measurement of the cosmic ray energy spectrum with IceTop-73", *Phys. Rev. D* **88** (2013) 042004.

[21] M. Takeda *et al.*, "Energy determination in the Akeno Giant Air Shower Array experiment", *Astroparticle Physics* **19** no. 4, (2003) 447 – 462.

[22] R. U. Abbasi *et al.*, "First Observation of the Greisen-Zatsepin-Kuzmin Suppression", *Phys. Rev. Lett.* **100** (2008) 101101.

[23] J. Abraham *et al.*, "Observation of the Suppression of the Flux of Cosmic Rays above 4×10^{19} eV", *Phys. Rev. Lett.* **101** (2008) 061101.

[24] M. Ackermann *et al.*, "Fermi LAT observations of cosmic-ray electrons from 7 GeV to 1 TeV", *Phys. Rev. D* **82** (2010) 092004.

[25] J. Beringer *et al.*, "Review of Particle Physics (RPP)", *Phys.Rev.* **D86** (2012) 010001.

[26] K.-H. Kampert and M. Unger, "Measurements of the Cosmic Ray Composition with Air Shower Experiments", *Astropart.Phys.* **35** (2012) 660–678, arXiv:1201.0018.

[27] K. Greisen, "End to the cosmic ray spectrum?", *Phys.Rev.Lett.* **16** (1966) 748–750.

[28] J. R. Hörandel, "A Review of experimental results at the knee", *J.Phys.Conf.Ser.* **47** (2006) 41–50, arXiv:astro-ph/0508014.

[29] A. Bell, K. Schure, B. Reville and G. Giacinti, "Cosmic ray acceleration and escape from supernova remnants", arXiv:1301.7264.

[30] T. Gaisser, T. Stanev and S. Tilav, "Cosmic Ray Energy Spectrum from Measurements of Air Showers", *Front.Phys.China.* **8** (2013) 748–758, arXiv:1303.3565.

[31] E. Fermi, "On the Origin of the Cosmic Radiation", *Phys.Rev.* **75** (1949) 1169–1174.

[32] L. Anchordoqui, V. Barger, I. Cholis, H. Goldberg, D. Hooper *et al.*, "Cosmic Neutrino Pevatrons: A Brand New Pathway to Astronomy, Astrophysics, and Particle Physics", *JHEAp* (2013) , arXiv:1312.6587.

[33] T. Gaisser, "Cosmic Rays and Particle Physics". Cambridge University Press, 1990.

[34] M. S. Longair, "High Energy Astrophysics", vol. 3. Cambridge University Press, 2011.

[35] M. A. Malkov and L. O. Drury, "Nonlinear theory of diffusive acceleration of particles by shock waves", *Reports on Progress in Physics* **64** no. 4, (2001) 429.

[36] J. K. Becker, "High-energy neutrinos in the context of multimessenger astrophysics", *Physics Reports* **458** no. 4–5, (2008) 173 – 246.

[37] A. M. Hillas, "The Origin of Ultra-High-Energy Cosmic Rays", *Annual Review of Astronomy and Astrophysics* **22** no. 1, (1984) 425–444.

[38] J. Learned and K. Mannheim, "High-energy neutrino astrophysics", *Ann.Rev.Nucl.Part.Sci.* **50** (2000) 679–749.

[39] F. Aharonian *et al.*, "High-energy particle acceleration in the shell of a supernova remnant", *Nature* **432** (2004) 75–77, arXiv:astro-ph/0411533.

[40] M. Ackermann *et al.*, "Detection of the Characteristic Pion-Decay Signature in Supernova Remnants", *Science Magazine 2013* (2013) 807, arXiv:1302.3307.

[41] P. Meszaros, "Gamma-Ray Bursts", *Rept.Prog.Phys.* **69** (2006) 2259–2322, arXiv:astro-ph/0605208.

[42] A. A. Abdo *et al.*, "Fermi Observations of High-Energy Gamma-Ray Emission from GRB 080916C", *Science* **323** (2009) 1688–1693.

[43] E. Waxman and J. N. Bahcall, "High-energy neutrinos from cosmological gamma-ray burst fireballs", *Phys.Rev.Lett.* **78** (1997) 2292–2295, arXiv:astro-ph/9701231.

[44] R. Abbasi *et al.*, "An absence of neutrinos associated with cosmic-ray acceleration in γ-ray bursts", *Nature* **484** (2012) 351–353, arXiv:1204.4219.

[45] C. M. Urry and P. Padovani, "Unified Schemes for Radio-Loud Active Galactic Nuclei", *Publications of the Astronomical Society of the Pacific* **107** (1995) 803, astro-ph/9506063.

[46] M. Tluczykont, E. Bernardini, K. Satalecka, R. Clavero, M. Shayduk and O. Kalekin, " Long-term lightcurves from combined unified very high energy γ-ray data", *Astronomy & Astrophysics* **524** (2010) A48, arXiv:1010.5659.

[47] J. Albert *et al.*, "Probing Quantum Gravity using Photons from a flare of the active galactic nucleus Markarian 501 Observed by the MAGIC telescope", *Phys.Lett.* **B668** (2008) 253–257, arXiv:0708.2889.

[48] F. Stecker, C. Done, M. Salamon and P. Sommers, "High-energy neutrinos from active galactic nuclei", *Phys.Rev.Lett.* **66** (1991) 2697–2700.

[49] F. W. Stecker, "A note on high energy neutrinos from AGN cores", *Phys.Rev.* **D72** (2005) 107301, arXiv:astro-ph/0510537.

[50] M. Aartsen *et al.*, "Search for Time-independent Neutrino Emission from Astrophysical Sources with 3 yr of IceCube Data", *Astrophys.J.* **779** (2013) 132, arXiv:1307.6669.

[51] E. Waxman and J. N. Bahcall, "High-energy neutrinos from astrophysical sources: An Upper bound", *Phys.Rev.* **D59** (1999) 023002, arXiv:hep-ph/9807282.

[52] E. Waxman, "High energy cosmic ray and neutrino astronomy", arXiv:1101.1155.

[53] M. Ahlers, L. Anchordoqui, M. Gonzalez-Garcia, F. Halzen and S. Sarkar, "GZK Neutrinos after the Fermi-LAT Diffuse Photon Flux Measurement", *Astropart.Phys.* **34** (2010) 106–115, arXiv:1005.2620.

[54] B. Cleveland, T. Daily, J. Davis, Raymond, J. R. Distel, K. Lande *et al.*, "Measurement of the solar electron neutrino flux with the Homestake chlorine detector", *Astrophys.J.* **496** (1998) 505–526.

[55] Y. Fukuda *et al.*, "Solar Neutrino Data Covering Solar Cycle 22", *Phys. Rev. Lett.* **77** (1996) 1683–1686.

[56] Q. R. Ahmad *et al.*, "Measurement of the Rate of $\nu_e + d \to p + p + e^-$ Solar Neutrinos at the Sudbury Neutrino Observatory", *Phys. Rev. Lett.* **87** (2001) 071301.

[57] Y. Ashie *et al.*, "Evidence for an Oscillatory Signature in Atmospheric Neutrino Oscillations", *Phys. Rev. Lett.* **93** (2004) 101801.

[58] J. K. Ahn *et al.*, "Observation of Reactor Electron Antineutrinos Disappearance in the RENO Experiment", *Phys. Rev. Lett.* **108** (2012) 191802.

[59] F. P. An *et al.*, "Observation of Electron-Antineutrino Disappearance at Daya Bay", *Phys. Rev. Lett.* **108** (2012) 171803.

[60] N. Agafonova *et al.*, "Evidence for $\nu_\mu \to \nu_\tau$ appearance in the CNGS neutrino beam with the OPERA experiment", `arXiv:1401.2079`.

[61] J. Learned and S. Pakvasa, "Detecting tau-neutrino oscillations at PeV energies", *Astropart.Phys.* **3** (1995) 267–274, `arXiv:hep-ph/9405296`.

[62] M. Gonzalez-Garcia, M. Maltoni, J. Salvado and T. Schwetz, "Global fit to three neutrino mixing: critical look at present precision", *JHEP* **1212** (2012) 123, `arXiv:1209.3023`.

[63] T. Kashti and E. Waxman, "Flavoring astrophysical neutrinos: Flavor ratios depend on energy", *Phys.Rev.Lett.* **95** (2005) 181101, `arXiv:astro-ph/0507599`.

[64] T. Gaisser and M. Honda, "Flux of atmospheric neutrinos", *Ann.Rev.Nucl.Part.Sci.* **52** (2002) 153–199, `arXiv:hep-ph/0203272`.

[65] R. Enberg, M. H. Reno and I. Sarcevic, "Prompt neutrino fluxes from atmospheric charm", *Phys.Rev.* **D78** (2008) 043005, `arXiv:0806.0418`.

[66] M. Honda, T. Kajita, K. Kasahara, S. Midorikawa and T. Sanuki, "Calculation of atmospheric neutrino flux using the interaction model calibrated with atmospheric muon data", *Phys.Rev.* **D75** (2007) 043006, `arXiv:astro-ph/0611418`.

[67] R. Abbasi *et al.*, "Measurement of the atmospheric neutrino energy spectrum from 100 GeV to 400 TeV with IceCube", *Phys.Rev.* **D83** (2011) 012001, `arXiv:1010.3980`.

[68] M. Aartsen *et al.*, "Measurement of the Atmospheric ν_e flux in IceCube", *Phys.Rev.Lett.* **110** (2013) 151105, `arXiv:1212.4760`.

[69] T. K. Gaisser, "Spectrum of cosmic-ray nucleons and the atmospheric muon charge ratio", arXiv:1111.6675.

[70] A. Martin, M. Ryskin and A. Stasto, "Prompt neutrinos from atmospheric $c\bar{c}$ and $b\bar{b}$ production and the gluon at very small x", *Acta Phys.Polon.* **B34** (2003) 3273–3304, arXiv:hep-ph/0302140.

[71] M. Aartsen *et al.*, "Observation of High-Energy Astrophysical Neutrinos in Three Years of IceCube Data", *Phys.Rev.Lett.* **113** (2014) 101101, arXiv:1405.5303.

[72] R. Abbasi *et al.*, "Determination of the Atmospheric Neutrino Flux and Searches for New Physics with AMANDA-II", *Phys.Rev.* **D79** (2009) 102005, arXiv:0902.0675.

[73] M. Gonzalez-Garcia, M. Maltoni and J. Rojo, "Determination of the atmospheric neutrino fluxes from atmospheric neutrino data", *JHEP* **0610** (2006) 075, arXiv:hep-ph/0607324.

[74] G. Barr, T. Gaisser, P. Lipari, S. Robbins and T. Stanev, "A Three - dimensional calculation of atmospheric neutrinos", *Phys.Rev.* **D70** (2004) 023006, arXiv:astro-ph/0403630.

[75] T. K. Gaisser, "Spectrum of cosmic-ray nucleons, kaon production, and the atmospheric muon charge ratio", *Astropart.Phys.* **35** (2012) 801–806.

[76] A. Avrorin, V. Aynutdinov, V. Balkanov, I. Belolaptikov, S. Berezhnev *et al.*, "The Baikal neutrino experiment", *Nucl.Instrum.Meth.* **A626-627** (2011) S13–S18.

[77] J. Aguilar *et al.*, "Search for a diffuse flux of high-energy ν_μ with the ANTARES neutrino telescope", *Phys.Lett.* **B696** (2011) 16–22, arXiv:1011.3772.

[78] I. Cholis and D. Hooper, "On The Origin of IceCube's PeV Neutrinos", *JCAP* **1306** (2013) 030, arXiv:1211.1974.

[79] J. Formaggio and G. Zeller, "From eV to EeV: Neutrino Cross Sections Across Energy Scales", *Rev.Mod.Phys.* **84** (2012) 1307, arXiv:1305.7513.

[80] A. Cooper-Sarkar, P. Mertsch and S. Sarkar, "The high energy neutrino cross-section in the Standard Model and its uncertainty", *JHEP* **1108** (2011) 042, arXiv:1106.3723.

[81] R. Gandhi, C. Quigg, M. H. Reno and I. Sarcevic, "Neutrino interactions at ultrahigh-energies", *Phys.Rev.* **D58** (1998) 093009, arXiv:hep-ph/9807264.

[82] H. Lai *et al.*, "Global QCD analysis of parton structure of the nucleon: CTEQ5 parton distributions", *Eur.Phys.J.* **C12** (2000) 375–392, arXiv:hep-ph/9903282.

[83] S. L. Glashow, "Resonant Scattering of Antineutrinos", *Phys. Rev.* **118** (1960) 316–317.

[84] A. Dziewonski and D. Anderson, "Preliminary reference earth model", *Phys.Earth Planet.Interiors* **25** (1981) 297–356.

[85] P. Cerenkov, "Visible radiation produced by electrons moving in a medium with velocities exceeding that of light", *Phys.Rev.* **52** (1937) 378–379.

[86] J. V. Jelley, "Čerenkov Radiation and its applications". United Kingdom Atomic Energy Authority, 1958.

[87] D. H. Perkins, "Introduction to High Energy Physics". Cambridge University Press, 2000.

[88] C. H. Wiebusch, "The Detection of Faint Light in Deep Underwater Neutrino Telescopes". PhD thesis, RWTH Aachen, 1995.

[89] L. Gerhardt and S. R. Klein, "Electron and Photon Interactions in the Regime of Strong LPM Suppression", *Phys.Rev.* **D82** (2010) 074017, arXiv:1007.0039.

[90] L. Rädel and C. Wiebusch, "Calculation of the Cherenkov light yield from electromagnetic cascades in ice with Geant4", *Astropart.Phys.* **44** (2013) 102–113, arXiv:1210.5140.

[91] M. Kowalski, "On the cherenkov light emission of hadronic and electro-magnetic cascades." Amanda internal report amanda-ir/20020803, 2002.

[92] D. Chirkin and W. Rhode, "Muon Monte Carlo: A new high precision tool for muon propagation through matter",.

[93] M. Markov and I. Zheleznykh, "On high energy neutrino physics in cosmic rays", *Nuclear Physics* **27** no. 3, (1961) 385 – 394.

[94] R. Abbasi *et al.*, "The IceCube Data Acquisition System: Signal Capture, Digitization, and Timestamping", *Nucl.Instrum.Meth.* **A601** (2009) 294–316, arXiv:0810.4930.

[95] E. Andres, P. Askebjer, S. Barwick, R. Bay, L. Bergstrom *et al.*, "The AMANDA neutrino telescope: Principle of operation and first results", *Astropart.Phys.* **13** (2000) 1–20, arXiv:astro-ph/9906203.

[96] R. Abbasi *et al.*, "Calibration and Characterization of the IceCube Photomultiplier Tube", *Nucl.Instrum.Meth.* **A618** (2010) 139–152, arXiv:1002.2442.

[97] P. B. Price and L. Bergström, "Optical properties of deep ice at the South Pole: scattering", *Applied Optics* **36** no. 18, (1997) 4181–4194.

[98] M. Ackermann *et al.*, "Optical properties of deep glacial ice at the South Pole", *Geophys.Res.* **111(D13203)** (2006) 282–300.

[99] P. Askebjer, S. W. Barwick, L. Bergstrom, A. Bouchta, S. Carius *et al.*, "Optical properties of deep ice at the South Pole: Absorption", *Appl.Opt.* **36** (1997) 4168–4180, arXiv:physics/9701025.

[100] S. L. Miller, "Clathrate Hydrates of Air in Antarctic Ice", *Science* **165** no. 3892, (1969) 489–490.

[101] M. Aartsen *et al.*, "Measurement of South Pole ice transparency with the IceCube LED calibration system", *Nucl.Instrum.Meth.* **A711** (2013) 73–89, arXiv:1301.5361.

[102] M. Aartsen *et al.*, "Observation of the cosmic-ray shadow of the Moon with IceCube", *Phys.Rev.* **D89** (2014) 102004, arXiv:1305.6811.

[103] M. Aartsen *et al.*, "Energy Reconstruction Methods in the IceCube Neutrino Telescope", *JINST* **9** (2014) P03009, arXiv:1311.4767.

[104] D. Pandel, "Bestimmung von Wasser- und Detektorparametern und Rekonstruktion von Myonen bis 100 TeV mit dem Baikal-Neutrinoteleskop NT-72." Diploma thesis, Humboldt Universität zu Berlin, 1996.

[105] J. Lundberg, P. Miocinovic, T. Burgess, J. Adams, S. Hundertmark *et al.*, "Light tracking for glaciers and oceans: Scattering and absorption in heterogeneous media with Photonics", *Nucl.Instrum.Meth.* **A581** (2007) 619–631, arXiv:astro-ph/0702108.

[106] N. Whitehorn, J. van Santen and S. Lafebre, "Penalized splines for smooth representation of high-dimensional Monte Carlo datasets", *Computer Physics Communications* **184** no. 9, (2013) 2214 – 2220, 1301.2184.

[107] W. H. Press, S. A. Teukolsky, W. T. Vetterling and B. P. Flannery, "Numerical Recipes in C++: The Art of Scientific Computing". Cambridge University Press, 2002.

[108] C. Finley, "Weighting NeutrinoGenerator Events with OneWeight in IceSim 2.0", tech. rep., IceCube Collaboration, 2007.

[109] J. Kelley, "Reweighting and Livetime Normalization of dCORSIKA Monte Carlo", tech. rep., IceCube Collaboration, 2007.

[110] G. Bohm and G. Zech, "Einführung in Statistik und Messwertanalyse für Physiker". Verlag Deutsches Elektronen-Synchrotron, 2006.

[111] A. Gazizov and M. P. Kowalski, "ANIS: High energy neutrino generator for neutrino telescopes", *Comput.Phys.Commun.* **172** (2005) 203–213, arXiv:astro-ph/0406439.

[112] B. Voigt, "Sensitivity of the IceCube Detector for Ultra-High Energy Electron-Neutrino Events". PhD thesis, Humboldt Universität zu Berlin, 2008.

[113] D. Chirkin, "Fluxes of atmospheric leptons at 600 GeV - 60 TeV", arXiv:hep-ph/0407078.

[114] D. Chirkin, "Cosmic ray energy spectrum measurement with the Antarctic Muon and Neutrino Detector Array (AMANDA)". PhD thesis, University of California, Berkeley, 2003.

[115] D. Heck, G. Schatz, T. Thouw, J. Knapp and J. Capdevielle, "CORSIKA: A Monte Carlo code to simulate extensive air showers",.

[116] Engel *et al.* in *Proc. 26th ICRC*, vol. 1, p. 415. 1999.

[117] M. D'Agostino, "First Evidence For Atmospheric Neutrino-Induced Cascades with the IceCube Detector". PhD thesis, University of California, Berkeley, 2009. arXiv:0910.2555.

[118] J. R. Hörandel, "On the knee in the energy spectrum of cosmic rays", *Astropart.Phys.* **19** (2003) 193–220, arXiv:astro-ph/0210453.

[119] R. Glasstetter *et al.*, "Analysis of electron and muon size spectra of EAS", in *Proc. 26 ICRC*, HE.2.2.03 1, 222. 1999.

[120] M. Aartsen, R. Abbasi, M. Ackermann, J. Adams, J. Aguilar *et al.*, "The IceProd Framework: Distributed Data Processing for the IceCube Neutrino Observatory", arXiv:1311.5904.

[121] E. Veach and L. J. Guibas, "Optimally combining sampling techniques for Monte Carlo rendering", in *Proceedings of the 22nd annual conference on Computer graphics and interactive techniques*, pp. 419–428, ACM. 1995.

[122] J. Klein and A. Roodman, "Blind analysis in nuclear and particle physics", *Ann.Rev.Nucl.Part.Sci.* **55** (2005) 141–163.

[123] E. Middell, "Reconstruction of Cascade-Like Events in IceCube." Diploma thesis, Humboldt Universität zu Berlin, 2008.

[124] F. James and M. Roos, "Minuit: A System for Function Minimization and Analysis of the Parameter Errors and Correlations", *Comput.Phys.Commun.* **10** (1975) 343–367.

[125] The IceCube Collaboration, "Event reconstruction in IceCube based on direct event re-simulation", in *Proceedings of the 33rd International Cosmic Ray Conference*. 2013. arXiv:1309.7010.

[126] J. Ahrens *et al.*, "Muon track reconstruction and data selection techniques in AMANDA", *Nucl.Instrum.Meth.* **A524** (2004) 169–194, arXiv:astro-ph/0407044.

[127] S. Panknin, "Request for the Cascade Online Filter", tech. rep., IceCube Collaboration, 2008.

[128] M. G. Aartsen *et al.*, "Search for neutrino-induced particle showers with IceCube-40", *Phys. Rev. D* **89** (2014) 102001.

[129] A. Hocker, P. Speckmayer, J. Stelzer, F. Tegenfeldt and H. Voss, "TMVA, toolkit for multivariate data analysis with ROOT",.

[130] R. O. Duda, P. E. Hart and D. Stork, "Pattern Classification". Wiley-Interscience, 2000.

[131] G. Punzi, "Sensitivity of searches for new signals and its optimization", arXiv:physics/0308063.

[132] G. Hill, J. Hodges, B. Hughey, A. Karle and M. Stamatikos, "Examining the balance between optimising an analysis for best limit setting and best discovery potential", PHYSTAT05, pp. 108–111. 2005.

[133] R. Abbasi *et al.*, "Study of South Pole ice transparency with IceCube flashers", arXiv:1111.2731. Papers submitted by the IceCube Collaboration to the 32nd International Cosmic Ray Conference, Beijing 2011/ part VI.

[134] R. Gandhi, C. Quigg, M. H. Reno and I. Sarcevic, "Ultrahigh-energy neutrino interactions", *Astropart.Phys.* **5** (1996) 81–110, arXiv:hep-ph/9512364.

[135] A. Cooper-Sarkar and S. Sarkar, "Predictions for high energy neutrino cross-sections from the ZEUS global PDF fits", *JHEP* **0801** (2008) 075, arXiv:0710.5303.

[136] G. D'Agostini, "Bayesian Reasoning in Data Analysis: A Critical Introduction". World Scientific Publishing Company, 2003.

[137] L. Mohrmann, "Measurement of the diffuse neutrino flux by a global fit to multiple IceCube results", in *13th International Conference on Topics in Astroparticle and Underground Physics, TAUP2013*. 2013.

[138] The IceCube Collaboration, "Search for diffuse astrophysical neutrinos with cascade events in the IceCube-59 detector", in *Proceedings of the 33rd International Cosmic Ray Conference*. 2013. `arXiv:1309.7003`.

[139] The IceCube Collaboration, "Search for extraterrestrial neutrino-induced cascades using IceCube 79-strings", in *Proceedings of the 33rd International Cosmic Ray Conference*. 2013. `arXiv:1309.7003`.

Acknowledgments

Looking back at the past years I would like to express my gratitude to many people who have helped me. First I would like to thank my supervisor Prof. Dr. Marek Kowalski. While giving me the freedom to explore my own solutions, he has always been available when I needed support. To the current and former members of the DESY Zeuthen cascade group: Dr. Markus Ackermann, Arne Schönwald, Achim Stößl, Lars Mohrmann and as well as Dr. Sebastian Panknin, Dr. Mike Walter, Dr. Rolf Nahnhauer, Dr. Jens Berdermann, Dr. Bernhardt Voigt and Dr. Lotfi Benabderrahmane: thank you for your assistance, the many fruitful discussions, also those about physics, and the pleasant working atmosphere that you have created. Thanks to Jakob van Santen and Dr. Nathan Whitehorn: I have learnt much from you. To Dr. Ralf Wischnewski: thank you for giving me from early on the chance to dive deep into the field of neutrino detection, while working with you at Lake Baikal. Similarly, I would like to thank Dr. Christian Spiering for making my visits to Lake Baikal and to the South Pole possible. Thanks to the members of the IceCube and Baikal collaboration: you are too many to name here, but I enjoyed working with you very much. Particular thanks to Prof. Joanna Kiryluk, Dr. Henrike Wissing, Dr. Aya Ishihara, Dr. Lisa Gerhardt, Dr. Stephanie Hickford, Prof. Jenni Adams, Prof. Todor Stanev, Prof. Ignacio Taboada, Dr. Mariola Lesiak-Bzdak and Dr. Claudio Kopper for their help in reviewing and publishing the analysis.

I owe much to my family and my friends: thank you for your support and forbearance.

To my wife Nadin: I wouldn't have made it without you.

Erklärung

Hiermit versichere ich, dass ich die vorliegende Arbeit selbständig verfasst und keine anderen als die angegebenen Quellen und Hilfsmittel verwendet habe. Ich habe mich nicht bereits anderwärts um einen Doktorgrad beworben und besitze keinen entsprechenden Doktorgrad. Ich erkläre die Kenntnisnahme der dem Verfahren zugrunde liegenden Promotionsordnung an der Mathematisch-Naturwissenschaftlichen Fakultät der Humboldt-Universität zu Berlin.

Ort und Datum

Eike Middell